The Promise of Nitrogen Plasma Implanted Gallium Arsenide for Band Gap Engineering

A Thesis Submitted to the
College of Graduate Studies and Research
in Partial Fulfillment of the Requirements
for the degree of Master of Science
in the Department of Department of Physics and
Engineering Physics
University of Saskatchewan
Saskatoon

By
Marcel Risch

Permission to Use

In presenting this thesis in partial fulfilment of the requirements for a Postgraduate degree from the University of Saskatchewan, I agree that the Libraries of this University may make it freely available for inspection. I further agree that permission for copying of this thesis in any manner, in whole or in part, for scholarly purposes may be granted by the professor or professors who supervised my thesis work or, in their absence, by the Head of the Department or the Dean of the College in which my thesis work was done. It is understood that any copying or publication or use of this thesis or parts thereof for financial gain shall not be allowed without my written permission. It is also understood that due recognition shall be given to me and to the University of Saskatchewan in any scholarly use which may be made of any material in my thesis.

Requests for permission to copy or to make other use of material in this thesis in whole or part should be addressed to:

Head of the Department of Physics and Engineering Physics
116 Science Place
University of Saskatchewan
Saskatoon, Saskatchewan
Canada
S7N 5E2

Abstract

This investigation examines band gap engineering of the GaAsN alloy by means of plasma ion implantation. The strong redshift of the alloy's band gap is suitable for telecommunication applications and thus stimulated much interest in recent years. Nitrogen (N) ion implantation into gallium arsenide (GaAs) results in a thin shallow N-rich layer below the surface. However, the violent implantation process also modifies the concentrations of gallium and arsenide. The core of this thesis is a novel method for prediction of the band gap from the conditions in the processing plasma.

The first important variable, the number of implanted ions, is obtained from the Lieberman model for the current during high-voltage Plasma Ion Implantation (PII). A review of the model's assumptions is provided as well as a comprehensive discussion of the implantation which includes error boundaries. The predicted and measured ion currents agree within error boundaries. The number of implanted ions can therefore be obtained from the prediction.

The distribution of the implanted ions was subsequently explored by simulations such as TRIM and TRIDYN. It was found that the nitrogen content in GaAs is limited by the sputtering of the surface atoms. Furthermore, the content of gallium increases near the surface while the content of arsenic decreases. The predicted ratios of the constituents in the implanted layer is such that the alloy cannot form by ion implantation alone; it could be reconciled by annealing.

Preliminary samples were produced and tested for the formation of the GaAsN alloy by Raman spectroscopy. No evidence for bonds between N and either Ga or As was found in the as-implanted samples. The thesis concludes with a discussion of the necessary steps to synthesize the GaAsN alloy.

Acknowledgements

I would like to express my sincere gratitude to my supervisor Dr. Michael Bradley for his outstanding support and of my work and for the other various extraordinary opportunities he offered for my development. I cannot think of a better inauguration into the world of researching physicists. I am also deeply indebted to JT Steenkamp for his ground-breaking work on the pulser system and continuing support thereof. Furthermore, I would like to extend my gratitude to Dr. Akira Hirose for providing the plasma facilities and resources and to David McColl for his exceptional technical support.

I am thankful to Dr. Ramaswami Sammynaiken, Jason Maley and Dr. Yuanshi Li for their fruitful discussions about the various aspects of Raman spectroscopy and its instrumentation. Furthermore, I appreciate the fruitful discussions about semiconductors with Dr. Safa Kasap and Dr. Robert Johanson. In addition, I am grateful to Dr. Andrew Robinson for offering his Communication Skills course which improved the overall presentation of this thesis. I greatly valued the positive working environment at the Plasma Physics Lab and especially the companionship of my fellow co-workers Darren Hunter, Kurt Krueger and Phillip Desautels which I would like to give special credit for the proof-reading this thesis. I would also like to thank my friends all over the world and my family for their encouragement and immense support.

I received financial support by the Department of Physics in my first year and I was awarded the Herzberg Fellowship at the U of S in my second year. I am more than thankful for all of the financial support.

This work is being supported by NSERC under the Discovery Grant # 403084.

Aber rühmen wir nicht nur den Weisen,
Dessen Name auf dem Büchlein prangt!
Denn man muß dem Weisen seine Weisheit erst entreißen.

but the honor should not be restricted
to the sage whose name is clearly writ.
for a wise man's wisdom needs to be extracted.

Berthold Brecht (1938)
Excerpt from the poem "Legende von der Entstehung des Buches
Tao Te King auf dem Weg des Laotse in die Emigration" [1]

Contents

List of Tables

List of Figures

List of Abbreviations

As	Arsenic
CMOS	Complementary Metal Oxide Semiconductor
Ga	Gallium
GaAs	Gallium Arsenide
GaAsN	The alloy consisting of gallium, arsenic and nitrogen
GaN	Gallium Nitride
LO	Longitudinal Optic Mode
MM	Marx Mode
N	Nitrogen
PBIID	Plasma Based Ion Implantation and Deposition
PII	Plasma Ion Implantation
PPL	Plasma Physics Laboratory
Si	Silicon
SRIM	Stopping and Range of Ions in Matter
TM	Transformer Mode
TO	Transverse Optic Mode
TRIDYN	Transport and Range of Ions for DYNamical Composition Changes
TRIM	Transport and Range of Ions in Matter
U of S	University of Saskatchewan

Chapter 1

Motivation

1.1 The Big Picture

Silicon (Si) is the current workhorse material of microelectronics and this is unlikely to change. Si is very abundant on earth and, due to its material properties, is the key component of today's transistors. Gate, insulator, source and drain are manufactured from polycrystalline silicon, silicon dioxide and doped crystalline silicon, respectively. Consequently, semiconductor processing facilities are highly specialized for silicon-based fabrication. Most of these facilities are incompatible with other materials.

The big players in the microprocessor industry are currently seeking to surpass silicon's limitations in order to keep up with the pace of progress of recent decades. Two key challenges are to shrink the size of transistors (i.e. obey Moore's law [2]) and the switch to optical circuits for increased inter-chip communication. As of 2008, it seems that the solution to both problems is to keep the Si foundation and add Si-compatible materials to overcome silicon's limitations. For example, Intel presented novel high-k metal gate transistors as well as an indium phosphide (InP) laser both on silicon chips in 2007. Other research intensive chip manufacturers are pursuing similar projects.

My research is also along these lines. In lieu of trying to increase the performance of silicon, a novel material is designed to fit onto Si at the atomic level. The gallium arsenide nitride (GaAsN) alloy is a promising candidate for the next generation of photonic emitters at the 1.3 μm wavelength which is used in telecommunication applications. This wavelength is chosen due to the local dispersion limit in the most widely used single mode glass fiber (i.e. SiO_2).

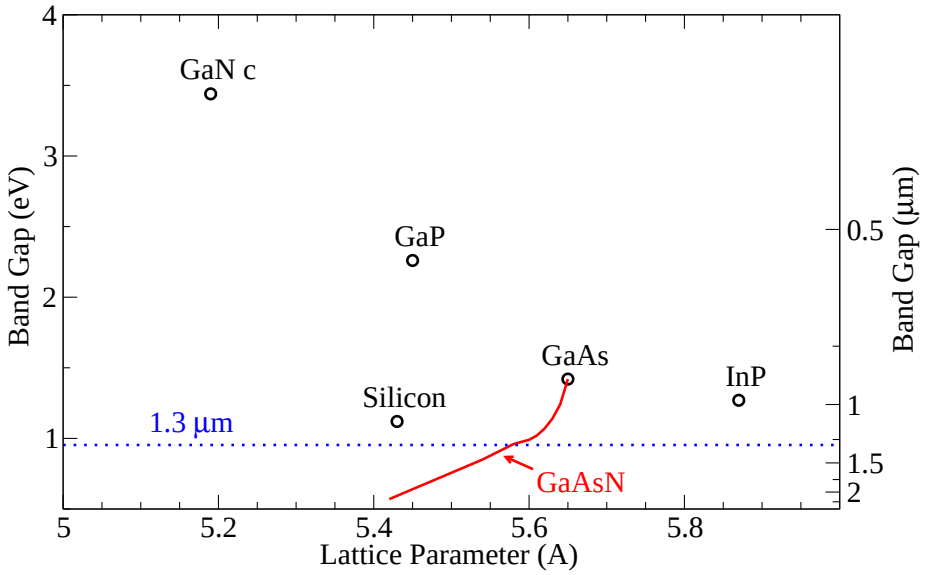

Figure 1.1. Band gaps of selected semiconductors as a function of their lattice constant. The data was compiled from [3, 4, 5, 6, 7]. The GaAsN band gap was calculated from the concentration-dependent bowing model discussed in Section 6.4 and the lattice parameter was calculated using Vengard's rule. 'GaN c' is the c lattice parameter of Wurtzite GaN.

Optical circuits have the advantage relative to electronic circuits of an increased band width and the elimination of cross-talk. The lattice parameter of GaAsN can be adjusted to match the one of Si to about 2.8% difference for light emission at 1.3 μm, see Fig. 1.1. This figure also reveals that the lattice parameter of the GaAsN alloy is closer to Si than to InP, which Intel used for their recent on-chip laser. Moreover, the melting point is about the same as that of Si, which makes GaAsN compatible with annealing procedures. The GaAsN alloy is therefore a candidate for an on-chip laser compatible with Si-processing technology. The GaAsN alloy could be manufactured cost-effectively by plasma ion implantation and then wafer bonded to Si via a wafer-cleave/layer transfer process. The result could be an on-chip CMOS-compatible laser for telecommunication applications or data transfer between neighbouring chips.

1.2 Objectives

The goal of my project is three-fold:

- Exploit the suitability of nitrogen plasma ion implantation into gallium arsenide (GaAs) for the synthesis and band gap engineering for the GaAsN alloy
- Correlate the conditions in the processing plasma with properties of the synthesized alloy
- Research techniques for the characterization of the ion-implanted thin films on the substrate's surface

I decided to attempt modelling as many of the processes involved in the fabrication as possible. Specifically, I extended existing software to estimate the expected dose as a function of the conditions in the processing plasma. This serves as the input to a simulation of the nitrogen ions' trace in the GaAs target. As a last step, I used reported models for the band gap of the alloy to convert spatial variation of the atomic concentration of N in GaAs into the band gap of the resulting GaAsN alloy.

The approach of an apriori design of a sample's features is not well developed in the plasma ion implantation community due to the complex nature of the process, which spans several fields of physics. Problems are usually tackled by order-of-magnitude estimations and a matrix of measurements. The apriori approach seemed the best option given the limited in-house resources. I cannot yet say whether my endeavor paid off scientifically due to missing experimental verification, but I learned so much that I may accept the journey as the reward. The following scheme guided me well to new insights:

1. Characterization of the nitrogen plasma
2. First design of the material by computational predictions
3. Production of samples

4. Characterization of the processed material (GaAsN)

5. Comparison with the predicted properties

6. Refinement of the models

This document is the result of several iterations through the scheme. It does not assert the claim of a final answer to all the problems uncovered in the process. The document should instead be seen as a progress report.

Chapter 2

Plasma Ion Implantation

Plasma Ion Implantation is defined and discussed in this chapter. The definition of a plasma may be found in my B.Sc. Thesis [8] or in Chen [9].

2.1 Introduction

Plasma Ion Implantation (PII) is a method to modify the surface as well as subsurface properties of materials. Tribological applications improve mechanical properties of the surface, such as wear resistance, and semiconductor applications improve the electronic properties, such as conductivity, by implanting a dopant. The method is closely related to ion beam implantation, which has been reduced in PII applications to the essential components, analogous to a simple dipole antenna made from a piece of wire replacing a resonant circuit. PII works without the intermediate stages of beam extraction, focusing, scanning, and substrate or wafer manipulation needed to implant complex targets with the beam implantation technique. The target is simply immersed in a plasma which serves as the ion source. When the target is biased by high-voltage pulses, the electric fields are such that all available ions are implanted into the sample in the small sheath limit. The ions are forced toward the target from all directions simultaneously, yielding a homogeneous distribution of the dose if the sheath is smaller than the features on the sample. Fig. 2.1 shows a schematic of implanting ions overlaid on a photograph of the plasma chamber used in my project.

The technique of Plasma Ion Implantation (PII or PI^2) is also known by a multiplicity of other names and their acronyms: Plasma Immersion Ion Implantation (PIII or PI^3), Plasma Immersion Ion Processing (PIIP), Plasma Source Ion Implan-

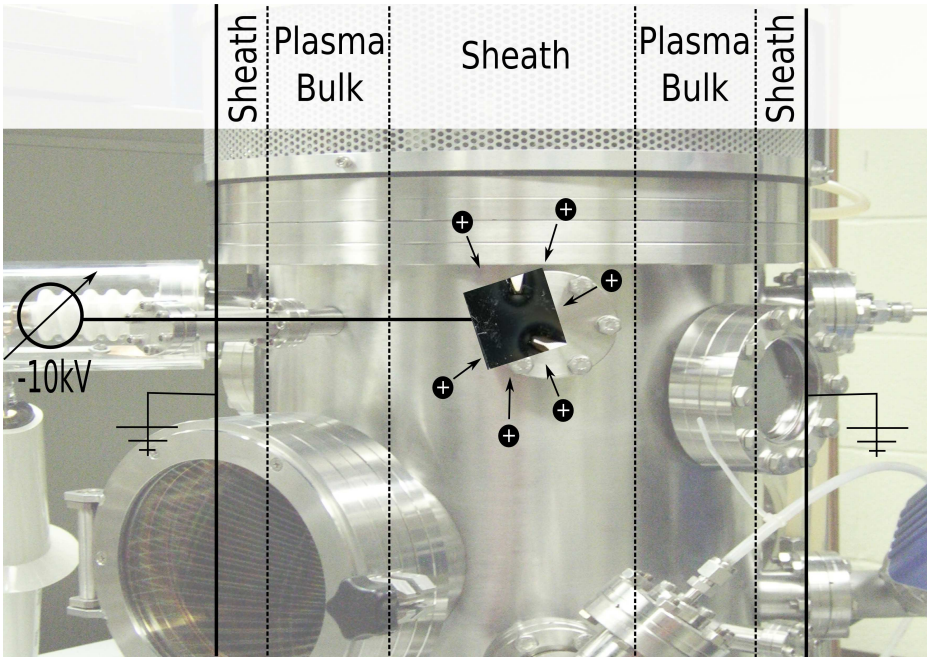

Figure 2.1. Profile of the regions inside the plasma chamber (not to scale). Plasma ions in the sheath surrounding the target are implanted by virtue of high-voltage pulses. We are grateful to Prof. A. Hirose for the permission to use his chamber in this study.

tation (PSI), Plasma Implantation (PI) or Plasma Ion Plating (PIP), to name a few. If the implantation process is followed by deposition, the suffix D is often added as in Plasma Based Ion Implantation and Deposition (PBIID). This is also the name of the yearly conference series of the PII community. The proceedings of all nine workshops provide an invaluable introduction to and overview of the field.

Key Properties

The advantages and limitations of PII are compiled in Table 2.1. Complex, large and heavy samples may be implanted due to the immersion in plasma and the concomitant omission of controlling an ion beam. The immersion in the ion sourcing plasma also renders the processing time independent of the plasma exposed surface area. In addition, the direct exposure of the surface to the plasma between pulses neutralizes surface charging. The dose will be applied uniformly to the sample if the electric field is perpendicular to the sample which is only the case for small sheath widths or flat samples. The major down side of the immersion is that all ions in the

Table 2.1. Advantages and limitations of plasma ion implantation.

Advantages	Limitations
Large and complicated samples possible	Dose uniformity limited by sheath size
Process time independent of surface area	Inhomogeneous implant energy distribution
Charge neutralization by plasma	Target must be conductive
Compatibility with deposition tools	In-situ dose monitoring difficult
Cheap acquisition & maintenance	

plasma sheath are implanted. There is no mass separation and the potential across the sheath always varies slightly. The result is an inhomogeneous implant energy distribution inherent to PII. The situation even worsens if the target is an insulator which requires additional efforts. Significant surface charging and an additional mesh to accelerate ions are the two major challenges faced with non-conductive targets in PII. In-situ dose monitoring is difficult to achieve since the probe must be in the vicinity of the target, thus distorting the electric field. The bottom line is that the measurement slightly alters dose and energy distribution. Lastly, the instrumentation for PII systems does require less space due to the simpler principle and is also about an order of magnitude cheaper to acquire and maintain.

Instrumentation

A typical PII system consists of the chamber holding a precursor gas, a device to ionize the gas, a vacuum system, some device to supply high voltage to a sample holder and diagnostics to monitor the all of the other components. Most systems use pulses of high-voltage to reduce stress on the equipment, prevent arcing and allow the sheath regions to refill the implanted ions. The chamber sizes vary between 0.05 m^3 (typical semiconductor processing chamber) and 8 m^3 (Los Alamos). Further size comparisons of PII systems are given in Ref [10]. Common to all applications of PII is that large and sometimes complex areas are implanted simultaneously from all relevant faces, be it semiconductor wafers, artificial hip bones or an array of 1000 automotive pistons. The setup at the Plasma Physics Laboratory (PPL) at the

University of Saskatchewan (U of S) has average specifications for a semiconductor processing setup.

History

The foundation to the theory of PII was laid in the late 1960's when Widner, Lonngren and Alexeff[1] discovered transient sheaths [12] and calculated the generation of ion-acoustic waves at a negatively pulsed plate [13]. They obtained the two most important quantities for the PII theory, time-dependent ion flux and the ion energy, as a by-product of their work. Almost 20 years later, Adler [14] used a pulsed vacuum arc source to perform the first metal ion beam implants with an instrumentation similar to modern PII setups. The work of Conrad [15, 16] in 1986 is usually regarded as the birth of PII. Semiconductor applications were pioneered by Mizuno who developed a PII room-temperature process using a high density plasma which was fully compatible with conventional semiconductor processing [17]. In 1997, Chu's group demonstrated the PII production of full 100-mm silicon-on-insulator (SOI) wafers [18] which have been crucial for microprocessor production for a decade.[2] I present the basics of the PII theory and semiconductor applications in my history review; a very extensive discussion of the historical developments from the first 'Kanalstrahlen'[3] [20] to the state of the art of PII at the time of print may be found in the Handbook of Plasma Immersion Ion Implantation [10]. The book contains further introduction to the physics and instrumentation of PII. The reviews by Anders [21, 22], Chu [23], Ensinger [24] as well as Möller [25] also contain appealing presentations of many aspects of PII.

[1] I met Igor Alexeff at the 49th Annual Meeting of the Division of Plasma Physics 2007 in Orlando, where I presented my research on carbon-implanted silicon [11] and where he was the session chair. Happy that someone showed up early for the session, I got a quick lecture on the history of plasma waves, electron heating and other topics.

[2] The SOI technology is now on the verge of being replaced by high-k metal insulators. An excellent introduction to the topic may be found in Physics Today [19].

[3] German for 'canals rays' which are known as ion beams in modern language.

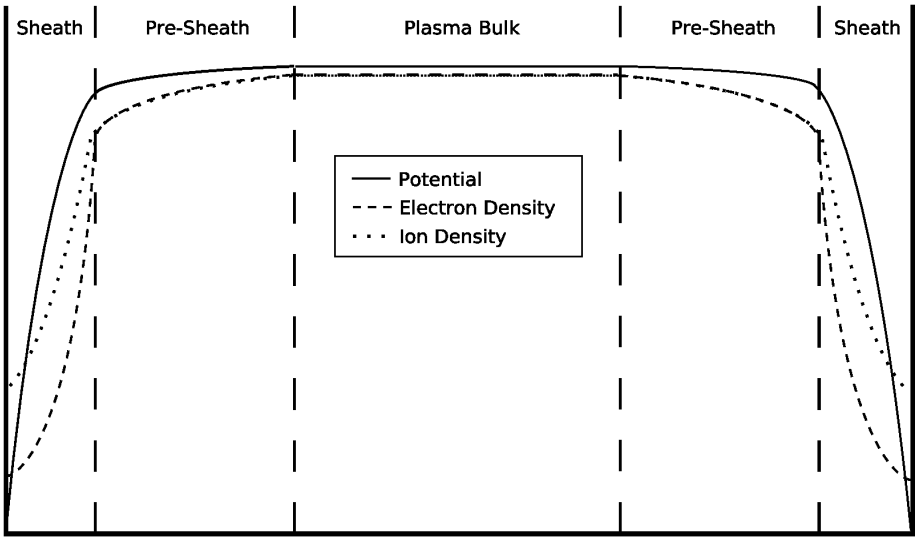

Figure 2.2. Sketch of the potential and the densities in a plasma confined between grounded walls.

2.2 Sheath Concepts

Plasmas are quasi-neutral overall, meaning there are equal numbers of ions and electrons, even though local space charges are possible. A positively charged ion-rich region, called the sheath, forms in the vicinity of grounded conductors when they are inserted into a plasma. Fig. 2.2 shows electron and ion densities for the example of a plasma confined between two grounded walls. Three distinct regions can be identified: the sheath, the pre-sheath and the plasma bulk. The properties of the pre-sheath and various sheath scenarios will be derived and discussed for a collisionless plasma in the following sections.

2.2.1 Quiescent Sheath and Pre-Sheath

As the potential is constant in the bulk, the differing electron and ion densities in the sheath can be explained by the difference in the thermal velocities of electrons and ions caused by the difference in their masses and temperatures. The net positive charge density in the sheath leads to a potential profile that is positive within the plasma bulk and falls sharply near the conducting walls, see Fig. 2.2 or Fig. 2.3 a).

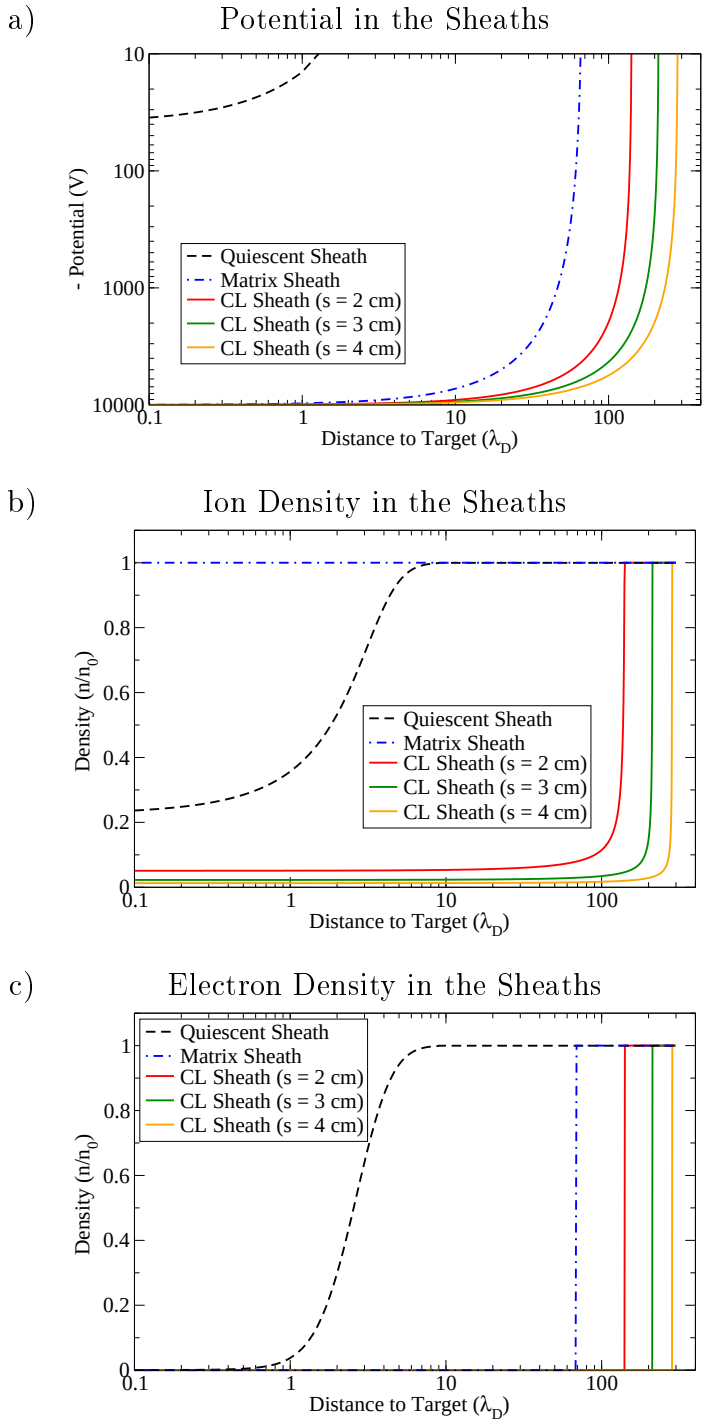

Figure 2.3. Comparison of the quiescent, Matrix and Child-Langmuir sheaths. The latter two sheath types were calculated for a target potential of 10 kV. The evolution of the Child-Langmuir sheath can be deduced from snapshots at different times. The top graph shows the potential (a). The ion (b) and electron density (c) are also compared.

The plasma bulk acts as a confining valley for the electrons and as a hill for ions because the electric field lines within the sheath point from the plasma to the wall. Thus the force on the electrons is directed towards the plasma, so that lower-energy electrons traveling toward the conducting wall are reflected back into the plasma. Conversely, ions from the plasma that enter the sheaths are accelerated toward the conducting wall. A useful definition of the sheath edge is the boundary at which the mean thermal energy of the electrons equals the potential due to the ions. The potential within a plasma is given by Poisson's equation

$$\nabla^2 V(x) = \frac{e}{\varepsilon_0}\left[n_e(x) - n_i(x)\right], \tag{2.1}$$

where $V(x)$ is the potential in the plasma, e is the elementary charge, ε_0 is the permittivity of free space, $n_e(x)$ and $n_i(x)$ are the electron and ion densities within the sheath.

Electron and Ion Density

The electron density can usually assumed to be Maxwellian-distributed and is thus

$$n_e(x) = n_s \cdot \exp\left(\frac{eV(x)}{kT_e}\right), \tag{2.2}$$

where n_s is the density at the sheath edge and kT_e is the electron temperature. The ion density can be derived from energy conservation and continuity at the sheath edge

$$n_i(x) = n_s\left(1 - \frac{eV(x)}{\frac{1}{2}m_i u_B^2}\right)^{-1/2} \tag{2.3}$$

with $\frac{1}{2}m_i u_B^2$ as the kinetic energy of the ions having mass m_i and velocity u_B at the sheath edge. The electron and ion density as a function of the Debye length are plotted in Fig. 2.3 b) and c), respectively.

Debye Length

Poisson's equation can be approximated by the linear terms if the potential $V(x)$ is small compared to the ion kinetic energy $\left(eV \ll \frac{1}{2}mu_B^2\right)$:

$$\frac{d^2}{dx^2}V(x) \approx \frac{e^2 n_s}{\varepsilon_0 kT_e}V(x) \equiv \frac{V(x)}{\lambda_D^2}. \tag{2.4}$$

This defines the Debye length λ_D which is a measure of the electrostatic shielding distance within the plasma. The Debye length in a plasma with bulk density $n_0 = 1.2 \times 10^{16}$ ions/m^3 and electron temperature $kT_e = 4.34$ eV is $\lambda_D = 141$ μm.

Potential

The potential which satisfies eq. (2.4) between two floating walls with the origin $x = 0$ in the middle is [9]

$$V(x) = V_0 \cdot \exp\left(-\frac{|x|}{\lambda_D}\right), \tag{2.5}$$

where V_0 is the potential difference between the wall and the plasma. Equating the electron and ion fluxes at the wall yields [26]

$$V_0 = -\frac{kT_e}{2e} \ln\left(\frac{m_i}{2\pi m_e}\right), \tag{2.6}$$

where T_e is the electron temperature, m_i and m_e are the effective ion mass and the electron mass. The wall potential with respect to the electropositive plasma is $V_0 = -19.4$ V for $kT_e = 4.34$ eV and $m_i = 26$ u[4]. The formula is only approximately valid for the grounded walls in our setup. The potential in the quiescent sheath is shown in Fig. 2.3 a).

Pre-Sheath

The solution for the potential in this simplified case always exists. This is not the case if all terms are kept. Bohm [27] showed that the basic nonlinear equation of sheath dynamics

$$\frac{d^2}{dx^2}V = \frac{en_s}{\varepsilon_0}\left[\exp\left(\frac{eV}{kT_e}\right) - \left(1 - \frac{eV}{\frac{1}{2}m_i u_B^2}\right)^{-1/2}\right] \tag{2.7}$$

has physical solutions with an electron repelling sheath [9] only for

$$u_B \geq \sqrt{\frac{kT_e}{m_i}}. \tag{2.8}$$

[4]The unit u (unified atomic mass unit) was chosen for the ion masses to simplify the calculation of ion-electron mass ratios. The mass of the electron m_e is 1/1833 u.

This inequality is called the Bohm sheath criterion. It was reviewed by Riemann [28] who showed that the criterion also applies in RF discharges [29]. A finite initial ion energy requires electric fields to be present in a region further away from the wall than the sheath. This region is called pre-sheath and extends typically much wider than the sheath. The pre-sheath is quasi-neutral unlike the sheath, but electric fields can exists in both. The potential drop across the pre-sheath necessary to facilitate the Bohm velocity $u_B = \sqrt{kT_e/m_i}$ is the plasma potential:

$$V_p = -\frac{m_i u_B^2}{2e} = -\frac{kT_e}{2e}. \tag{2.9}$$

The density at the interface between sheath and pre-sheath can therefore be calculated by substitution of the plasma potential into eq. (2.2)

$$n_e = n_0 \cdot \exp\left(-\frac{e}{kT_e}\frac{kT_e}{2e}\right) = n_0 \cdot e^{-1/2} \approx 0.61 \cdot n_0, \tag{2.10}$$

where $n_e \approx n_i = n_s$ is the density at the sheath edge and n_0 is the density in the plasma bulk.

2.2.2 High-Voltage Sheaths

If one of the walls in the preceding example is biased to a high negative voltage, electrons are repelled quickly and the sheath consists entirely of ions.

Matrix Sheath

In a Matrix sheath, the ions are distributed uniformly in the absence of electrons. The electric field varies linearly with position. The potential is then parabolic

$$V(x) = -\frac{en}{\varepsilon_0}\frac{x^2}{2}. \tag{2.11}$$

The sheath will extend until the charge of the ions cancels the high-voltage potential at the wall. The potential drop across the sheath is thus the potential at the wall $V(s) = -V_0$. Solving for the sheath width gives

$$s_M = \sqrt{\frac{2\varepsilon_0 V_0}{en}} = \lambda_D \sqrt{\frac{2eV_0}{kT_e}}. \tag{2.12}$$

This sheath width is of the order of tens of Debye lengths for typical target potentials in PII. A target bias of $V_0 = 10$ kV, in a plasma with electron temperature $kT_e = 4.34$ eV and Debye length $\lambda_D = 141$ μm yields a Matrix sheath width of $s_M = 68 \times \lambda_D = 9.6$ mm.

The characteristic time scale to establish this situation is given by the time it takes an electron to travel across the collisionless sheath with kinetic energy

$$eV_0 = \frac{1}{2} m_e u_{0,e}^2. \tag{2.13}$$

The result is a reaction time of the order of the inverse electron plasma frequency

$$\tau_e = \frac{s_M}{u_{0,e}} = \frac{\sqrt{2\varepsilon_0 V_0/en}}{\sqrt{2eV_0/m_e}} = \sqrt{\frac{m_e \varepsilon_0}{ne^2}} = \omega_e^{-1}, \tag{2.14}$$

which is about 0.2 ns for the conditions stated in Table 5.2.

Child-Langmuir Sheath

The conditions under which the Matrix sheath can exist are short-lived as the ions move in response to the negative potential at the wall after a time of the order of the inverse plasma ion frequency

$$\tau_i = \frac{s_M}{u_{0,i}} = \omega_i^{-1} = \sqrt{\frac{m_i \varepsilon_0}{ne^2}}, \tag{2.15}$$

which is about 35 ns for the conditions given by Table 5.2 and hence much longer than the 0.2 ns it takes the electrons to react to the electric field. The ions are accelerated toward the wall and buried below the surface. Their positive charge, which had previously balanced the negative potential at the wall, is decreased and the electric field can penetrate deeper into the pre-sheath. This rejects more electrons and moves the sheath edge deeper into the pre-sheath. The energy distribution of the ions in this phase depends on their location within the sheath. As more and more ions are uncovered by this process, both sheath width and the current of ions toward the wall will reach a steady state. The current is now subject to the space charge in the sheath. The sheath in this situation is called Child-Langmuir (CL) sheath after the Child-Langmuir law [30]

$$J_{CL} = \frac{4}{9}\varepsilon_0\sqrt{\frac{2e}{m_i}} \cdot \frac{V^{3/2}}{s^2}, \tag{2.16}$$

which treats the plasma like a (planar) diode with the sheath width s as the distance between cathode (negatively biased target) and anode (positive ions in the sheath).

The potential within the CL sheath is derived from the conservation of energy in the limit of small initial ion kinetic energies and the continuity equation which is set equal to eq. (2.16). Poisson's equation is in this case

$$\frac{d^2V}{dx^2} = -\frac{J_{CL}}{\varepsilon_0}\left(-\frac{2eV}{m_i}\right)^{1/2} = \frac{e}{\varepsilon_0}n_i. \tag{2.17}$$

Integration with the boundary conditions $V = dV/dt = 0$ yields the potential relative to the sheath edge at x = 0

$$V(x) = -V_0\left(\frac{x}{s}\right)^{4/3}, \tag{2.18}$$

which is plotted in Fig. 2.3 a). Substitution of this potential into Poisson's equation gives the ion density

$$n_i(x) = \frac{4}{9}\frac{\varepsilon_0}{e}\frac{V_0}{s^2}\left(\frac{x}{s}\right)^{-2/3}. \tag{2.19}$$

This expression is not finite as x approaches zero because the initial ion kinetic energy was neglected in the derivation of the Poisson's equation in eq. (2.17). The current in steady-state is given by the Bohm current $J_B = enu_B$ which may be used to solve eq. (2.16) for the final sheath width

$$s_{CL} = \frac{\sqrt{2}}{3}\lambda_D\left(\frac{eV}{kT_e}\right)^{3/4} = \frac{1}{3}\left(\frac{eV_0}{kT_e}\right)^{1/4}s_M. \tag{2.20}$$

This result will again be derived with greater detail in section 5.2.1 for a different situation. The Child-Langmuir sheath is generally more extended than the Matrix sheath and can be of the order of 100's of Debye lengths. An electrode potential of $V_0 = 10$ kV and an electron temperature of $kT_e = 4.34$ eV gives a Matrix sheath width of $s_M = 9.6$ mm. The Child-Langmuir sheath that develops will extend to $s_{CL} = 157\times\lambda_D = 2.2$ cm.

Fig. 2.3 shows the potential, ion density and electron density as a function of the Debye length for all three situations: quiescent sheath, Matrix sheath and Child-Langmuir sheath.

2.3 Secondary Electrons

If the kinetic energy of ions impinging on a target is sufficiently larger than the target material's work function, multiple electrons can be ejected. Electrons other than the first one are called secondary electrons. The negative electrons are accelerated in the direction of the plasma bulk by the same electric field that guided the positive ions to the target. Ref [10] contains a detailed discussion of secondary electrons' role in the ion implantation process, PII instrumentation and radiation safety. Steenkamp [31] discusses the latter two points for the setup at the U of S Plasma Physics Laboratory.

Relation to the Measured Current

The measured current output of the plasma chamber is related to the plasma ion current by the secondary electron emission current

$$I_{\text{measured}} = [1 + \gamma(V)] \cdot I_{\text{plasma},i}, \tag{2.21}$$

where the material-dependent secondary electron emission coefficient $\gamma(V)$ is given by

$$\gamma(V) = \gamma(V, \text{surface}, t) = \begin{cases} \alpha(\text{surface}, t) \cdot \sqrt{V} - \beta(\text{surface}, t), & \left(\alpha \cdot \sqrt{V}\right) \geq \beta \\ 0, & \text{else} \end{cases} \tag{2.22}$$

with V as the potential in volts. The coefficients α and β are heavily dependent on the surface conditions [32, 10], such as the roughness and charge states. Those conditions also change in time until the surface is saturated and additional impinging ions do not affect the conditions at the surface [32]. The first coefficient α has units of electrons per $\sqrt{V}$. For convenience, I will use the number of electrons emitted at 10 kV

$$\alpha^* = \alpha \cdot \sqrt{10,000} \tag{2.23}$$

in the discussion. The coefficients α are tabulated for a large number of gases and target materials, but those values are for atomically clean target surfaces and condi-

tions different from those during plasma ion implantation. The second coefficient β is a unitless threshold value for secondary electron emission to occur.

Contribution to the Sheath's Space Charge

Each incident ion triggers the emission of multiple secondary electrons in a typical PII process, but they do not contribute to the space charge in the sheath due to their high velocity. The ion I_i and secondary electron currents I_γ during implantation with an ideal pulse are

$$J_i \approx e n_i \sqrt{2eV_0/m_i} \tag{2.24}$$

and

$$J_\gamma \approx e n_{se} \sqrt{2eV_0/m_e} \equiv \gamma \cdot J_i, \tag{2.25}$$

where e is the elementary charge, V_0 is the potential of the pulse, m_i and m_e are the masses of electrons and ions, respectively. The ratio of the secondary electron density in the sheath n_{se} to the ion density in the sheath n_i is

$$\frac{n_{se}}{n_i} \approx \gamma \sqrt{\frac{m_e}{m_i}} = \frac{\gamma}{43\sqrt{M}}, \tag{2.26}$$

where γ is the number of secondary electrons emitted at V_0 and M is the number of nucleons in the ion molecule. For an N_2 plasma and a surface that emits about 1 secondary electron at -10 kV, the ratio is approximately 1:220 $\ll 1$. Thus, the space charge in the sheath is not influenced by the secondary electrons.

Ionization of Neutrals

Even though the large number of secondary electrons does not contribute to the space charge in the sheath, their presence still influences the sheath region. They can ionize the neutral gas molecules and thereby increase the ion density during high-voltage implantation. This was observed by several groups [33, 34, 35, 36, 37] and can also be seen as an increased steady-state current in my raw data (Fig. 3.5). Bradley [38] recently discussed the role of a plasma-beam instability for the ion enhancement through secondary electrons. However, the exact mechanism of the

coupling of secondary electrons to the neutral plasma molecules is not yet fully understood and remains an active field of research at the U of S Plasma Physics Laboratory.

Chapter 3

PII Apparatus

3.1 Overview of the Components

An overview of all components of the setup is shown in the Fig. 3.1. The apparatus is roughly grouped into into three sections: high voltage on the left, plasma processing in the middle and plasma control on the right. The various units will be discussed briefly in the following paragraphs.

High-Voltage

The high voltage pulses are supplied by stacks of custom built Marx stage modulators which were designed by J.T. Steenkamp [31, 39, 40]. The Marx stages setup as of Spring 2008 is depicted in Fig. 3.2. The pulse height is given by

$$V = V_{DC} \times (\#\text{ stages}) \times (\text{ratio})\,, \tag{3.1}$$

where V_{DC} is the voltage output of the custom-built DC supply (max 1 kV), (# stages) are the stages installed and (ratio) is the step-up ratio of the transformer (or 1 if no transformer is connected). A voltmeter near the dial of the DC power supply can be used to monitor the DC output voltage V_{DC} after a 1:100 voltage divider.

Two modes may be selected by changing the wire connections between the Marx stages and the ICP chamber. The circuit diagrams are shown in Fig. 3.3. In the 'Transformer Mode', a Westinghouse 610J647H01 step-up transformer (1:10) as well as a 2 kΩ shunt resistor are connected between the HV pulse output and the plasma chamber, yielding a greater penetration ion depth at the cost of a wide spread in the ion energy distribution, see discussion in Section 7.4. The 'Marx Mode' produces a

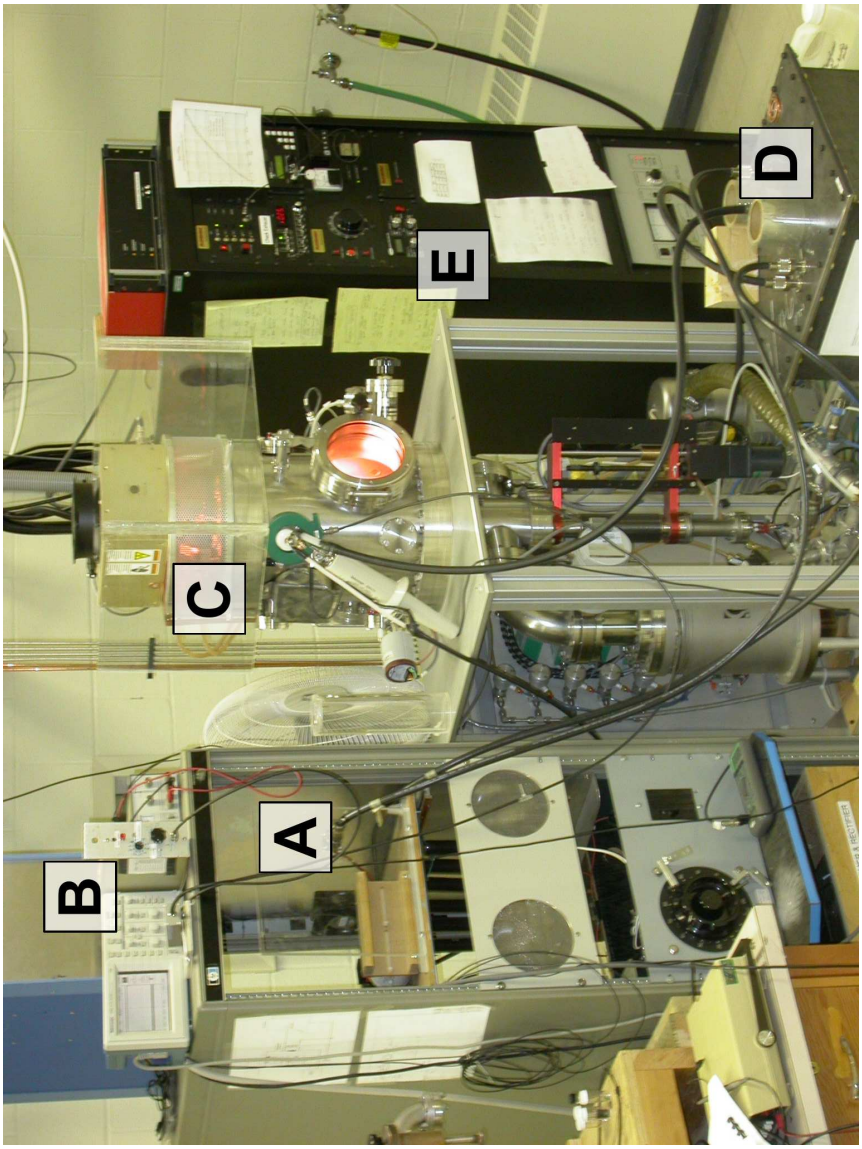

Figure 3.1. The Plasma processing setup as of Spring 2008. (A: Marx II pulser; B: Pulser Control; C: Processing Chamber; D: Transformer; E: Gas & Plasma Control.)

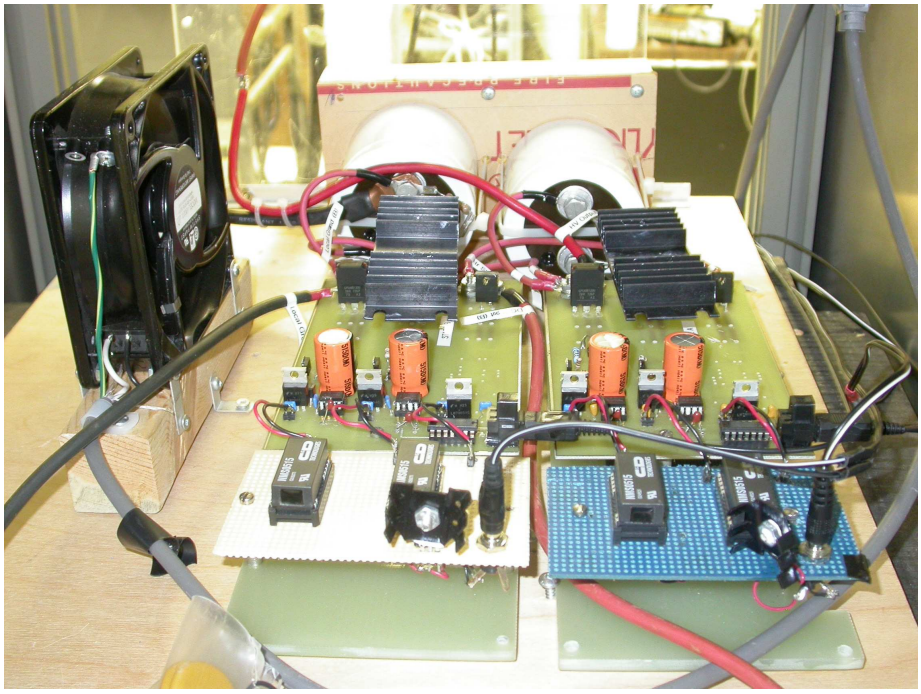

Figure 3.2. The Marx stages setup as of Spring 2008.

narrower ion energy distribution but is limited to an output of 1 kV per stage. Two stages are currently installed and their design allows for efficient operation of 8 to 10 stages in total [31]. The electrode potential, the current output and the calculated ion energy distribution of -1 kV pulses in both modes with the plasma load (electron temperature 4.34 eV, ion density 1.2×10^{16} m^{-3}) are compared in Fig. 3.4, Fig. 3.5 and Fig. 3.6, respectively. The standard operating mode is the 'Transformer Mode' in order to achieve a deeper penetration depth.

High-Voltage Control and Monitoring

The implantation duration (1 s to 90 min) and the pulse repetition rate (50 to 100 Hz) can be set using a custom-made pulse control box. The pulse width is hard-wired to 6.2 μs. The circuit diagram and a more detailed discussion can be found in J.T. Steenkamp's MSc thesis [31]. The changes I made to account for the pulse transformer's limitations are documented in Appendix A.1. A Tektronix probe model P6015A acquires the high voltage and a Pearson current probe model 150 (Rogowski coil) is utilized to obtain the current. Both are recorded to a Tektronix

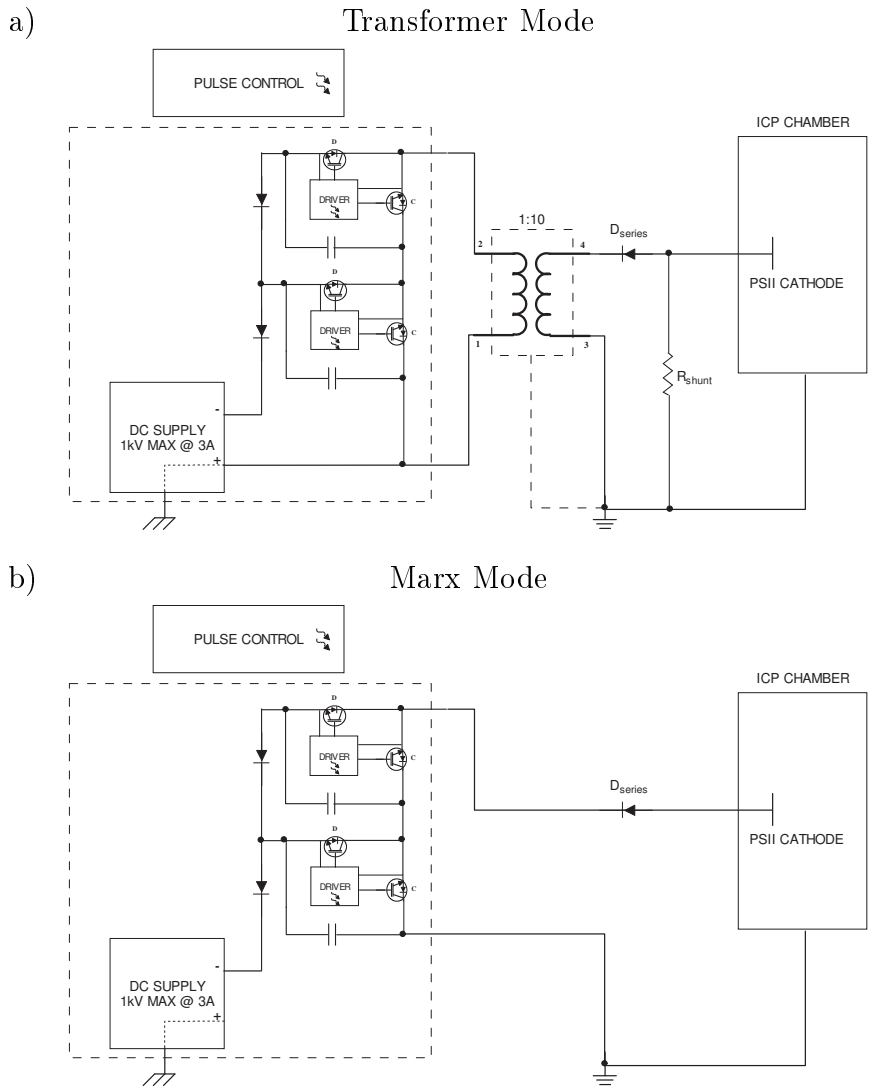

Figure 3.3. Schematic circuit diagrams for the 'Transformer Mode' a) and the 'Marx Mode' b). The diagram in a) was taken from Ref [31] with permission of the author.

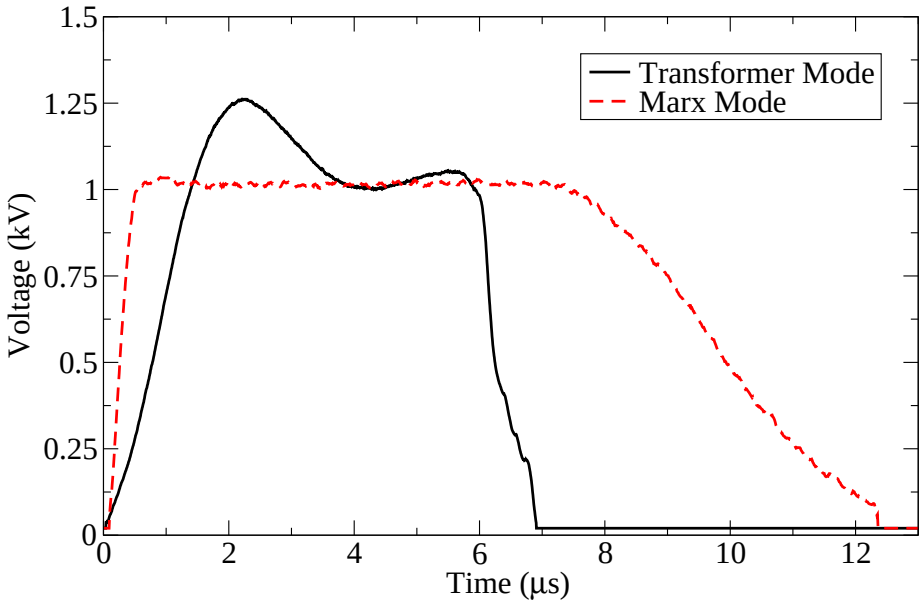

Figure 3.4. Comparision of the measured electrode potentials in the 'Transformer Mode' and the 'Marx Mode'.

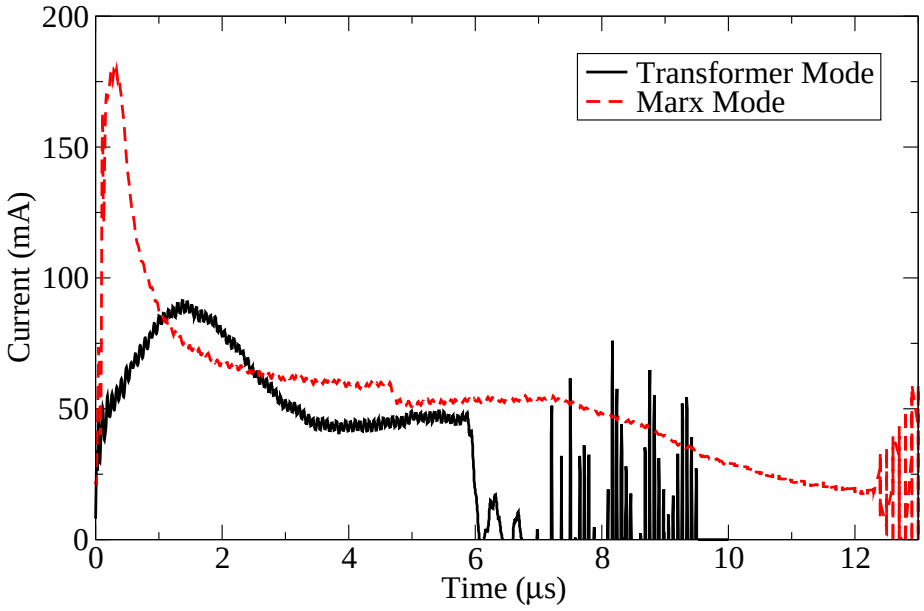

Figure 3.5. Comparision of the measured current at the high voltage feed-through (not corrected for secondary electron emission) in the 'Transformer Mode' and the 'Marx Mode'. The kink at 5 μs could be related to a synchronization problem we lately encountered with one of the stages.

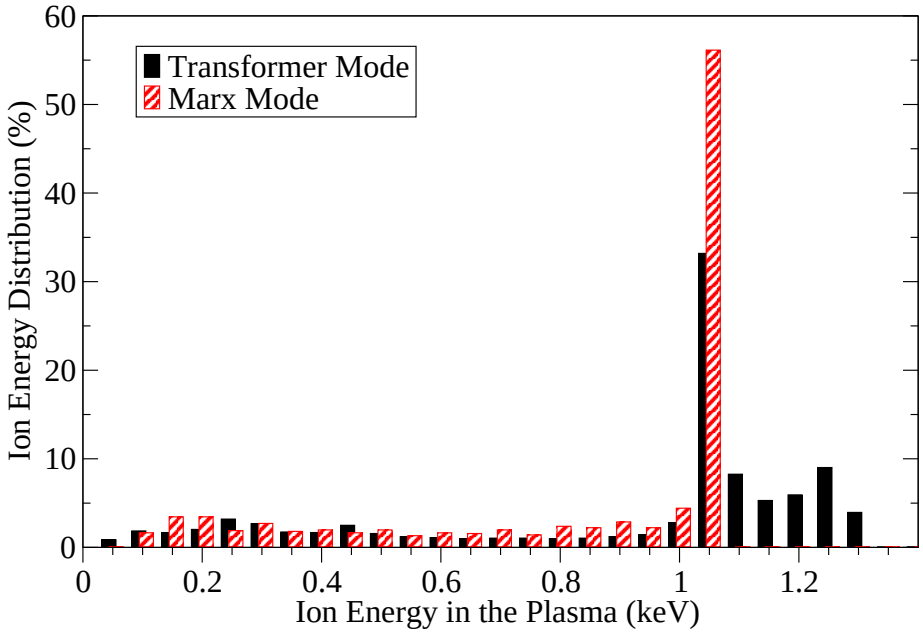

Figure 3.6. Ion energy distribution calculated for the 'Transformer Mode' and the 'Marx Mode' by the p2i software; see Section 5.6 for a discussion of the method.

TDS 210 Oscilloscope where the voltage is on channel 1 and current on channel 2 in the default configuration. The data is transferred to a PC using the software Tektronix Open Choice Desktop V1.10.

Processing Chamber

The inductively coupled plasma (ICP) chamber was manufactured for Prof. Akira Hirose at the U of S Plasma Physics Laboratory by Plasmonique Inc., 1650 Boul. Lionel-Boulet, Varennes, QC Canada. We are grateful for the permission to use his chamber for this project. A close-up photograph of the chamber and its diagnostic devices is provided in Fig. 3.7. The chamber is cylindrical with 29.8 cm inner diameter and 37.5 cm height. The gas inside is ionized by electrons heated by induced radio-frequency (RF) electric fields at a frequency of 13.56 MHz through a quartz window via a water-cooled coil on top of the processing chamber. The chamber is capped by a Comdel match pro cpm-1000 matching network part FP2216R1 which is discussed in Hong Li's MSc thesis [41].

The stainless steel sample holder is disk-shaped and features two thin bars to

hold samples in place. A photograph can be found in Fig. 3.8 and the blueprint is in Appendix A.2. The sample holder is mounted radially on a rod which exits the chamber through the high-voltage feed-through and is about 10 cm from the quartz window. The setup is rated for voltages up to 30 kV [31].

Langmuir Probe

The port radially opposite of the sample holder is occupied by a Langmuir probe which can be moved to within a few centimeters of the sample holder for measurements. The probe is made from tungsten wire and is not capacitively compensated. The inner diameter is 0.31 mm and the length of the tip exposed to the plasma is 5 mm. The remaining area is insulated by an alumina sleeve which itself is surrounded by a grounded stainless steel jacket. RF frequencies are eliminated by wrapping the cable between the probe and the voltage supply around a yoke. The voltage is supplied by a Kepco BOP-1M 4888 power supply which is modulated by an HP function generator 3311A. The sweep frequency was typically $\sim$25 Hz for which no hysteresis effect were observed. Voltage and current are recorded on another Tektronix TDS 210 using the convention described in the high-voltage control and monitoring paragraph. The plasma current is obtained from the voltage drop over a 1 kΩ resistor to conveniently read milliamperes for volts. The voltage applied to the probe is given by the difference of channel 1 and channel 2. Fig. 3.9 depicts the setup for Langmuir probe measurements. Tusyewski and Tobin [42] estimated that the error due to a simple setup is about 10% to 12%.

Plasma and Gas Control

The chamber is evacuated by a LH Trivac D8A roughing pump down to 20 mTorr in a few minutes and then brought down to pressures of typically low 10^{-7} Torr by a Leybold turbo-molecular pump model He-500 within 12 hours. This low base pressure is necessary to prevent contamination due to implantation of unwanted ions. The ratio of working pressure ($\sim$mTorr) to the base pressure of 1:10,000 translates into 1 unwanted ion in 10,000 ions of the processing gas. A Granville Phillips Micro-

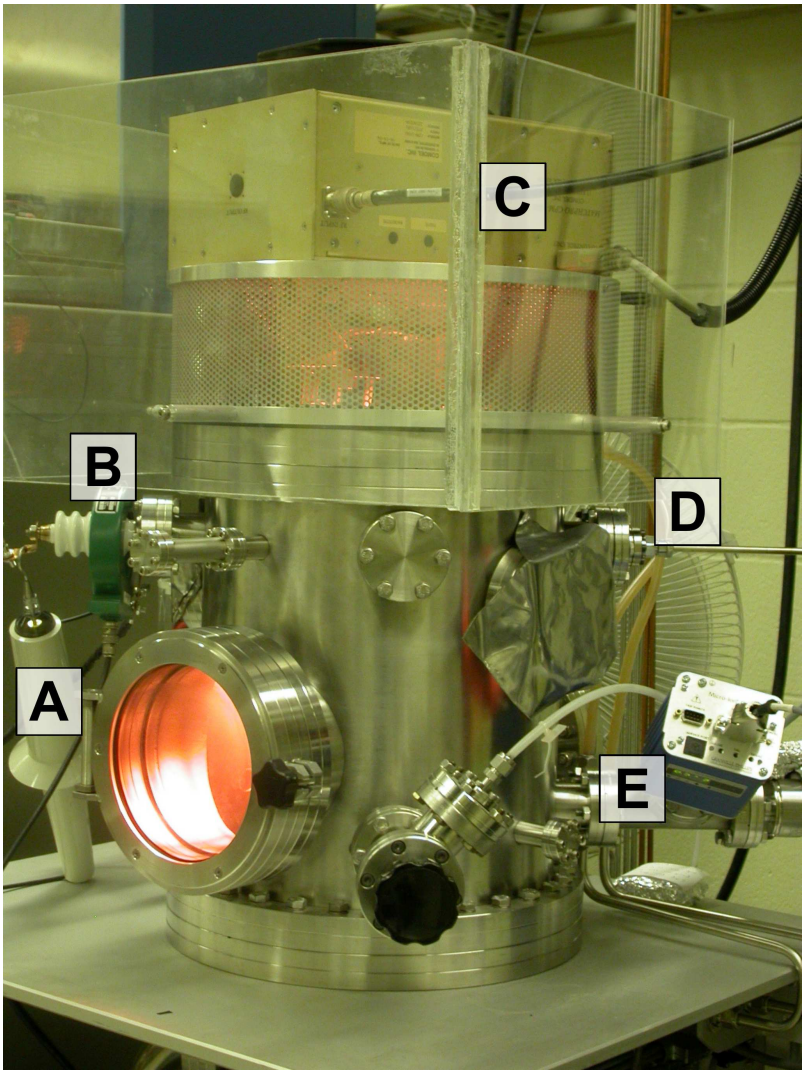

Figure 3.7. The Plasma processing chamber and diagnostic devices as of Spring 2008. (A: High-Voltage Probe; B: Current Probe; C: Matching Network; D: Langmuir Probe; E: Ion Gauge.) We are grateful to Prof. A. Hirose for the permission to use his chamber in this study.

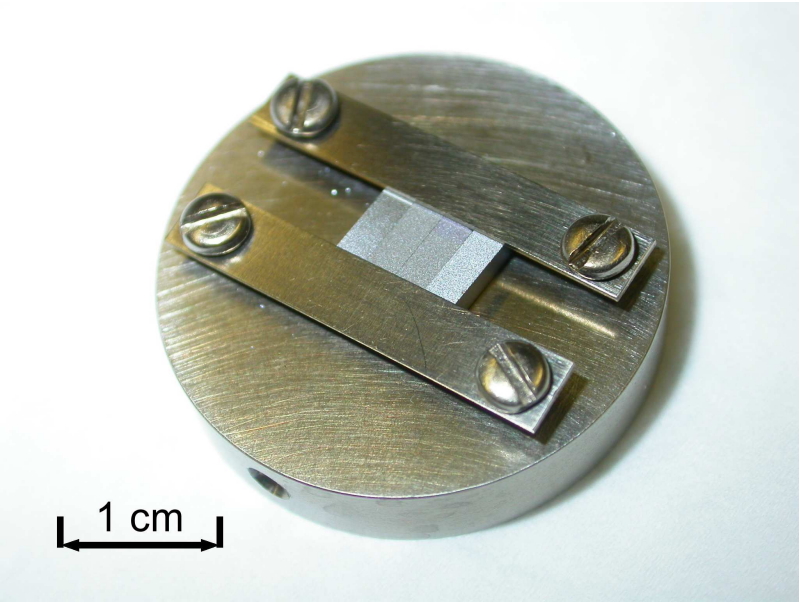

Figure 3.8. The sample holder for gallium arsenide implants.

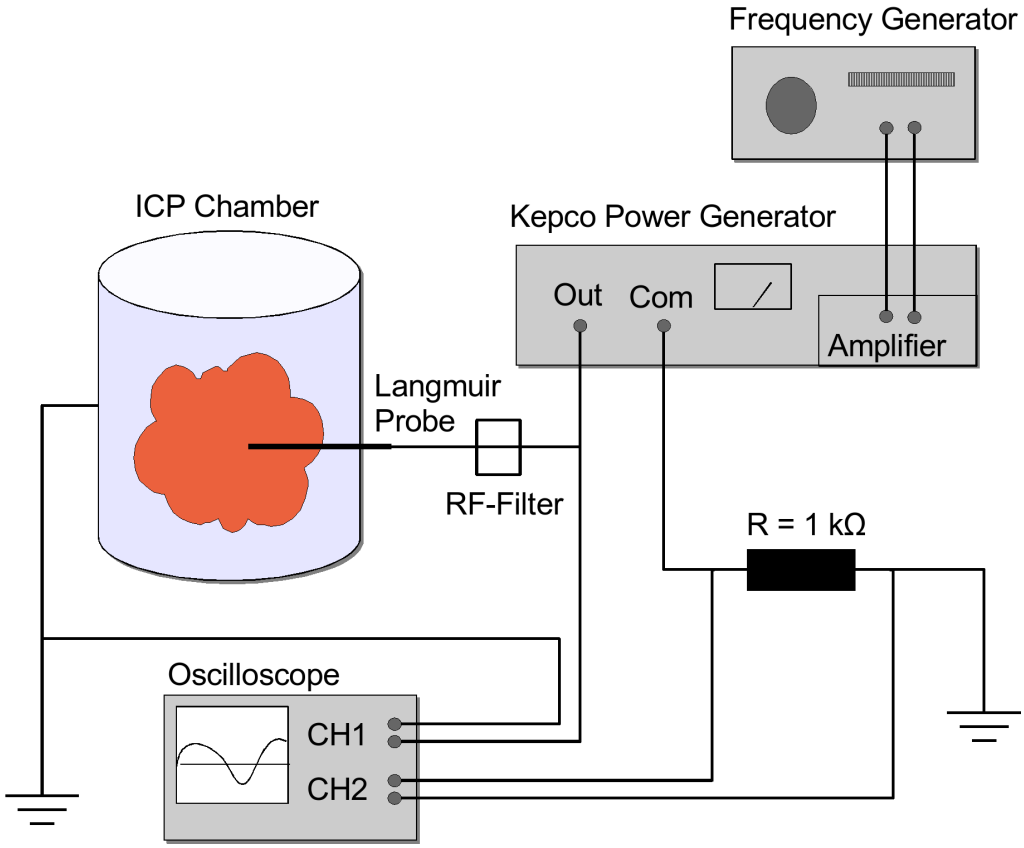

Figure 3.9. The Langmuir probe setup.

Table 3.1. Independent parameters of ion implantation.

Parameter	Value
Base Pressure	$< 3 \times 10^{-7}$ Torr
Working Pressure	3±1 mTorr
Gauge Position	70%
Gas	nitrogen
RF Power	400 W
Series Matching	60.5%
Shunt Matching	78.9%

Ion Plus Gauge Model 356-002 is connected to the chamber to read the base pressure. Its heat loss sensor is active from atmospheric pressure to 3×10^{-2} Torr, then the signal is mixed with the ion gauge turning on in 'low emission' up to a pressure of 3×10^{-3} Torr. The low emission mode is active until the pressure drops below 5×10^{-6} Torr which triggers the 'high emission' mode. The accuracy is ±15% of reading for pressures up to 50 Torr[1].

The rack at the rightmost of the setup features an MKS Type 247 flow controller, MKS Type 651 pressure controller for a MKS valve type 653B-13048 to set the working pressure which is measured by a MKS 622A-21745 transducer. This combination is accurate to within 1 mTorr if the sensor has been zeroed correctly[2]. Thus, the position of the valve was also recorded to increase repeatability of the conditions, see Table 3.1. Lastly, the section contains a Comdel match pro cpm-1000 impedance matching unit FA0 718 for the ENI OEM-6A-11491-51 radio frequency (RF) solid state plasma power supply. The series and shunt capacitance was adjusted until the reverse power was below the detection limit of 5 W. The reading of the matching unit for minimal reverse power are given in Table 3.1.

[1]The manual does not include the accuracy for the gauge. Customer support emailed me the value upon request.

[2]The manual does not include the accuracy of the transducer. Customer support emailed me the value upon request.

Table 3.2. Properties of ICP plasmas. Values from [10].

Property	Range
Density	$10^{16} - 10^{18}\mathrm{m}^{-3}$
ICP Power Transfer	50 - 90%
Electron Temperature	1 - 5 eV
Ion Temperature	0.1 - 0.5 eV
Plasma Potentials	10 - 30 V
Radio Frequency	0.1 - 100 MHz

3.2 ICP Plasmas

Inductively coupled plasmas (ICP) are well suited for plasma ion implantation as they provide stable and and clean plasmas over wide range of gas pressures. The most important properties for plasma ion implantation and their ranges are compiled in Table 3.2.

The coil which ionizes the gas sits outside the chamber which minimizes contamination of the plasma as well as wear of the coil. A wide range of radio frequencies (RF) are utilized. Popular choices are 13.56 MHz and harmonics 6.78 MHz and 27.12 MHz as well as frequencies lower than 0.46 MHz. The 13.56 MHz frequencies (used at the U of S Plasma Physics Laboratory) and harmonics gain their popularity from their historical assignment to high-voltage applications and the low, sub MHz, frequencies offer an increase in the power transfer from the coil to the plasma at lower frequencies [10]. In any case neither of the popular frequencies interfere with public or military broadcast bands. Typical skin depths in the plasma are of the order of a few centimeters at 13.56 MHz which means that the sample holder in our setup is surrounded by a maximally ionized plasma.

Other benefits of ICP discharges are that the electron and ion densities are nearly equal and that the electron energy distributions are close to Maxwellian [10]. Furthermore, the density profile over the plasma chamber varies only by a few percents for low pressures ($<$ 100 mTorr). In general, higher mean free paths of the ions

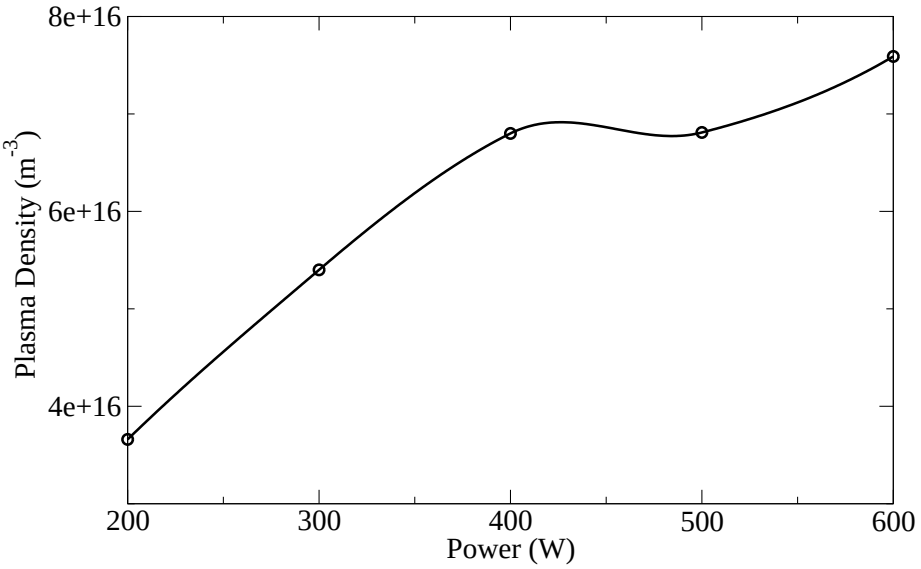

Figure 3.10. Measured plasma density as function of power. The densities were obtained from Langmuir probe measurements and are too high by a factor of 6, see discussion in Section 4.3. However, the general trend is not affected by the multiplicative factor.

broaden the plasma density profile.

3.3 Considerations

3.3.1 Power

The plasma ion density as a function of the RF coil's power is shown in Fig. 3.10. The data was extracted from Langmuir probe measurements as described in section 4.2. The density varies linearly with the power up to about 400 W. The measured density decreases at 500 W and rises up again when approaching 600 W. This local minimum is consistent with Langmuir probe measurements reported by Tuszewski and Tobin [42]. Based on these measurements, I chose to run the processing at 400 W to save energy. The minor increase of the plasma density at 600 W did not seem worth the extra expense of 200 W.

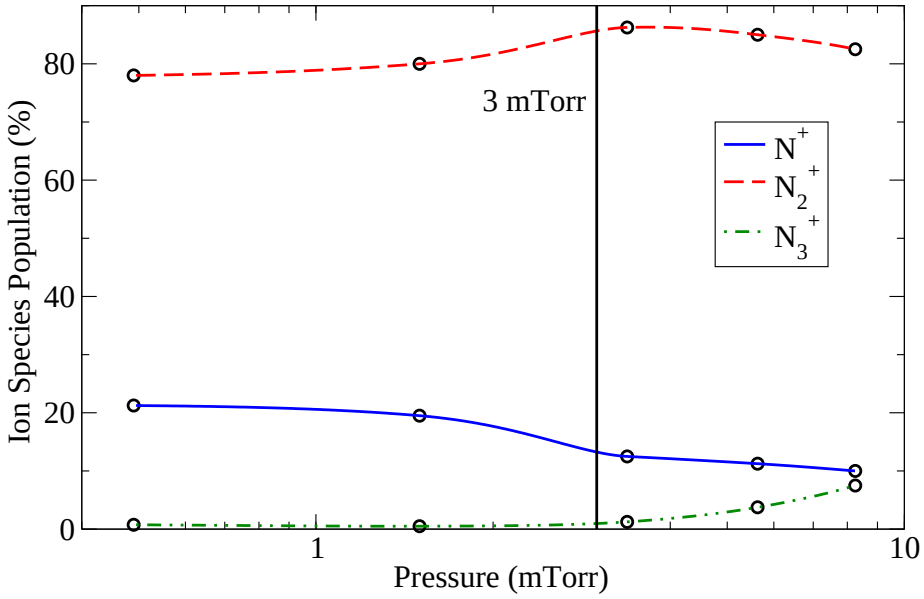

Figure 3.11. Variation of the nitrogen ion species in a 400 W ICP power source after Kim et al. [43].

3.3.2 Ion Populations

Kim et al. [43] studied the populations of nitrogen ion species for a wide range of powers and pressures in ICP (RF 13.56 MHz) processing plasmas. Their mass analyzer consists of a movable ion extraction system immersed in a plasma, a 60° permanent sector magnet, an ion energy modulator for beam scanning and an ion collecting Faraday cup. Fig. 3.11 shows their results for 400 W RF power. The black circles are the measured data points and the solid lines are fits obtained from an Akima spline algorithm. I obtained the following values for the pressure of 3 mTorr: 13.2% N^+ ions and 85.7% N_2^+ ions. The remainder of 1.1% was assigned to N_3^+ ions.

3.3.3 Surface Charging

The effective voltage on the target surface due to surface charging was studied by Emmert [44]. He found that the effective voltage on the surface of a dielectric, such as GaAs, is given by:

$$V_{\text{eff}} = \frac{V_0(t) - [n_0 e d (s - s_0) / (\varepsilon_0 \kappa)]}{1 + [4d/(3s\kappa)]}, \tag{3.2}$$

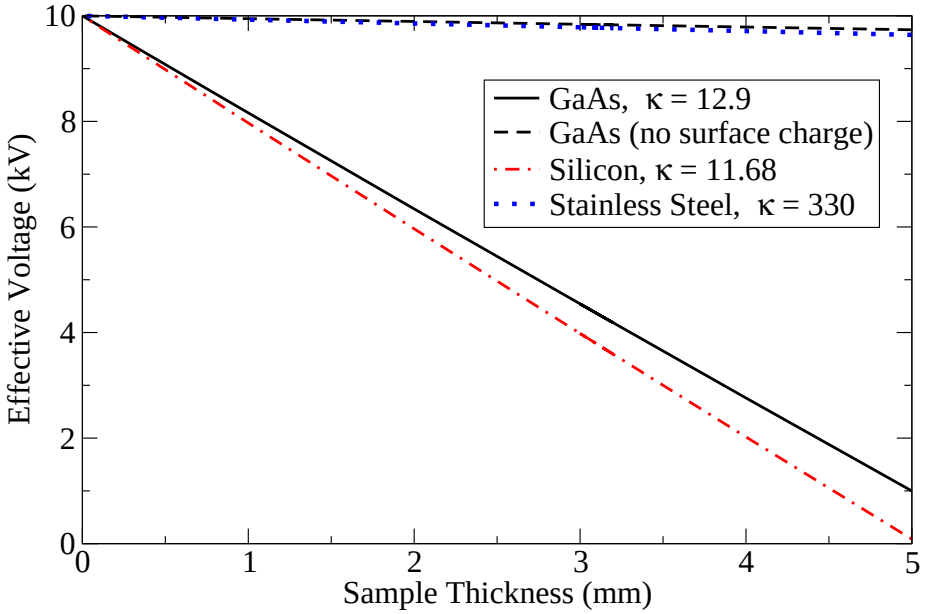

Figure 3.12. Surface charging for a 10 kV implant of popular implantation targets.

where $V_0(t)$ is the voltage applied to the sample holder, d is the thickness of the sample, $\kappa = 12.9$ is the sample's dielectric constant, n_0 is the plasma bulk density, s_0 is the quiescent sheath width (the sheath width prior to implantation) and $s = s(t)$ is the thickness of the expanding high voltage sheath. The second term in the numerator is the effect of accumulating charge and the denominator accounts for the change in the potential due to the thickness of the sample. The effective voltages for samples of various popular implantation targets of various thicknesses are plotted in Fig. 3.12. The effective voltage at the surface of a 2.1 mm GaAs target for a 10 kV pulse would be 6.1 kV if the sample sits on a sample holder. However, two thin stainless steel bars on top of the samples might mitigate the effect of surface charging (dashed black line in Fig. 3.12) significantly. The effective voltage is then almost the voltage at the sample holder, but the ions will be implanted at an angle slightly different from normal as the electric field lines are not perpendicular to the surface in this situation. The secondary electron emission can also significantly contribute to the surface charging as Lindner and Cheung [45] showed. The surface charging also depends on the pulse repetition rate. Those effects have been studied by Dai and Wang [46]. Short pulse widths and low repetition rates surface charging.

The effective voltage cannot be measured easily, but a measured ion depth profile can clearly show whether the ions were accelerated by 10 kV or 6.1 kV. The depth profile can also be used to some extent to detect the angle which the ions had upon implantation into the target.

3.3.4 Sample Heating

Sample heating has been studied experimentally [47] and theoretically [48]. I developed a simple model for an estimate of the temperature increase under the following assumptions:

1. Each ion has the same kinetic energy which is equal to the voltage at the plateau of the pulse (mono energetic ions)

2. The kinetic energy is completely converted into lattice vibrations, i.e. heat, when the ions are stopped at their final destination within the target. Changes in any of the potential energies of the target will not be considered. Furthermore, no ions are reflected at the target.

3. The target is thermally isolated and does not radiate heat.

4. The temperature of the sample is initially 300 K.

The following sample calculation will be carried out for a fluence of $F = 5 \times 10^{10}$ ions/cm^2 caused by an ideal -10 kV pulse. The energy Q deposited in the target is:

$$Q = A \cdot F \cdot KE, \tag{3.3}$$

where $A = 0.13$ cm^2 is the surface area of the target, $F = 5 \times 10^{10}$ ions/cm^2 is the fluence and $KE = 1.6 \times 10^{-15}$ J is the kinetic energy of the ions. The question of thermal conductivity must be answered next since the ions are implanted within a small volume just below the surface. If the target is such that both the thermal conductivity and the specific heat coefficient are low, then the temperature of the surface will increase greatly and melting will occur. The thermal conductivity of

GaAs at 300 K is $\delta = 46$ W/m/K [49] and the power due to implantation in my example is

$$P_{\text{impl}} = f \cdot Q = f \cdot A \cdot F \cdot KE, \tag{3.4}$$

where $f = 63.13$ Hz is the pulse repetition rate. The implanted power $P_{\text{impl}} = 8.32$ mW is small and the thermal gradient within the sample is therefore also small. The heat will be distributed over the entire volume of the sample. The heat capacity is defined by

$$Q = c_m \cdot m \cdot \Delta T, \tag{3.5}$$

where $c_m = 350$ J/K/kg [49] is the specific heat of gallium arsenide, $m = 126{\times}10^{-6}$ kg is the mass of the entire sample and ΔT is the temperature difference caused by the deposited energy. Combining eqs. (3.3) and (3.5) yields the temperature difference of the sample ΔT

$$\Delta T = \frac{A \cdot F \cdot KE}{c \cdot m}, \tag{3.6}$$

which is $\Delta T \approx 10^{-3}$ K in my example. For a total fluence of 10^{15} ions/cm^2 or in other units 6% nitrogen in GaAs, the target would be about 20 K hotter which is negligible.

The sample does not heat significantly due to ion implantation. However the stainless steel sample holder does due to a lower heat conductivity and ohmic heating. The thermal connection between sample and sample holder in vacuum and in a plasma is weak, so that the influence on the sample temperature is negligible. The low thermal interaction also means that the sample holder is very hot after implantations and the sample holder should be given a few hours to cool down.

Chapter 4

Experimental

4.1 GaAs Samples

The gallium arsenide (GaAs) samples for this study were bought from Wafer World Inc., 1100 Technology Place, Suite 104 - West Palm Beach, FL 33407. They were sold as test grade 6.4×3.2×3.2 mm^3 bars with unknown orientation. I measured a large number of the samples with a KAR Vernier caliper. The actual dimensions are $(6.1 \pm 0.1) \times (2.1 \pm 0.1) \times (2.1 \pm 0.1)$ mm^3 which gives at total sample volume of $V_{\text{sample}} = (27 \pm 2) \times 10^{-9}$ m^3. The masses of 10 samples were measured on a Mettler Toledo AB 204-5 laboratory scale. The sample mass is $m_{\text{sample}} = (126.4 \pm 0.2)$ mg. The error includes the scale's accuracy and spread amongst the samples. The calculated density for those samples $\rho_{\text{GaAs}} = (4700 \pm 320)$ kg/m^3 is about 12% smaller than the literature value for the density of crystalline GaAs (5320 kg/m^3) [6]. The number density was calculated from

$$n_{\text{GaAs}} = \frac{\rho_{\text{GaAs}}}{M_{\text{GaAs}}} N_A, \tag{4.1}$$

where $M_{\text{GaAs}} = 144.65$ g/mol is the molar mass of a GaAs building block and $N_A = 6.022 \times 10^{23}$ per mol is Avogadro's number. Using the measured density ρ_{GaAs}, a number density of $n_{\text{GaAs}} = 1.96 \times 10^{22}$ cm^{-3} was obtained for the samples, which is about 11% lower than the literature value of 2.20×10^{22} cm^{-3} [6]. The discrepancy between the measured value and the literature value could be an indication of polycrystallinity. A photograph of the samples loaded on the sample holder is

shown in Fig. 3.8.

4.2 Langmuir Probe Measurements

Evaluation of the current-voltage plot obtained from Langmuir probe measurements is a standard technique in plasma physics. A discussion of the physics and the instrumentation is given in several textbooks [9, 26, 50] and more in-depth in reviews [51, 52, 53, 54, 55, 56].

Fig. 4.1 shows the measured current response as a function of the applied voltage for a nitrogen plasma generated by 400 W RF power (13.56 MHz) at (3±1) mTorr working pressure. Measurements were performed before, during, and after implantation, but they yielded essentially the same values for all parameters in the plasma bulk and will not be discussed separately.

The plasma potential is located at the intersection of the two lines in the inset and has a value of 19.5 V with respect to ground. Strictly speaking, this potential is the sum of the plasma potential and the wall potential. The electron and ion currents are balanced at (4.8±2.4) V which is the floating potential. The left line is fitted to the diode-like electron collection which theoretically occurs until the probe potential equals the plasma potential and the right current line is fitted to the electron saturation current for probe potentials above the plasma potential.

The electron temperature may be obtained from the electron component of the probe current [26] by realizing that the electron temperature is the inverse slope in the log(current)-voltage plot between the floating potential and the plasma potential

$$T_e = \frac{\Delta V}{\Delta \ln (I)}. \tag{4.2}$$

An appropriate number of data points was used to calculate an electron temperature of 4.34 eV by least square fitting to the left slope in the inset of Fig. 4.1.

Three different methods were applied to the current-voltage measurements to extract the plasma densities. The first method obtains the plasma ion density from applied voltages much lower than the positive plasma potential. Electrons are repelled by the probe in this configuration. Therefore, only ions are collected. The ion

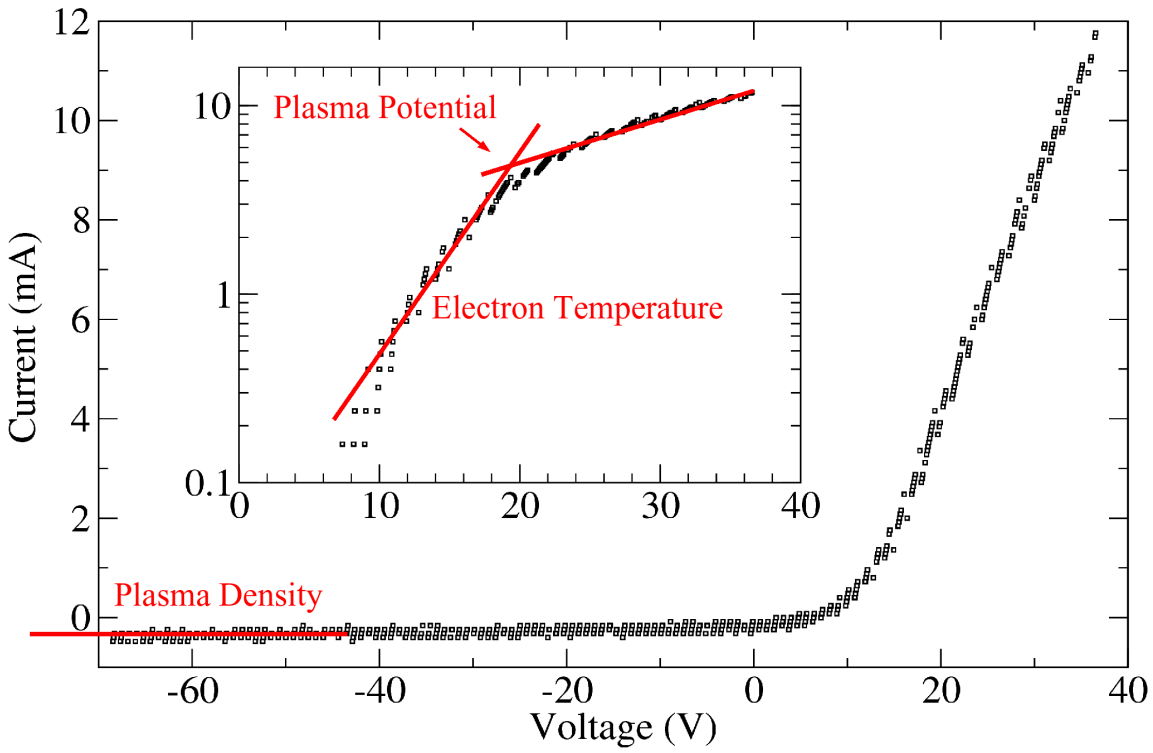

Figure 4.1. A current-voltage curve obtained from Langmuir probe data for a nitrogen plasma generated by 400 W RF (13.56 MHz) power at 3 mTorr pressure. The inset is logarithmic to emphasize the difference in the slopes.

saturation current I_i collected by the negatively biased probe is [26]

$$I \approx -I_i = -0.61 \cdot e n_i u_B A_{\text{probe}}, \tag{4.3}$$

where n_i is the ion density, $u_B = 4,000$ m/s is the Bohm velocity and $A_{\text{probe}} = 5$ mm^2 is the surface area of the probe. Eq. (4.3) was solved for the ion density $n_i = 1.7 \times 10^{17}$ m^{-3} using an average current obtained from all data points for which $V < -60$ V.

The second method follows the orbital-motion-limited (OML) approach [57, 58] which includes effects of the pre-sheath to obtain the ion density n_i. Here, the ion current is given by

$$I_i = e n_i v_i A_{\text{probe}}, \tag{4.4}$$

where the ion velocity v_i is

$$v_i = \sqrt{\frac{-eV}{8m_i}} \tag{4.5}$$

with V as the applied voltage, $e = 1.602 \times 10^{-19}$ C as the elementary charge and m_i as the (effective) ion mass. The value of the ion density was again obtained by least-square fit to all data points for which $V < -60$ V. The OML approach yields $n_i = 6.8 \times 10^{16}$ m^{-3}.

The last method [59] takes data from the electron saturation region where the electron current is dominant. The current at the plasma potential is then given by

$$J_{V_p} = \frac{1}{4} e n_e \langle v_e \rangle, \tag{4.6}$$

where $\langle v_e \rangle = \sqrt{\frac{8kT_e}{\pi m_e}} = 1.4 \times 10^6$ m/s is the average thermal speed of Maxwellian-distributed electrons. The current at the plasma potential was measured as $J_{V_p} = 2.7$ mA. Rearranging eq. (4.6) yields the electron density $n_e = 9.85 \times 10^{15}$ m^{-3}.

4.3 Discussion

Plasma Potential

Lieberman [26] derives the sheath potential at a floating wall V_0 from the condition of equal ion and electron fluxes at the sheath boundary. The plasma (space) potential is approximately the floating wall potential if the effects of the grounded walls are neglected

$$V_0 \approx V_p = \frac{1}{2} T_e \cdot \ln\left(\frac{m_i}{2\pi m_e}\right) \tag{4.7}$$

where $T_e = 4.34$ eV is the electron temperature, $m_i = 26$ u is the effective mass of the ions and m_e is the mass of the electrons. The value $V_p = 19.39$ V obtained from eq. (4.7) under the assumption of a correctly measured electron temperature compares extremely well with the measured value of 19.5 eV within the 10% error due to the setup.

Electron Temperature

The obtained value of $T_e = 4.34$ eV within 10% error agrees very well with Hong Li's measurements[1] [41] on the same setup. She also found that the electrons do not strictly follow a Maxwellian distribution, which adds to the error budget for the electron temperature.

Plasma Densities

The plasma ion and electron densities were obtained by three different methods which diverge by a factor of 10 from the lowest measurement to the highest. The ion densities obtained by the Langmuir probe were higher than the electron density by a factor of approximately 6-10 which was also observed by Tusyewski and Tobin [42] for a lower RF frequency (0.46 MHz). Their ratio is 1.2 at 400 W power and 3 mTorr pressure. They suggest that RF interference causes the overestimation of the ion densities. Our Langmuir probe is poorly shielded against RF which would explain the higher ratio in my study.

The determination of the electron density with this method depends critically on the exact position of the plasma potential, which cannot be determined very precisely with the present setup. The value $n_e = (9.85 \pm 0.99) \times 10^{15}$ m^{-3} is close to the electron density of 1.24×10^{16} m^{-3} reported by Tusyewski and Tobin [42]. The ion density of 1.53×10^{16} m^{-3} in their report is lower than the ones I obtained, but is of the same order. The best agreement between the measured and predicted currents was obtained for a plasma bulk density of $n_0 \approx n_i \approx n_e \approx 1.2 \times 10^{16}$ m^{-3} which agrees with the measurements in Ref [42].

[1] Fig. 4.7 on p. 37 in Ref [41] shows a broad maximum at about 4.3 eV for 400 W. Note that the position of the maximum is not strongly dependent on the pressure, thus the values obtained for 5 mTorr are also valid for the lower pressure of 3 mTorr used in my study.

Chapter 5

Modelling Plasma Ion Implantation

5.1 Introduction to the Lieberman Model

Lieberman derived an analytical alternative to the differential equations of a two-fluid plasma by assuming that the current can be described by the Child-Langmuir law on the one hand and by the current due to a combination of the moving sheath edge and the Bohm current on the other hand. The model is also known as the dynamic sheath model. Lieberman's derivations for the current toward the target and the sheath width for ideal rectangular pulses [60] and trapezoidal pulses [61] compare reasonably well to numerical simulations and measurements [62].

The physical insight and simplicity of an analytical description for a complex system such as the plasma sheath must be paid for by assumptions which specify the boundaries of the description's validity. The analytical Lieberman model for the ion current toward the target is subject to the following conditions:

1. Electric fields are frozen to their initial value during a calculation step. Thus, ion motion and the sheath positions are treated quasi-statically.

2. A fully expanded quasi-static ion matrix sheath forms instantaneously and the current can be described by a (quasi-static) Child-Langmuir law [30] during the entire implantation.

3. Pre-sheath and the plasma bulk supply the Bohm current and the plasma ion density at all times which are treated as boundary conditions. Furthermore, the ion reservoir is infinite and refilling happens instantaneously.

4. Electrons respond instantaneously to the applied fields. Lieberman [60] refers to those electrons as 'inertialess'.

5. Ions arrive at the target instantaneously.

6. Uniform plasma density in the region of implantation.

7. Collisionless ion flow.

8. The sheath edge is abrupt which applies if the Debye length is much smaller than the initial sheath width.

9. Ions are mono-atomic and singly charged. Moreover, multiple ion species in the plasma produce a common sheath edge, i.e. they can be treated by an effective mass.

10. The geometry is planar and one dimensional.

11. Ion density and initial sheath width at the beginning of each applied voltage pulse are the same.

12. The measured potential is the potential at the sample surface.

The first four assumptions as well as assumptions 7 and 8 were briefly discussed in the paper describing the model [60]. I added the other assumptions due to their relevance for an accurate description of a real PII process. There is no review of their validity in the literature. My discussion may be found in Appendix C.1.

There are several numerical simulations constrained by far less assumptions [63, 64, 65], but their execution is time consuming. Moreover, the extra effort is futile for most PII applications where other sources of error outweighs the accuracy of current or dose predictions. The Lieberman model has been proven a fair approximation for PII under laboratory conditions [62].

5.2 Implementation of the Model

The implementation of the model follows a report by En et al. [62] with extensions for multiple ion species [66, 67], plasma enhancement [37] and the prediction of currents before and after implantation [68]. The name of the software discussed here is p2i. It is written in ANSI C and a refinement of the software previously discussed by JT Steenkamp [31]. My work is the first attempt to predict the sheath, current and fluence within error boundaries.

5.2.1 Current and Sheath

The fragile equilibrium of ions in the sheath must be sustained by a constant flow of ions into the sheath region. The new ions are supplied by the Bohm current

$$J_B = enu_B \tag{5.1}$$

and also by the moving sheath edge

$$J_s = en\frac{ds}{dt}, \tag{5.2}$$

which uncovers new ions to be accelerated until the space charge of the ions in the sheath cancels the applied potential at the target. The expression becomes negative for decreasing potential, thus screening some of the ions from the Bohm current by virtue of a shrinking sheath width. The sign of the moving sheath edge for all phases is shown in Table 5.1.

The total current toward the target at all times can hence be written

$$J = en\left(V,t\right)\left(\frac{ds\left(V,t\right)}{dt} + u_B\right), \tag{5.3}$$

where e is the elementary charge, ds/dt is the velocity of the sheath edge, u_B is the (effective) Bohm velocity and $n\left(V,t\right)$ is the momentary plasma density tabulated in Table 5.1. This density is reduced when a pre-sheath exists and is enhanced linearly with the voltage during PII

$$n\left(V,t\right) = \begin{cases} n_0\left[1 + a \cdot V\left(t\right)\right] & \text{during PII} \\ 0.61 \cdot n_0 & \text{else} \end{cases}, \tag{5.4}$$

Table 5.1. Phases during plasma ion implantation and their implementation in the p2i software. CL denotes the Child-Langmuir sheath, a is the coefficient of the plasma enhancement and n_0 is the plasma bulk density.

Region	1	2	3	4	5
Voltage Shape	_____	/	—	\	_____
Sheath Type	Quiescent	Matrix+CL	CL	CL	Quiescent
Pre-Sheath	large	small	small	small	large
Density	$0.61n_0$	$(1+aV)n_0$	$(1+aV)n_0$	$(1+aV)n_0$	$0.61n_0$
Sheath Velocity	ds/dt=0	ds/dt>0	ds/dt=0	ds/dt<0	ds/dt=0

where a is a constant, V is the voltage at the sample surface and the factor 0.61 was derived in Section 2.2.1.

At the same time, it is assumed that the current toward the target at all times can be described by the Child-Langmuir law [30]

$$J_{CL} = \frac{4}{9}\varepsilon_0\sqrt{\frac{2e}{m_i}}\cdot\frac{V^{3/2}}{s^2}. \tag{5.5}$$

Equating the currents in eqs. (5.3) and (5.5) gives an inhomogeneous non-linear differential equation for the sheath width s(t)

$$\frac{d}{dt}s(V,t) - \frac{4}{9}\frac{\varepsilon_0}{e\cdot n\,(V,t)}\sqrt{\frac{2e}{m_i}}V(t)^{3/2}\left(\frac{1}{s(V,t)^2}\right) = -u_B. \tag{5.6}$$

The software solves this differential equation for each of the time steps using a 4th order Runge-Kutta algorithm. The resulting value for the sheath width is then plugged back into eq. (5.5) to obtain the current density at time t.

In the steady-state $ds/dt = 0$ and eq. (5.6) becomes

$$s_0 = \left(\frac{4}{9}\right)^{1/2}\left(\frac{\varepsilon_0}{enu_B}\right)^{1/2}\left(\frac{2eV_0^3}{m_i}\right)^{1/4}. \tag{5.7}$$

Substitution of the Bohm velocity u_B, introducing the Debye length λ_D and sorting yields

$$s_0 = \frac{\sqrt{2}}{3}\frac{1}{\sqrt{b}}\lambda_D\left(\frac{eV}{kT_e}\right)^{3/4}, \tag{5.8}$$

where b is the modifier of the plasma bulk density. Before and after implantation $b = 0.61$, $V = 19.5$ V and $kT_e = 4.34$ eV. The sheath width from eq. (5.8) is then $s_0 \approx 3 \cdot \lambda_D$ which compares reasonably well to the screening of the potential in Fig. 2.3 a). The differential equation in eq. (5.6) can therefore be used for times before and after high-voltage implantation and eq. (5.8) is a reasonable starting value for the quiescent sheath width.

5.2.2 Fluence and Energy Distribution

Integration by Simpson's rule over the current from the pulse's beginning to its end yields the fluence which is defined here as the number of (molecular) ions in the sheath that are accelerated toward a unit area. Upon impact on the area, the molecular ions break into mono-atomic ions. If their energy and trajectory is such that they are stopped within the target, those ions will contribute to the dose which has units of ions per unit volume. The software calculates the energy distribution of the ions from the applied potential under the assumption that all ions are singly charged and accelerated by the full potential at any time step, i.e. a histogram of the voltage is calculated. It is assumed that the contributions of different species to the fluence is in the same ratio than the population of those species in the plasma. This is strictly valid only for short pulse durations [67]. Two cases are considered in the output, the energy distribution of the fluence in the plasma as well as the distribution of the mono-atomic daughter ions formed at the instant of the impact. The calculation of the dose will be discussed in Chapter 7.

5.2.3 Error Boundaries

The error boundaries in the output of the sheath width and the plasma ion current are calculated from three sources: the errors of the measured electron temperature and plasma bulk density as well as from the quantization error of the oscilloscope. The error in the first two variables is estimated as 10% [42], the latter error is typically 1% of the pulse plateau. The relative quantization error is thus very large

at the beginning and end of the pulse. All three errors are used to calculate the set of minimal and maximal variables which are fed to the same algorithms that calculate the (average) values for sheath, current and fluence.

5.2.4 Measured Sheath, Current and Fluence

The p2i software also outputs the measured current density and the sheath width calculated from the measured current, both as a function of time. The raw output of the Pearson coil is smoothed and divided by the sample area after the secondary electron current component is subtracted. The sheath width is calculated from eq. (5.5) under the assumption that the current can be described by the Child-Langmuir law at all times. This method can only be used during high-voltage implantation when the measured current is exclusively due to ions. Finally, the measured fluence was obtained by integration over the current density from the start of the pulse to its end with the same Simpson's rule algorithm used to obtain the predicted fluence.

The henceforth called 'measured' values are subject to a correct estimation of the electrode area and the secondary electron emission and thus not raw data. The electrode area was measured, but the entire area is not necessarily immersed in plasma. In fact, about a third of the rod supporting the sample holder is hidden in a port where the ionization from the ICP coil should be less than in the chamber. Moreover, an extended sample adds to the effective surface area and if sample and sample holder are made from different materials, both secondary electron emission coefficients must be included. The sample holder area and secondary electron coefficient in the calculations do not include those effects and should thus be understood as effective areas and coefficients.

5.2.5 Calculation Input

Predictions using the Lieberman model require at least the electron temperature, the plasma density and the time-dependent electrode potential as input. The first two are typically obtained from Langmuir probe measurements and the latter is either

Table 5.2. Input parameters used in the calculation of the ion current, sheath width and fluence. The last column states how the value was obtained.

Parameter	Value	Obtained via
Electron Temperature T_e	(4.34±4.3) eV	Langmuir probe
Plasma Density n_0	$(1.20\pm0.12)\times10^{16}$ m^{-3}	Pearson probe
Density Enhancement Factor a	5.5×10^{-4} per V	Fitting
Ion Populations	13.2% N^+, 85.7% N_2^+, 1.1% N_3^+,	Ref [43]
Plasma Potential	19.5 V	Langmuir probe
Electrode Area	42.0 cm^2	Measurement
Secondary Electrons α^*	1.0 at 10 kV	Fitting
Electrode Potential	see inset of Fig. 5.4, 5.3 or 5.5	HV probe

measured or approximated by the analytic formula [61] for trapezoidal voltage pulses.

The input parameters to all predictions shown in this work are given in Table 5.2. The density enhancement factor and the secondary electron emission coefficient were chosen to fit a large number of electrode potentials in both modes. The predicted and measured current densities were compared for their initial Bohm currents, peak heights, currents at the plateau and decay characteristics of the peak to the plateau as well as from the plateau to the Bohm current after the pulse. The predictions depend strongly on a correct measurement of the ion bulk density and electron temperature which can be seen in Fig. 5.1 and Fig. 5.2, respectively. Variations in those parameters affect the peak height and the decay behaviour of the ion current and hence the fluence. Both increase the peak height with lower values and increase the current in the fall time of the voltage.

5.3 Sheath Prediction

The predicted sheaths and measured sheaths are shown in Fig. 5.3, Fig. 5.4 and Fig. 5.5. All measured sheaths are reasonably close to the predicted error boundaries. The maximum sheath widths are consistently lower than the sheath widths expected

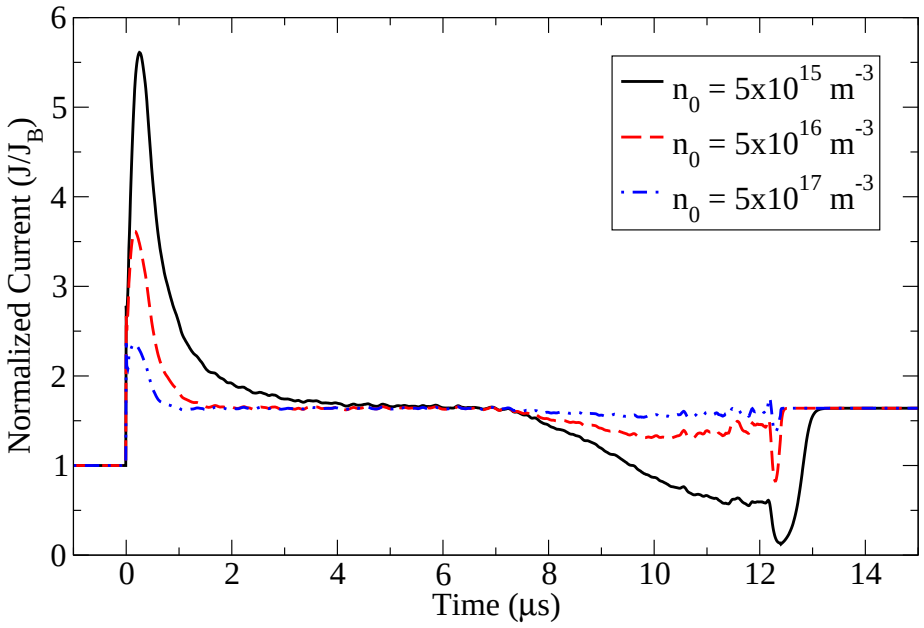

Figure 5.1. Change of the ion current prediction for various ion bulk densities. The calculation uses the voltage waveform shown in the inset of Fig. 5.3. The electron temperature was set to 4.34 eV and ion density enhancement was turned off. It was assumed that the pre-sheath does not form instantly after the end of the voltage pulse.

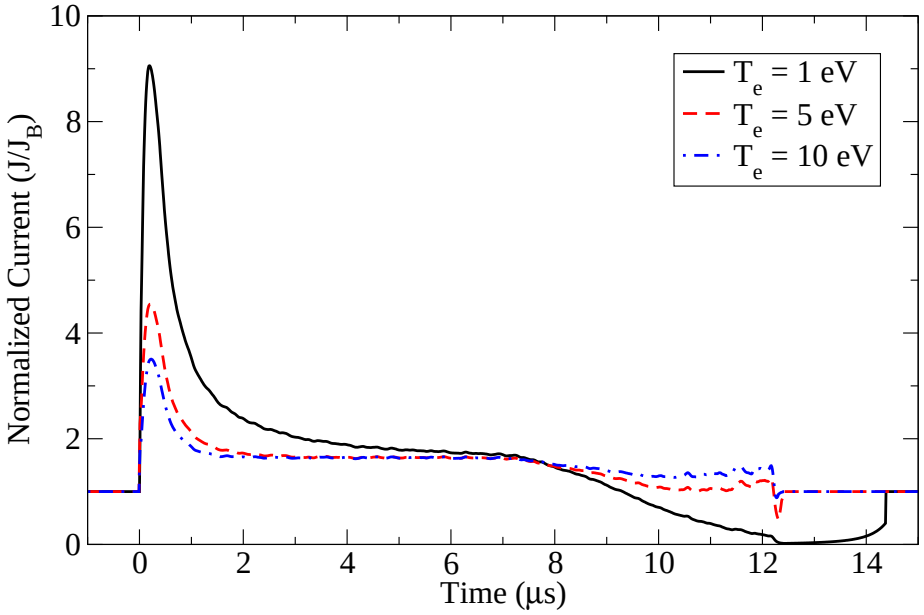

Figure 5.2. Change of the ion current prediction for various electron temperatures. The calculation uses the voltage waveform shown in the inset of Fig. 5.3. The bulk ion density was set to 1.2×10^{16} m^{-3} and ion density enhancement was turned off. It was assumed that the pre-sheath forms instantly after the collapse of the high-voltage sheath.

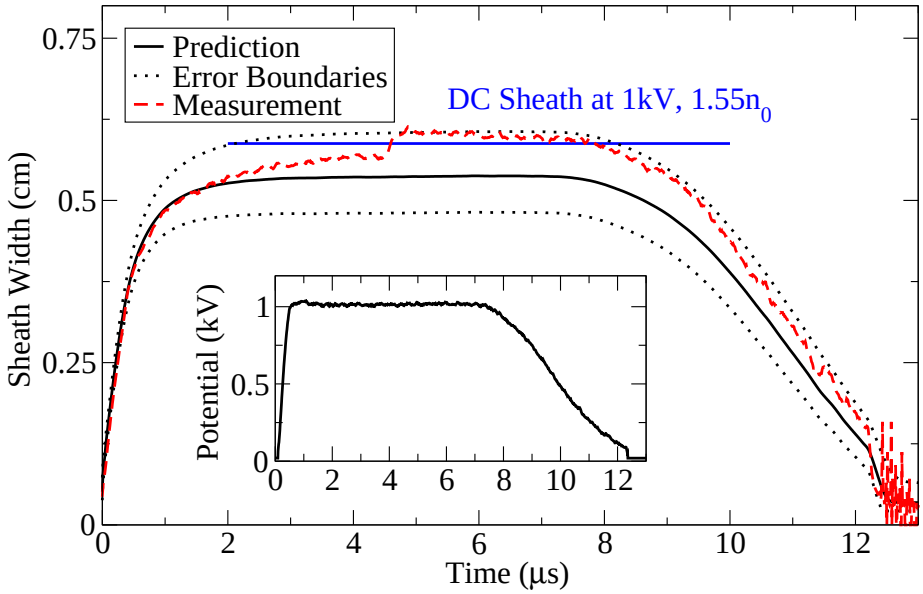

Figure 5.3. Comparison between the measured sheath and the sheath predicted by the p2i software. The inset shows the electrode potential used in the calculation. This is an example for a typical -1 kV voltage pulse generated in the 'Marx Mode'. The horizontal blue line is the expected sheath width for a very long ideal pulse (DC solution). The kink at 5 μs is most likely due to a malfunction in the Marx stage.

for a long pulse at the enhanced plasma density and the difference grows with higher plateau voltages and less ideal pulse shapes. This is a consequence of the plasma enhancement factor and the dependence of the sheath width on its history. The predictions agree very well with the DC sheath width if the plasma enhancement is turned off and the plasma conditions allow a steady-state sheath width for the duration of the pulse.

The Child-Langmuir law is not valid at the beginning of the voltage pulse, where the current is due to the extraction of ions from the Matrix sheath. This happens fast, i.e. within the first few steps of the calculation, and can thus be neglected. Sheaths predicted by the Lieberman model are generally lower than those predicted by numerical simulations [10, 68]. Those simulations predict a steeper rise and fall slope, but agree well in terms of the sheath collapse time. The measured sheath width can only be calculated until the end of the high-voltage pulse, when currents due to electrons become dominant. This will be discussed in the next section.

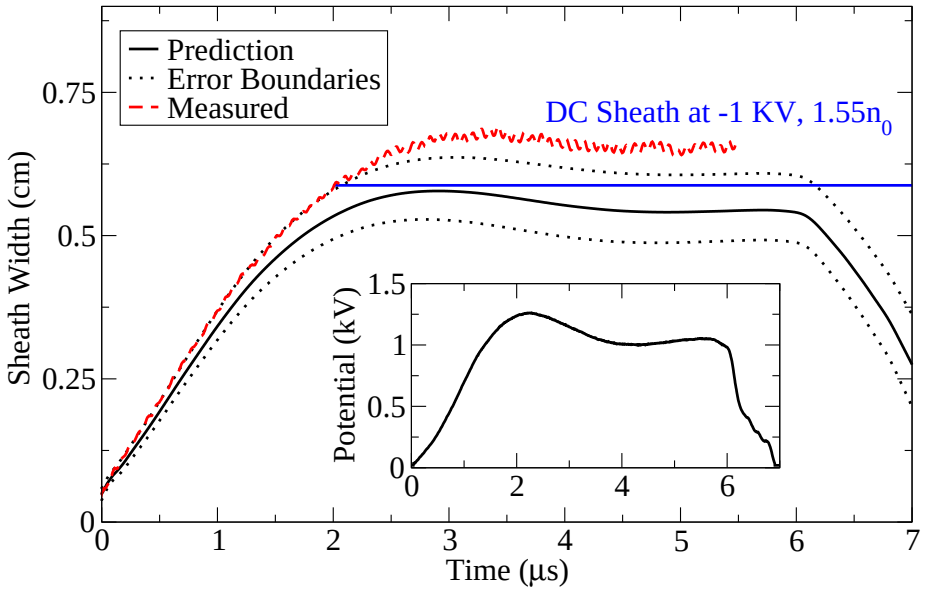

Figure 5.4. Comparison between the measured sheath and the sheath predicted by the p2i software. The inset shows the electrode potential used in the calculation. This is an example for a typical -1 kV voltage pulse generated in the 'Transformer Mode'. The horizontal blue line is the expected sheath width for a very long ideal pulse (DC solution).

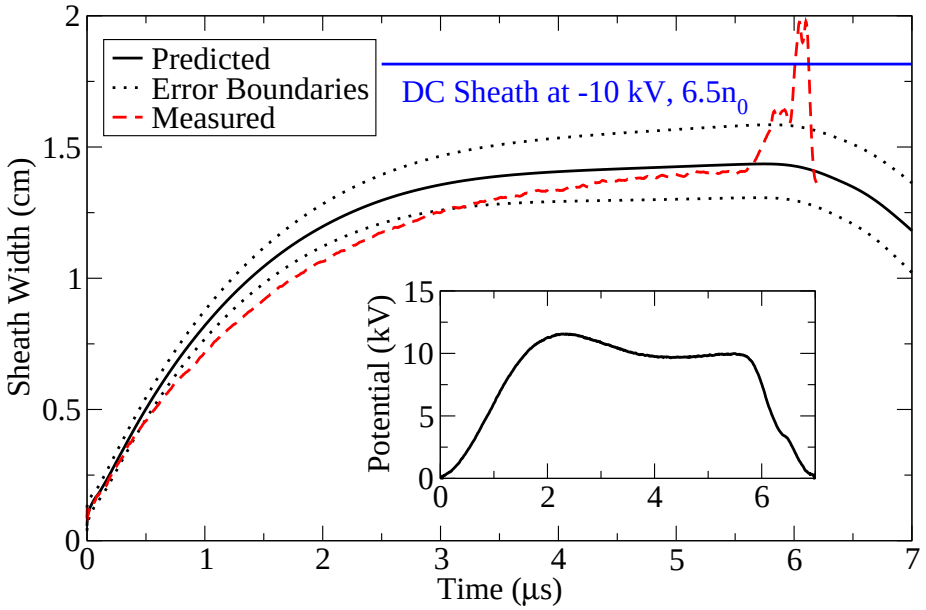

Figure 5.5. Comparison between the measured sheath and the sheath predicted by the p2i software. The inset shows the electrode potential used in the calculation. This is an example for a typical -10 kV voltage pulse generated in the 'Transformer Mode'. The horizontal blue line is the expected sheath width for a very long ideal pulse (DC solution) at the enhanced plasma density. The pulse is too short to reach the maximal sheath width under conditions in the plasma.

5.4 Plasma Current Prediction

The predicted and measured current densities are compared in Fig. 5.6, Fig. 5.7 and Fig. 5.8. The -1 kV pulse in the 'Marx Mode' (MM) and the -10 kV pulse in the 'Transformer Mode' (TM) are predicted very well within the error boundaries. The plateaus of predicted currents for the -1 kV pulses are at the level of the Bohm current for the enhanced density. This is expected from the left hand side of eq. (2.16) when the sheath width does not change. The predicted current of the -10 kV pulse is higher than the Bohm current which can be explained from the underestimation of the sheath width in most of Fig. 5.5.

Limitations of the Model

Two features in the prediction of the upper error boundary catch the eye: secondary peaks at the beginning and the end of Fig. 5.6 and Fig. 5.8. The spike at the beginning is the result of an underestimation of the minimal Matrix sheath width and a relative quantization error of the order of 50 to 100% for the first steps. The peaks at the end are caused by the minimal sheath width which collapses first and is close to the small pre-implantation steady-state value while the maximum voltage is still considerably high. The current then surpasses the level of the Bohm current for the enhanced plasma density. The software is still in development and those glitches were deliberately not edited to show exactly the output a user of the software would produce.

The oscillations with high amplitudes at the end of the measured current are most likely due to sheath depletion. The absence of ions in the former sheath region causes electrons to pour into the void and get lost to the electrode in large numbers. The current decays to the level of the initial current after 2 to 3 μs. The sign of the current should be opposite of the ion current, but the current experimental setup is not able to detect this.

Anomaly of the -1 kV TM Pulse

The measured current in Fig. 5.7 violates the assumption of plasma density enhancement as well as the assumption that the pre-sheath before implantation has a density significantly different from the plasma bulk. However, the effects of plasma density enhancement are clearly visible in the current plot for the 'Marx Mode' at the same peak voltage, see Fig. 5.6. A hypothetical threshold for the plasma density enhancement must therefore be dependent on the voltage as well as the shape of the applied voltage waveform. The assumption that the Child-Langmuir sheath eats into the pre-sheath could also be invalid. The factor of 0.61 due to the difference between bulk and the edge of the pre-sheath can be absorbed into the plasma enhancement factor without affecting the fit. It is also possible that the secondary electron emission rather than the plasma enhancement factor has to include a threshold. The physics behind the current density caused by the -1 kV pulse in the 'Transformer Mode' must be subject to further research.

Concluding Remarks

The deficits in the prediction of the ion current with the Lieberman model, especially the height of the first peak, have also been reported by other researchers [62, 68, 69]. The plasma current can be measured directly by means of a Faraday cup which is currently being added to our experimental setup. Faraday cup measurements make redundant the inclusion of the secondary electron coefficient, but cannot resolve the uncertainties concerning the true area of the electrode. Nonetheless, the direct measurement of the ion current will help to increase the accuracy of the predictions further and could also supply insight to the puzzle of the measured current for the -1 kV pulse in the 'Transformer Mode'.

5.5 Fluence Prediction

The performance of the experimental system for a wide range of implantation durations is depicted in Fig. 5.9. Table 5.3 contains the fluences obtained by integrating

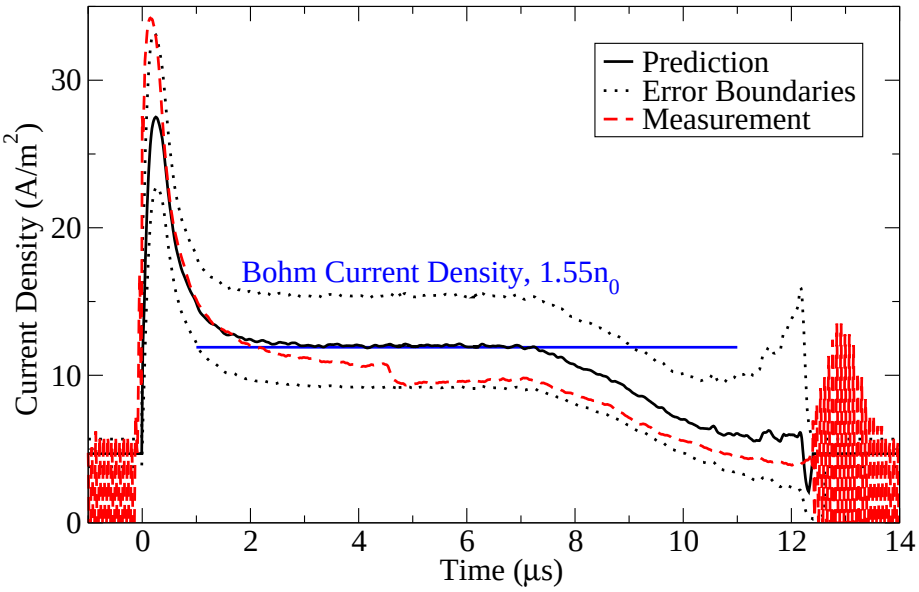

Figure 5.6. Comparison between the measured current and the current predicted by the p2i software for the voltage pulse shown in the inset of Fig. 5.3. The horizontal blue line show the expected Bohm current for the given conditions in the plasma. The kink at 5 μs is most likely due to a malfunction in the Marx stage.

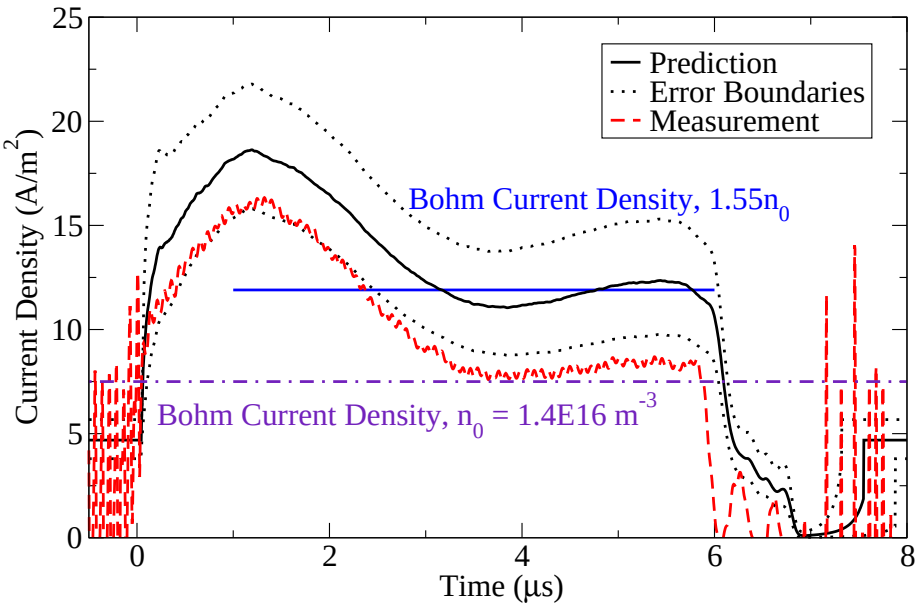

Figure 5.7. Comparison between the measured current and the current predicted by the p2i software for the voltage pulse shown in the inset of Fig. 5.4. The horizontal blue line show the expected Bohm current for the given conditions in the plasma. The purple dashed line shows that the plateau is at the same level as the initial Bohm Current density.

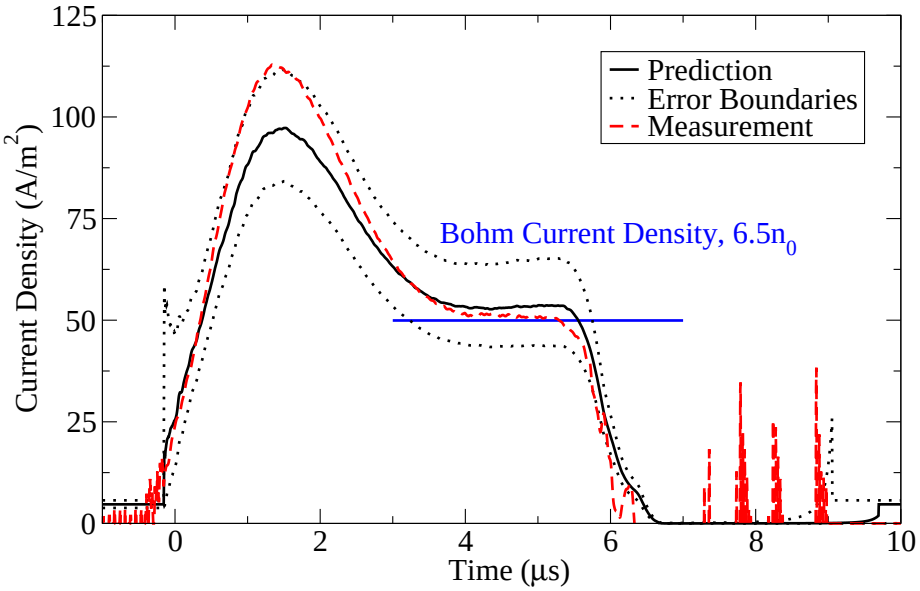

Figure 5.8. Comparison between the measured current and the current predicted by the p2i software for the voltage pulse shown in the inset of Fig. 5.5. The horizontal blue line show the expected Bohm current for the given conditions in the plasma.

the currents shown in the previous section. The first and the last fluences agree very well to the measured fluences within the error prediction. The second fluence (Fig. 5.7) is too low because of the reasons discussed in the last section.

The predicted fluences scale according to

$$F \propto n_0^p V_0^{1/2}, \tag{5.9}$$

where n_0 is the plasma bulk density, V_0 is the voltage at the plateau of the pulse and p depends on the plasma enhancement factor. The exponent is $p = 1.27 \approx 5/4$ for no plasma enhancement and $p = 1.14$ for an enhancement of $a = 5.5 \times 10^{-4}$ per volt. In any case, the exponents are lower than the value $p = 3/2$ which was reported by Tian and Chu [70]. They derived the exponent for a perfectly rectangular pulse, whereas all of our pulses were approximately trapezoidal. Hence, the exponent could also depend on the shape of the applied voltage form. The scaling with the ion density is important for the optimization of plasma ion implantation, but scarcely reported in the literature. Further research with other common voltage shapes for PII processing and a greater set of (enhanced) densities is necessary to draw any conclusions.

Table 5.3. Fluences per pulse for both modes and -1 kV as well as -10 kV plateau voltages.

Current Profile	Measured (ions/cm^2)	Predicted (ions/cm^2)
Fig. 5.6	7.7×10^{10}	$(8.5^{+2.8}_{-2.1})\times10^{10}$
Fig. 5.7	3.9×10^{10}	$(5.3^{+1.2}_{-1.0})\times10^{10}$
Fig. 5.8	25.2×10^{10}	$(24.6^{+4.8}_{-4.1})\times10^{10}$

Fluence Measurements

Whether dose[1] (ions in the solid) or fluence (ions in the plasma) is the more meaningful variable to measure depends on the focus of one's research. The dose is routinely measured ex-situ by Rutherford Backscattering (RBS) or Nuclear Reaction Analysis (NRA). The first technique is non-destructive and uses the scattering of ion beams in the target material to obtain the composition. NRA makes use of ionization radiation given off by excited nuclei to probe the material composition. In-situ measurements of the fluence are preferable, but more difficult to realize due to the high voltage biasing of the target in close proximity and the immersion of the apparatus in plasma. Measurements of the fluence with a Faraday cup have been successfully demonstrated [71] and will soon be available at our experimental setup. Tian and Chu [47] measured the increase in temperature during implantation from which they calculated the fluence. A yet unexplored method is the in-situ measurement of the mass increase after implantation with a quartz scale. However, screening from the plasma and the high-voltage at the target is an engineering challenge.

5.6 Ion Energy Distribution

Knowing the ion energy distribution is crucial for the prediction of the distribution of the dose within the target. Fig. 5.10 shows the distribution of kinetic energies of

[1]The the dose (ions per volume) should be distinguished from fluence (ions per area) because molecular ions break into daughter ions at the target's surface and not every ion becomes implanted. Most authors do not make this distinction.

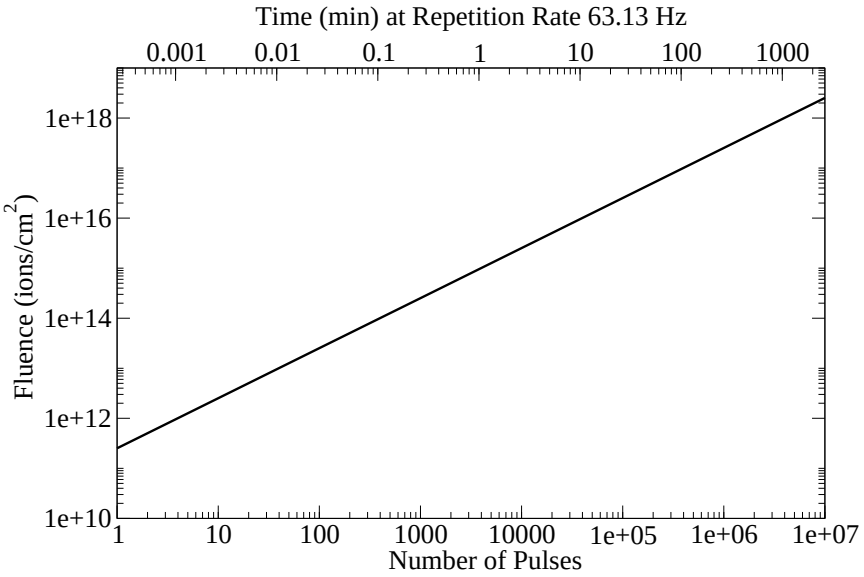

Figure 5.9. Performance of the experimental setup for -10 kV implantation in the 'Transformer Mode' with the plasma conditions in Table 5.2.

the nitrogen ions traveling in the plasma and the distribution when the molecular ions impact on the surface and break into mono-atomic components. It is assumed that the initial kinetic energy is distributed among the daughter ions according to

$$\mathrm{KE}_d = \sum_d \left\{ \frac{m_d}{m_{\mathrm{total}}} \cdot \mathrm{KE}_{\mathrm{ini}} \right\}, \tag{5.10}$$

where KE $_d$ is the kinetic energy of the daughter ion, m_d is its mass, m_{total} is the mass of the precursor molecule and KE_{ini} is the initial kinetic energy of the molecule. The energy distribution upon impact is shifted toward lower energies since nitrogen is mostly diatomic and hence every N_2 breaks into two ions possessing half the initial energy.

Discussion of the Plots

The distribution upon impact is plotted relative to the fluence in the plasma and thus does not add up to 100%. In the case of a purely diatomic plasma, the distribution upon impact would be 200% of the initial fluence. For the nitrogen populations given in Table 5.2, the distribution adds up to 187.9% which would be the difference between fluence and dose if all ions were implanted. The kinetic energy of the

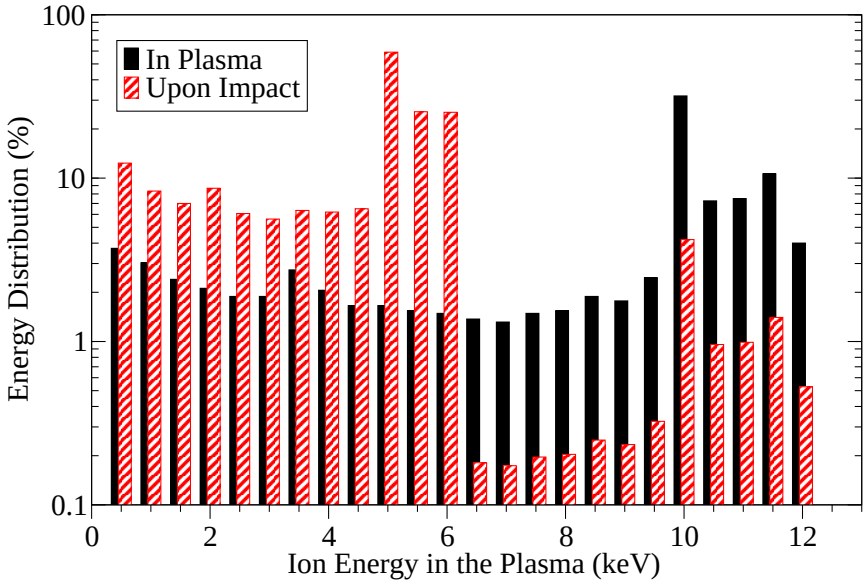

Figure 5.10. Comparison between the distributions of molecular ion energies in the plasma (solid black) and the distribution of daughter ions upon impact with the target surface (red stripes). Calculation output of the p2i software for the -10 kV pulse shown in the inset of Fig. 5.5.

molecular ions, which is proportional to the penetration depth, can thus be traded for an increase in dose by a smart choice of the precursor gas. Fig. 5.11 shows the mono-atomic ion energy distribution upon impact for the three ion species in the plasma. The mono-atomic nitrogen ions have the highest energies and will thus penetrate deepest into the material. The diatomic ions are the biggest contribution with a peak around 5 keV. Tri-atomic ions do not add much to the distribution even though they break into 3 pieces. PII with a -10 kV trapezoidal voltage pulse (cf. Fig. 5.5) thus results in a most probable implantation ion energy of only 5 keV and even worse, a broad bi-modal ion distribution as seen best in Fig. 5.10. The desired characteristic for my work would be a mono-energetic ion energy distribution at the impact which is at the highest possible kinetic energy. The ion depth distributions in the GaAs target resulting from various scenarios for the ion energy distribution will be discussed in Section 7.4.

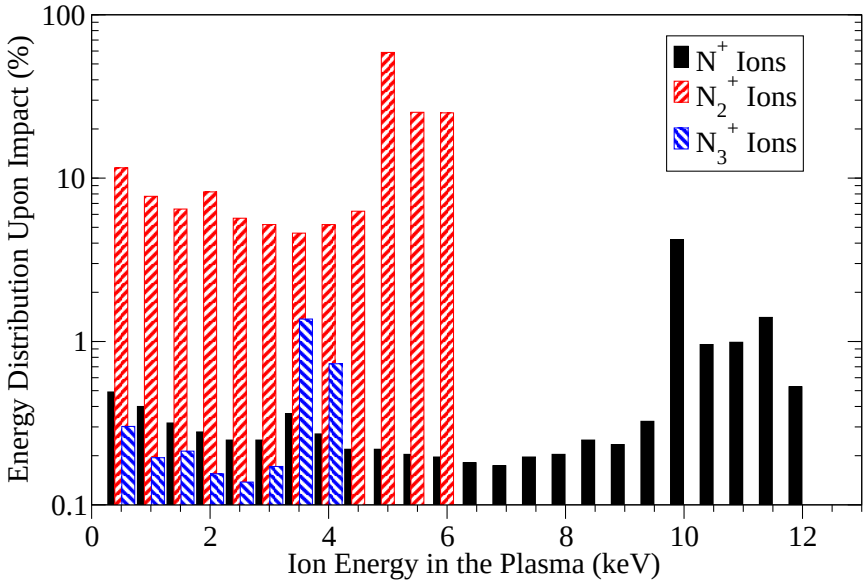

Figure 5.11. Distribution of ion energies upon impact on the target's surface by ion specie. Calculation output of the p2i software for the -10 kV pulse shown in the inset of Fig. 5.5.

Limitations of the Model

The method of calculation does not include fall time implantation, time-of-flight effects or the change of the potential within the plasma sheath. All of these add additional low energy components to the prediction, the latter two even in the case of ideal, rectangular pulses. Time-of-flight effects had only marginal impact on the predicted current when implemented after Barrosso et al. [69] or Steenkamp [31]. Thus, it can be neglected for the plasma conditions and pulse lengths discussed in this report. Linder et al. [67] discuss the time-of-flight effects on the energy distribution in great detail. Ion energy distributions in the Lieberman model were also discussed by Stewart and Lieberman [61] as well as by Tian et al. [72]. The measurement of the ion energy distribution using a Faraday cup was reported by Mändel et al. [73] and Kellerman et al. [36]. The change of the spatial plasma potential in the sheath should account for the biggest contribution to the error in the output of the present prediction. The modelling of the ion energy distribution is complex, but I am confident that the next version of the p2i software will include an improved model for the energy distribution.

Chapter 6

The GaAsN Alloy

The importance of GaAsN originates from the possibility of engineering the band gap and also matching its lattice to silicon. Reviews of the materials properties were published by Vurgaftman et al. [7, 74] and Toivonen [75].

6.1 History

Nitrogen implantation into gallium Arsenide (GaAs) wafers for the production of gallium nitride (GaN) or the GaAsN alloy is not a widely used production method. The following brief survey is the first review of the history of a technique which existed for 35 years after all.

Gallium Arsenide (GaAs) was first synthesized and described by Goldschmidt in 1929 [76] and became a very popular semiconductor in the 1950's. Kachare et al. [77] were the first to implant N into GaAs as early as 1973, but the interest in the alloy dwindled in the next two decades. This changed in 1992 after Weyers, Sato, and Ando [78] found from photoluminescence spectroscopy that alloying GaAs with small amounts of nitrogen results in a significant red shift of the observed emission. This feature caught the attention of many groups due to the technological importance of near infra-red (NIR) emission for telecommunication applications. The alloy GaAsN gained the attention of the ion (beam) community again in 1999 and 2000 with reports by Shima et al. [79] and Shan et al. [80]. The latter group published further papers on the aspect of the fabrication by the ion beam technique [81, 82, 83, 84]. Ion beam synthesis synthesis is now explored by various groups, mostly in Europe [85, 86, 87, 88, 89] and North America [90, 91, 92]. The

synthesis of the alloy by Plasma Ion Implantation (PII) is yet to be demonstrated and my contribution to the proceedings of the 9th International Workshop on Plasma Based Ion Implantation and Deposition (PBIID) [93, 94] and this document are the first feasibility studies.

The history of the synthesis of GaN by ion implantation into GaAs is much shorter and will be added for completeness since it may occur during the synthesis of the GaAsN alloy due to phase separation. In 1995, Lin et al. [95] reported the first ion beam synthesis of GaN. Ho et al. [96] reported the synthesis of GaN by PII in 2001. Lo et al. [97] did a follow-up study on the same experimental setup in 2004 which is the latest report of GaN synthesis by PII.

6.2 Structure

An introduction to the structure of crystals is given in Kittel [3] and Kasap [98]. At atmospheric pressures and temperatures, gallium arsenide (GaAs) has a Zincblende crystal structure and gallium nitride (GaN) exists in a Wurtzite crystal structure. Possible unit cells for both crystal structures are opposed in Fig. 6.1. The GaAs crystal is composed of gallium (Ga) atoms in face-centered cubic (FCC) formation as well as arsenic atoms also in FCC formation, but offset by 1/4 of a unit cube length in any direction. The length of the unit cube is also known as the lattice parameter and has the value $a = 5.65$ Å for GaAs [7]. The crystal structure of GaN has trigonal (also hexagonal or rhombohedral) symmetry, i.e. atoms in one plane group in equilateral triangles with spacing of the lattice parameter a and atoms in the plane perpendicular to the first one have the distance of a second lattice parameter c. This structure is then layered. The smallest unit cell in this trigonal crystal structure is the parallelepiped which is forms by the yellow atoms in Fig. 6.1. The atom within the parallelepiped belongs to a different layer. Both constituents of GaN have the trigonal structure described above, but with an offset parallel to the lattice parameter c. The lattice parameters of GaN are $a = 3.19$ Å and $c = 5.19$ Å [74]. Dilute nitrogen ion implantation into the GaAs host matrix

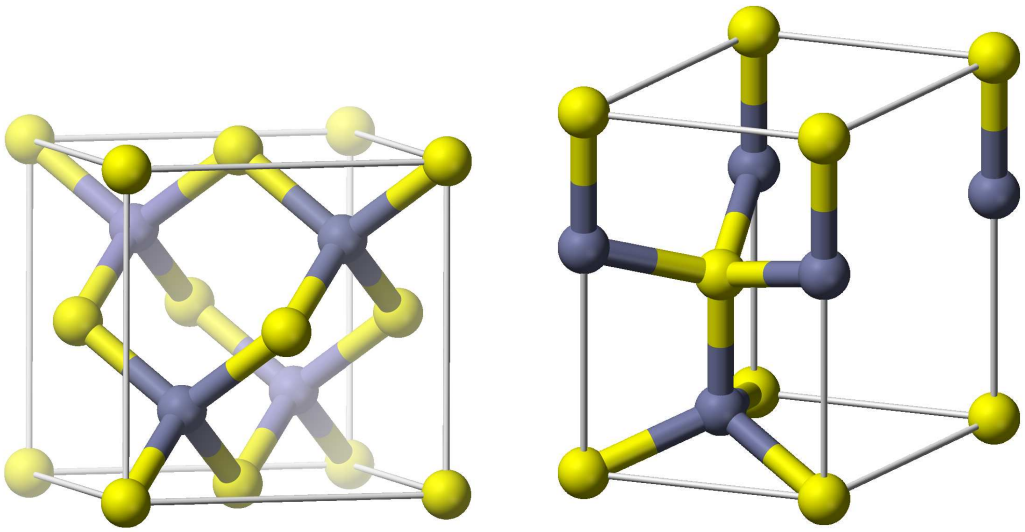

Figure 6.1. Three dimensional illustration of the Zincblende (left) and Wurtzite (right) crystal structures. The graphics are copyright-free available from wikipedia.org.

preserves the Zincblende structure as the non-nitride components are unlikely to form the other crystal structure under the conditions in plasma ion implantation [7].

Defects due to Ion Implantation

Fig. 6.2 shows the (Zincblende) structure of GaAsN as seen from one of the unit cube's faces. Also shown are common defects due to ion implantation: interstitial nitrogen, gallium and arsenic vacancies in the lattice and the distortion they cause to the lattice. Zhang and Wei [99] showed that the molecular N-N interstitial has relatively low formation energy and that it forms an undesired mid gap electron state. It is also common that gas filled voids form upon ion implantation with gas ions. However, annealing decreases the concentration of N-N defects [75] and also fosters the creation of GaN bonds [96]. Concentrations of more than approximately x = 6% in thick layers of the $GaAs_{1-x}N_x$ alloy cannot be synthesized with sufficient quality even if all disorder could be avoided since the differences in the size of arsenic and its replacement, nitrogen, produce strain which induces cracks in the material. The immense difference in size of nitrogen and the other constituents may be seen

in Fig. 6.2. Nonetheless, a concentration of x = 14.8% was reported for a thin layer[1] [103]. Phase separation into GaAs and GaN occurs with most methods for the synthesis of GaAsN alloys when using high nitrogen concentrations [7]. Ho et al. [96] reported such a case for high dose nitrogen plasma ion implantation and subsequent annealing.

Characteristic Size

The average space occupied by a single GaAs building block in the lattice is about

$$V_{\mathrm{GaAs}} = n_{\mathrm{GaAs}}^{-1} = 5.1 \times 10^{-23}\ \mathrm{cm}^3 = (0.37\ \mathrm{nm})^3\,, \tag{6.1}$$

where n_{GaAs} is the measured atomic density of the GaAs samples used in this study. Thus a cube of side length 3.7 nm contains 1000 GaAs formula units and 1% N in GaAs means that 10 nitrogen atoms are distributed somewhere within this cube. For such low nitrogen concentrations, this is approximately equal to the atomic percentage defined by

$$\rho_N\% = \frac{\#\ \mathrm{N\ atoms}}{\#\ (\mathrm{N{+}GaAs})\,\mathrm{atoms}}. \tag{6.2}$$

The high number of molecules also makes it meaningful to discuss the electronic properties and their changes on a 4 nm scale.

6.3 Electronic Properties

A result of the different crystal structures of GaAs and GaN is large differences in various physical properties. The lattice parameter a of GaAs is almost twice as large as the one of GaN. The bonds and hence the band structure must therefore be very different. Indeed, the direct band gap of GaAs is 1.42 eV at 300 K (1.52 eV near 0 K) [7] as opposed to GaN's direct band gap of 3.43 eV at 300 K (3.51 eV near 0 K) [74]. The bonds between gallium and nitrogen as well as between gallium

[1] Foxon et al. [100] report a concentration of "approximately 20%". This reference was not used due to the vagueness of the concentration. A report by Bandic et al. [101] shows graph with a ∼25% concentration, but the reference [102] to the measurement of the concentration in the second report could not be found.

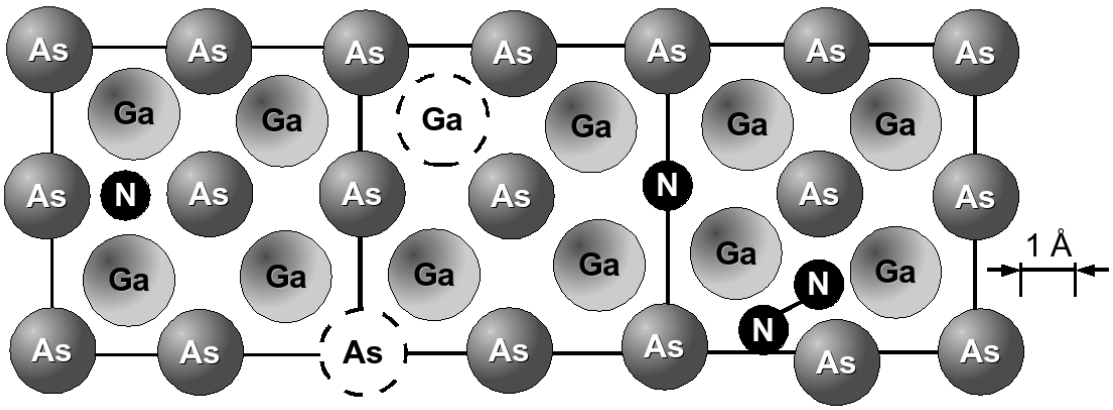

Figure 6.2. The structure of GaAsN and its defects (view along the normal to a unit cube face). The leftmost square contains an interstitial N and an As vacancy (dashed circle) in the right corner. The second square shows a Ga vacancy (dashed circle) and a N replacing As which is desired in this study, but also distorts the lattice. Interstitial N-N is depicted in the rightmost square. The atomic radii [3] and the lattice parameter are drawn to scale.

and arsenic are very different in their properties. The covalent bonding radius of 0.68 Å for nitrogen is much smaller than that of 1.2 Å for arsenic. Nitrogen thus strongly attracts electrons. More specifically, its electronegativity is 3.04 on the Pauling scale [75]. Both, gallium (1.81) and arsenic (2.18) have a much smaller electronegativities [75] which makes the Ga-N bond more polar than the Ga-As bond because electron localization around the nitrogen atom is favoured. The Ga-N bond is also more than twice as stiff as the Ga-As bond [104]. Those large differences of its constituents are the source of interesting and sometimes unexpected electronic properties of the GaAsN alloy.

Origin of the Strong Band Gap Bowing

Ding et al. [105] measured by photo-emission spectroscopy that the conduction bands in GaAs and GaN are at about the same level to the vacuum. The band gap changes in a highly non-linear way upon transition from a GaAs-like to GaN-like alloy due to impurity-like, i.e. strongly localized, band edge wave functions in GaAsN [7]. Bellaiche et al. [104] found from ab-initio calculations that for a nitrogen concentration

of x $<$ 10% the Ga-N bond may be considered an impurity in the GaAs host which decreases the band gap rapidly with increasing N content. The conduction band minimum (CBM) is localized in the vicinity of the nitrogen atoms. Thus in dilute concentrations, the variation in the band gap is mostly due to a change in the CBM. For higher N concentrations (x $>$ 40%) in the alloy, the As atom takes the role of the impurity in the GaN host and the valence band maximum (VBM) localizes strongly around the As atom which results in a decrease of the band gap with increasing N content, induced mostly by a change in the VBM. These results are summarized in Fig. 6.3. The ab-initio calculations which led to the plotted band structure are discussed in Section 7.3.

Effects of PII on the Electronic Structure

The electronic structure of the the real implanted material most likely exhibits features that can be seen as a superposition of the limits of bonded N in an alloy and unbound N impurities in the GaAs host. Both cases have localized wave functions due to the electronegativity [75] in the first or spatially isolated impurities in the second limit. Furthermore, the band gap decreases for dilute concentrations in both cases by virtue of movement of the CBM and population of deep gap states, respectively. Therefore, ion implantation may decrease the band gap by either mechanism.

6.4 Models

It is well known that the band gap in ternary III-IV alloys, such as a hypothetical XYZ, bends with increasing amount of one of the binary constituents (XY, YZ). The bending in III-IV semiconductors which do not undergo structural transitions (e.g. direct band gap to indirect or change of the crystal structure) can be described fairly well by a small parabolic correction to the Virtual Crystal Approximation [7, 75]

$$E_g^{XYZ}(x) = \left[x \cdot E_g^{XY} + (1-x) \cdot E_g^{YZ}\right] - b \cdot x\,(1-x)\,, \tag{6.3}$$

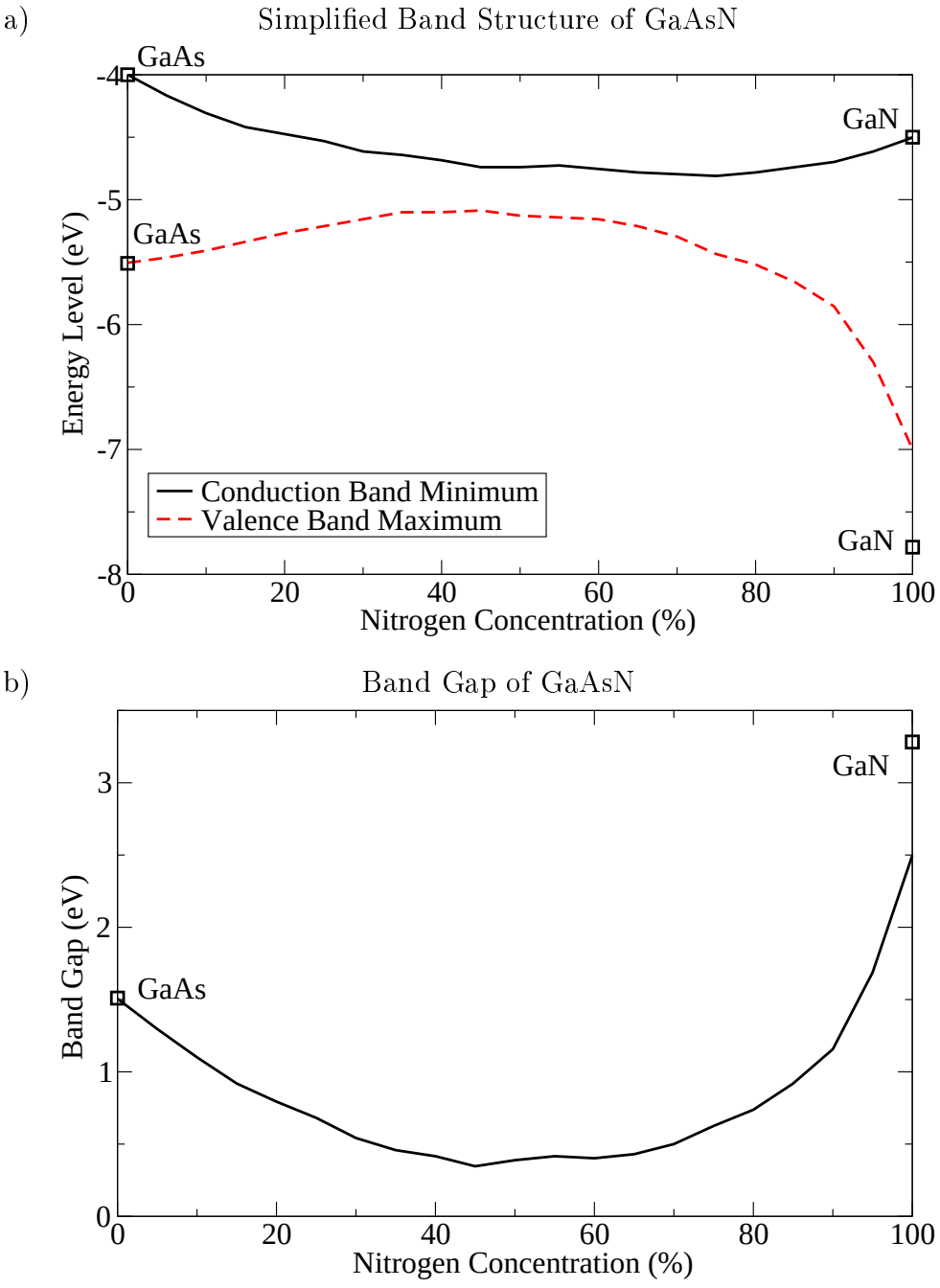

Figure 6.3. Band diagrams of GaN-like and GaAs-like GaAsN alloys from the pseudo-potential calculations of Bellaiche et al. [104]. The band structure for dilute N concentrations is basically a perturbation to the GaAs host. The energy of the conduction band minimum strongly decreases with increasing N content. For high N concentration, the host alloy is GaN perturbed by As. The valence band maximum strongly decreases with increasing N content.

where b is the (concentration independent) bowing parameter. However, the bending in GaAsN is unusually strong because nitrogen forms localized states within the band gap. Eq. (6.3) does not describe the band gap of the GaAsN well and thus, more advanced models have been developed.

6.4.1 Concentration-Dependent Bowing

Tisch et al. [106] used a concentration-dependent bowing parameter obtained from fitting to their extensive set of band gap measurements. They prepared 36 $GaAs_{1-x}N_x$ samples where x was between 0% and 5%. Their samples were synthesized by metalorganic vapor phase epitaxy [107] on semi-insulating (001) GaAs. The band gap was determined by optical transmission measurements at room temperature. This is the largest reported set of samples produced under the same conditions. Tisch et al. basically extended the formula of the virtual crystal approximation

$$E_{\mathrm{GaAsN}}(x) = [x \cdot E_{\mathrm{GaN}} + (1-x) \cdot E_{\mathrm{GaAs}}] - b\,(x) \cdot [x\,(1-x)] \tag{6.4}$$

by a concentration-dependent bowing parameter

$$b(x) = b_0 + b_1 e^{-x/x_1} + b_2 e^{-x/x_2} \tag{6.5}$$

to describe the results of their measurements. The first exponential dominates for nitrogen concentrations smaller than 3% and the second exponential describes the behaviour for higher concentrations. Table 6.1 shows the values of all fitting parameters b_0, b_1, b_2, x_1 and x_2 as well as the band gaps E_{GaN} and E_{GaAs}. A plot of the bowing parameter is presented in Fig. 6.4. The parameter is very large initially and converges to 7.5 eV for higher concentrations. The band gap and its error boundaries are shown in Fig. 6.4. The errors are very large around 50% and also allow for a closure of the band gap. Tisch et al. [106] report these errors, but neither show them graphically nor discuss the errors. However, most of their measured bowing parameters coincide with the solid line in my plots in Fig. 6.4 and Fig. 6.5. The authors show both plots only up to concentrations of about 6%. However, they briefly discuss the application of their model for higher concentrations ($< 10\%$) which are also plotted here.

Table 6.1. Input Parameters for the concentration-dependent bowing model from the report of Tisch et al. [106].

Parameter	Value	Parameter	Value
E_{GaAs}	1.42 eV	E_{GaN}	3.2 eV
b_0	(7.5±2.5) eV	x_1	(0.26±0.04)%
b_1	(21.1±1.3) eV	x_2	(3.3±1.3)%
b_2	(15.9±1.6) eV		

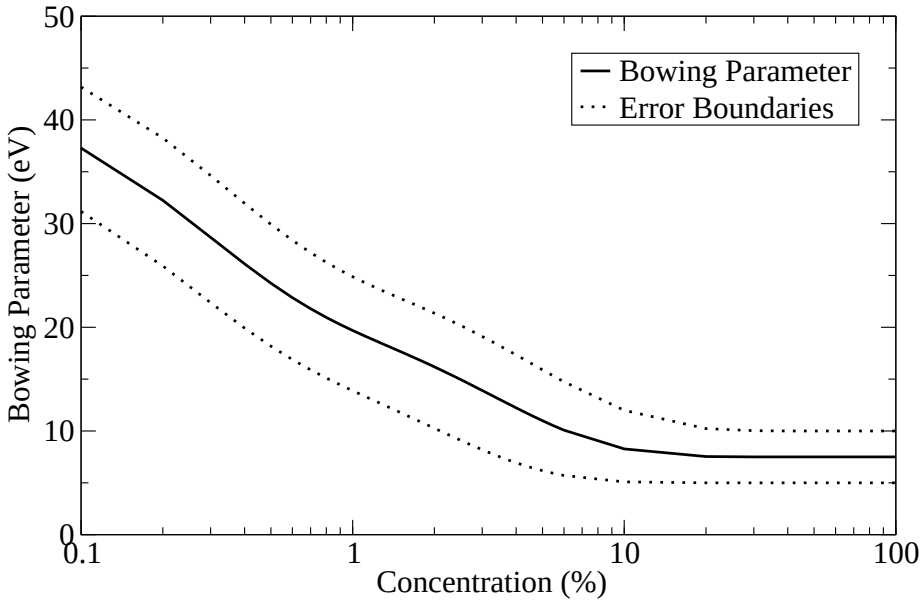

Figure 6.4. Plot of the concentration-dependent bowing parameter from Tisch et al. [106].

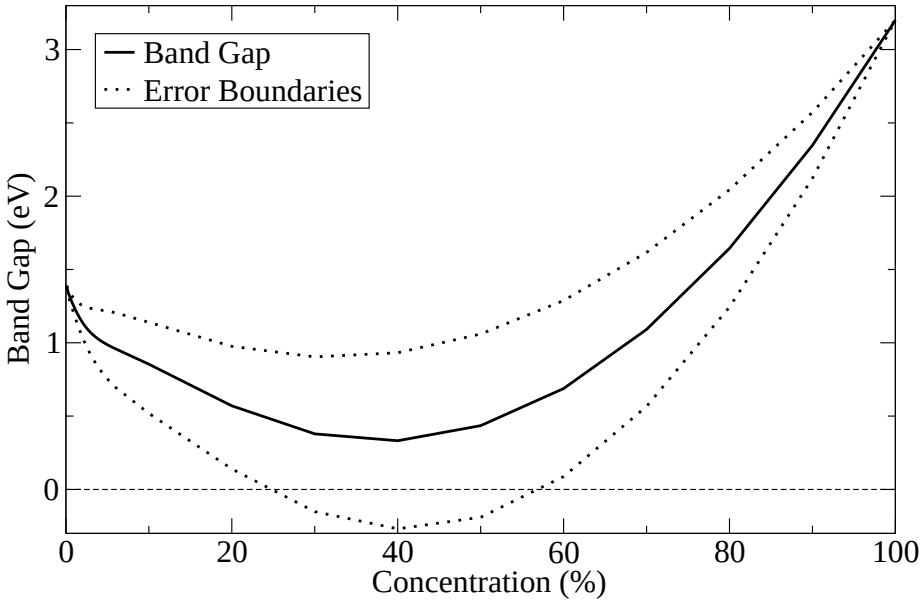

Figure 6.5. The band gap as a function of the nitrogen concentration in the concentration-dependent bowing model of Tisch et al. [106]. The error boundaries are based on the errors reported in the reference.

6.4.2 Band Anti-Crossing

The Band Anti-Crossing (BAC) model was derived by Shan et al. [108] using perturbation theory, hence it is not valid for high N concentrations and yields unphysical negative band gaps there. The underlying idea is that the change in the valence band maximum may be neglected for dilute nitrogen concentrations. The band gap is then given by the interaction between a single, spatially localized N level and the conduction band of the GaAs host matrix. The two band BAC model yields the following energy dispersion

$$E_{\pm}(k) = \frac{1}{2}\left[\left(E^C(k) + E^L\right) \pm \sqrt{\left(E^C(k) - E^L\right)^2 + 4V^2 x}\right]. \tag{6.6}$$

The direct band gap $E_g\,(k=0) \equiv E_g$ is given by

$$E_g = E_-\,(0) \tag{6.7}$$

if all energy constants are expressed relative to the valence band maximum. The lowest conduction band energy of GaAs is then $E^C\,(0) = 1.42$ eV, the energy of the localized N states is $E^L = 1.65$ eV and the coupling parameter between localized

states and the host is $V = 2.7$ eV. The latter two values of those energy constants are recommended in a review by Vurgaftman and Meyer [74]. The first is the band gap of GaAs which is by definition the difference between the conduction band minimum and the valence band maximum. The measured band gaps in dilute GaAsN shown in the review [74] are in good agreement with those values.

The BAC model has the advantage of a simple analytical solution for the effective electron mass

$$m^* = \hbar^2 \left. \frac{1}{\partial^2 E_g(k)/\partial k^2} \right|_{k=0} . \tag{6.8}$$

Taking the derivatives of eq. (C.8) yields

$$m^*_{\mathrm{GaAsN}} = m^*_{\mathrm{GaAs}} \cdot \left(1 + \frac{x \cdot V^2}{(E^L - E_g)} \right) , \tag{6.9}$$

where the effective mass of GaAs is given by $m^*_{\mathrm{GaAs}} = \hbar^2 \left(\partial^2 E^C / \partial k^2 \right)^{-1}$. Fig. 6.6 depicts the effective mass of the GaAsN alloy for nitrogen concentrations up to 10%. The effective mass is inversely proportional to the mobility and hence to the conductivity. An increase of the effective mass as observed in Fig. 6.6 should therefore result in a qualitative decrease of the conductivity if other effects such as scattering are neglected. This case is illustrated in Fig. 6.7. The conductivity initially drops rapidly with increasing nitrogen content. However, the conductivities for concentrations higher than 5% differ scarcely. The plot in Fig. 6.7 should be seen as a trend for the conductivity since conduction is a rather complex process not covered satisfactorily by my simple considerations. The conductivity can be measured by a four-point probe which is the standard for measuring conductivities of thin film semiconductors. The conductivity can also be obtained from contactless (near) infra-red spectroscopy of plasmons at the surface [109, 110, 111].

6.4.3 Ab-Initio Calculations

Bellaiche et al. [104] calculated the change of the valence and conduction bands in the disordered GaAsN alloy for nitrogen concentrations between 0% (GaAs) and 100% (GaN). The alloy was represented by a 512 super-cell with fixed symmetry which allowed for an increase in 0.4% steps. The nitrogen atoms were distributed at

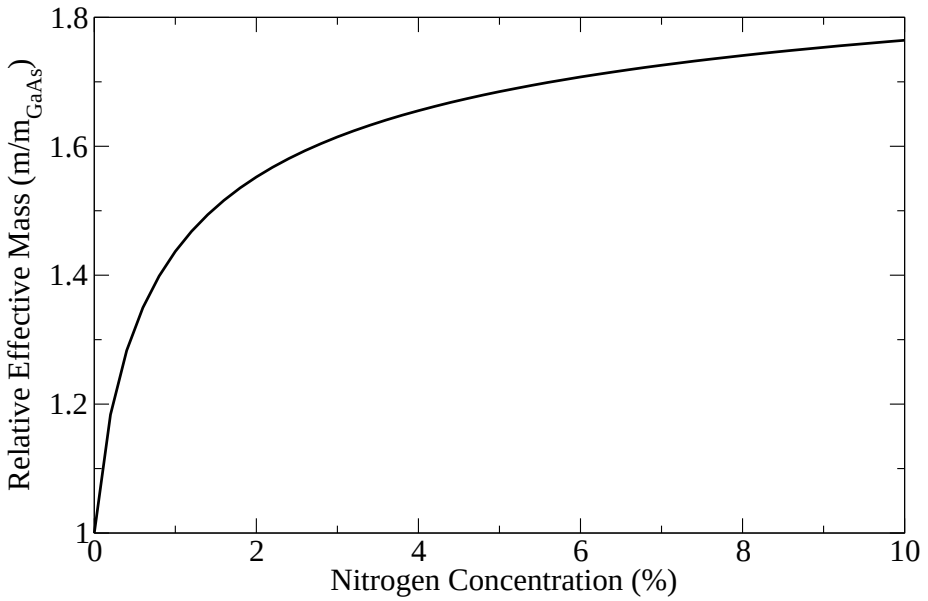

Figure 6.6. The effective mass of the GaAsN alloy from the BAC model in the limit of low nitrogen concentrations.

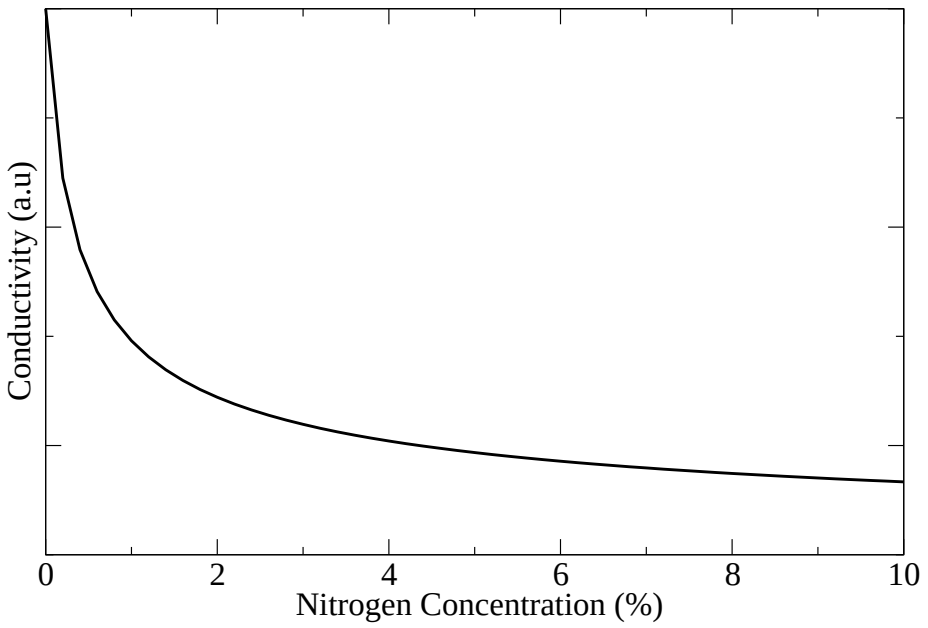

Figure 6.7. Estimation of general trend for the conductivity from the effective mass given by the BAC model [108].

random on the FFC lattice sites for each composition. The electronic properties are obtained via a plane wave pseudo-potential approach which employs local empirical pseudo-potentials that are fitted to physical parameters of the bulk constituents. Their results were used to explain the unexpected variation of the band gap in the last section. Those results are reproduced in Fig. 6.3.

6.4.4 Discussion

The top graph in Fig. 6.8 shows two models for the band gap in dilute GaAsN ($N < 5\%$). Both agree well to an N concentration of about 3% after which they diverge. However, both slopes are supported by measured data. Hence, the band gap of the GaAsN is difficult to model as its measured value may depend on the preparation conditions. The quality of the grown alloy becomes especially important for the concentrations higher 3% which is why the measured data diverges.

The concentration-dependent bowing model predicts a meaningful band gap over the full range of possible concentrations that agree in general features with the calculations of Bellaiche et al. [104], see the graph in Fig. 6.8 b). The BAC model was derived under the assumption of a (small) perturbation of the GaAs host crystal. Therefore, it cannot describe higher concentrations and yields an unphysical negative band gap for high concentrations. It does agree well with the measured band gaps for low N concentrations and may thus be used to estimate the mass and the trend of the conductivity in these alloys.

The reported values of the band gap and its dependence on the concentration depend heavily on the fabrication parameters and method as well as the technique used to characterize the alloy. It is therefore necessary to find a standard for nitrogen ion implanted GaAs, especially since the band gap varies within the material which I will discuss in Section 7.3. The models described above will be helpful as a starting point, but I expect the measured band gap variation in my samples to deviate slightly from the models presented in this section due to the disorder inherently introduced by ion implantation.

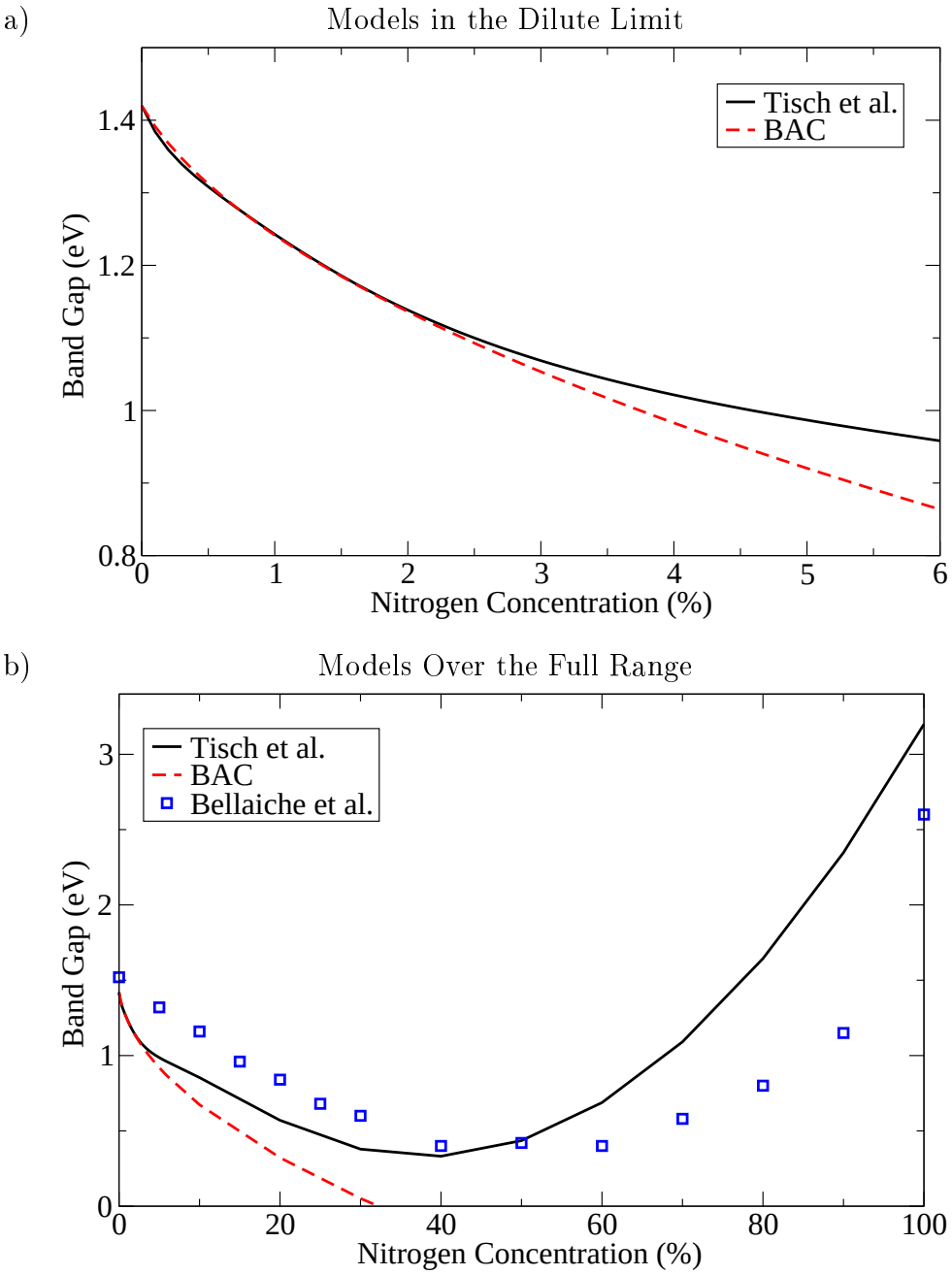

Figure 6.8. Comparison of different models for the non-linear variation of the band gap in the GaAsN alloy. The model of Tisch et al. [106] is semi-empirical, the BAC model [103] is derived from perturbation theory and Bellaiche et al. [108] did pseudo-potential calculations. The slopes in the top graph agree with measurements. It is not yet possible to synthesize concentrations $> 14.8\%$, so the lower graph is compared to predictions from the pseudo-potential calculations.

Chapter 7

Depth Profiles

The distribution of the implanted ions within the material will be discussed in this section. The distribution will be referred to as a 'depth profile' from now on. These profiles have Gaussian shape for nitrogen implantation into gallium arsenide and can be characterized by the mean and the standard deviation which are called range and straggle in the ion implantation community. The Handbook of Plasma Immersion Ion Implantation and Deposition [10] contains a comprehensive introduction to the physics of ion-solid interaction.

The incident fluence (ions per unit area) distributes within another dimension (the depth in the sample) during the implantation process. The unit of the resulting quantity should therefore be ions per unit volume and is usually called dose. The definition of 'the dose of the sample' is not meaningful due to the depth distribution of the implanted ions and an ambiguity of the implanted volume. However, I define the dose as the number of ions that are in the target at the end of the implantation process.

The sample is electrically connected to the electrode during the implantation. The conductivity of GaAs should be high enough to supply electrons to neutralize the ionic charge. Hence, I assume that the implanted nitrogen ions become neutral atoms at their final destination within the GaAs target.

7.1 TRIM

The depth distributions of nitrogen ions implanted into gallium arsenide can be calculated using the TRIM (**Tr**ansport of **I**ons in **M**atter) software in the SRIM 2008 [112]

program collection which can be downloaded at www.srim.org. The software is a Monte Carlo simulation of the implanted ions' trajectories through an amorphous material. The GaAs samples I used were initially crystalline of poor quality as discussed in Sections 4.1 and 8.4, but the relevant volume can be considered amorphous due to impinging ions after the first few pulses. The basic principle of the simulation is to follow a large number of ion histories with dimensions of energy, position and direction. The particle may only change its direction due to binary nuclear collisions and moves in a straight free flight path between collisions. The particle is not followed any further if the energy drops below a defined threshold or the particle's position is outside of the material. The method is applicable over ten orders of magnitude in energy from 100 eV to GeVs where the lower boundary is due to inclusions of binary collisions only and the upper boundary arises from the dependence on the ion mass and the neglected higher order relativistic effects. In any case, inelastic energy loss to nuclear reactions is not included. Typical depth profiles of TRIM for nitrogen implantation into GaAs are shown in Fig. 7.1.

7.2 TRIDYN

TRIDYN [113, 114] FZR V 4.0 is a derivate of the TRIM code which includes dynamic composition changes in the target[1]. The Forschungszentrum Dresden-Rossendorf (FZD also FZR) kindly issued a free license to the Bradley group. The software calculates the depth profiles of all constituents in the target as function of the incident fluence, i.e. in this study a separate depth profile for gallium, arsenic and nitrogen. The simulation employs pseudo particles which represent a fraction of the final fluence. Therefore, the precision of the calculation may be increased by a larger number of pseudo particles per fluence unit at the expense of computation time. The calculation of those depth profiles includes sputtering at the surface and saturation of a species in the target. TRIDYN and TRIM cover only non-thermal processes. Moreover, TRIDYN does not include any chemistry; all results are exclusively due

[1] TRIDYN is an acronym for **T**ransport and **R**ange of **I**ons for **DYN**amical composition changes.

to effects of physical sputtering. TRIDYN branched off early from TRIM and does not include some of the corrections for the MeV ion energy regime. The lower energy boundary of TRIDYN is 10 eV. Nevertheless, collisional processes with slightly lower characteristic energies, such as sputtering, are also predicted quite accurately [115].

7.3 Tailored Depth Profiles

The ideas and concepts discussed in this section were published in physica status solidi c as a contribution to the proceedings of the 9th International Workshop on Plasma Ion Implantation and Deposition in Leipzig, Germany (2007) [94].

All results are based on a TRIM simulation of 50,000 ions, a number high enough to converge the values of their distribution's momenta to at least the second decimal. The binning size is 1 nm in the depth profile predictions and 4 nm for band gap predictions to assure enough atoms for a meaningful definition of the band gap, cf. discussion in Section 6.2. The simulation accounts for the 10 to 20% of fluence lost due to recoil on the surface, but the change in the surface due to sputtered target atoms is not included. The following assumptions were made:

- The implanted particles are mono-energetic.
- The nitrogen molecules break into single atoms.
- The molecules energy is distributed equally amongst the daughter atoms.
- The temperature during implantation is low enough to neglect diffusion.
- All nitrogen atoms in the target are part of the GaAsN alloy, i.e. they are not interstitial.

It is almost certain that the molecular ions collide with the target within the first few monolayers. The kinetic energy of the impact is high compared to the bond energy and will therefore break the bond. It is very unlikely that all nitrogen atoms occupy lattice sites since the nitrogen atom's cross section is much smaller than the

the cross sections of gallium or arsenic. Moreover, gas ion implantation is likely to create gas-filled voids in the target. The peak height of certain bands in Raman spectroscopy could be used to estimate the fraction of the implanted nitrogen that is part of a GaAsN alloy. Yu et al. [84] reported that this fraction was about 10% in their study. However, this assumption is essential for my method of band gap calculation.

The depth profiles are designed to have a trapezoidal shape with a plateau as wide as possible, cf. Fig. 7.2. The concentration at this plateau is chosen in such way that the estimation of the band gap yields a value of 0.95 eV (1.3 μm). The profiles could be composed by subsequent implantation with near rectangular voltage pulses at 4 voltages: 20 kV, 10 kV, 4 kV and 2 kV. The 3 ion species in the N plasma yield 3 doses per implantation which means that 12 fluences are needed to predict the depth profiles in Fig. 7.2; their expected values are shown in Table 7.1. The profiles were weighted according to the population of the ion species and multiplied by the number of atoms the molecules break into. This step of the calculation is shown in Fig. 7.1 for the -20 kV implant. The main contribution (91%) to the depth profiles stems from N_2^+ ions; other ions only contribute an undesired, weak background. Predictions of TRIM depth profiles have been confirmed extensively in experiments [112]. Thus, I am confident that the concentration depth profiles are accurate if diffusion is low.

Table 7.1. Calculated nitrogen ion fluences for a depth profile with 6% peak concentration of N in GaAs, broken down by implantation voltage (head row) and the ion species (first column). Errors are not shown for clarity. All fluences are given in ions/cm^2 and rounded to the nearest integer.

	2 kV	4 kV	10 kV	20 kV	Total
N^+	8	4	4	95	111
N_2^+	72	37	41	1023	1174
N_3^+	1	1	1	18	20
Total	81	41	46	1136	1305

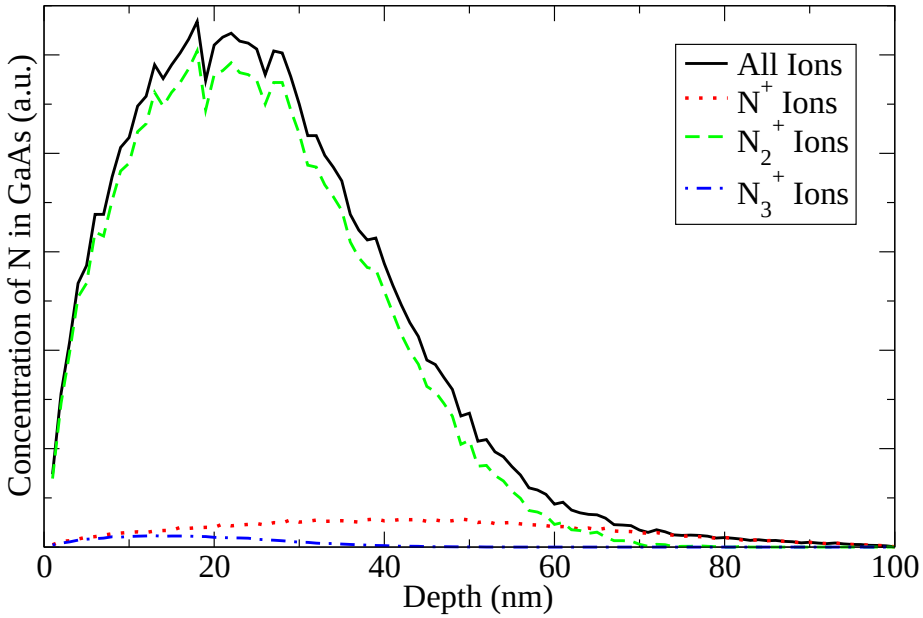

Figure 7.1. Contributions of the ion species to a depth profile for a mono-energetic -20 kV TM pulse as calculated by TRIM [112]. The effects of finite pulse rise and fall times on the ion energy distribution were neglected. The ion populations are given in Table 7.1. Errors were omitted for clarity.

The prediction of the band gap within the material employs the concentration-dependent method reported by Tisch et al. [106], i.e. eq. (6.4) and the parameters given in Table 6.1. The concentration was converted into a band gap for each 1 nm binning interval and subsequently averaged to one value every 4 nm. The resulting band gap profile is plotted in Fig. 7.3. A layer of about 30 nm width with the desired band gap of 1.3 μm (0.95 eV) is formed near the surface. The error boundaries are entirely due to the uncertainty in the fluences. The (optical) band gap could be measured using Photoluminescence (PL) spectroscopy or via the Urbach edge from transmission spectroscopy. The average penetration depth of laser light at 500 nm wavelength is 93 nm in GaAs [116] which should yield strong signals from the implanted layer that are clearly distinguishable from the GaAs background.

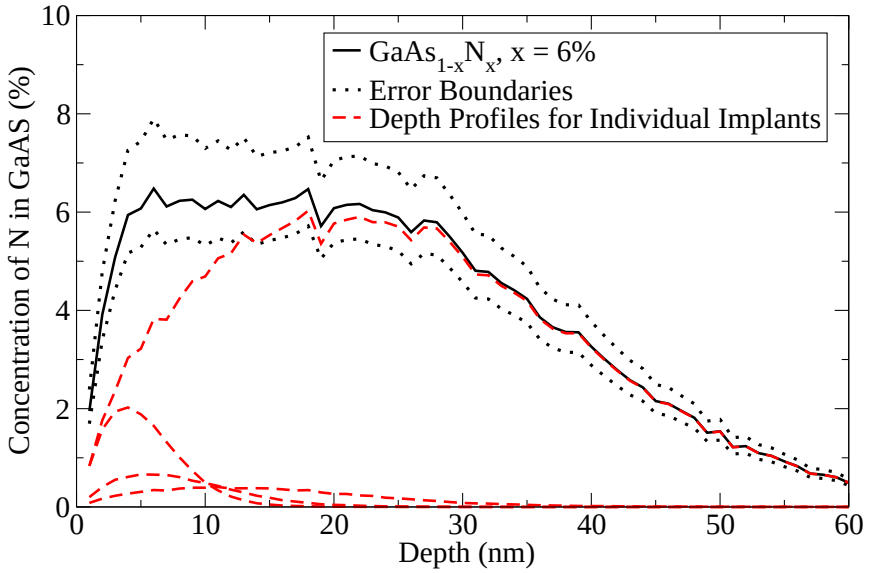

Figure 7.2. Depth profiles including error boundaries of a GaAsN alloy calculated using TRIM [112]. Shown is the profile whose concentration (solid black line) corresponds to a band gap of 1.3 μm (0.95 eV). Also shown are the depth profiles of the individual implants (dashed red lines) which were added to produce the figure. The error boundaries in the plots shown are exclusively due to the estimated errors in the fluence.

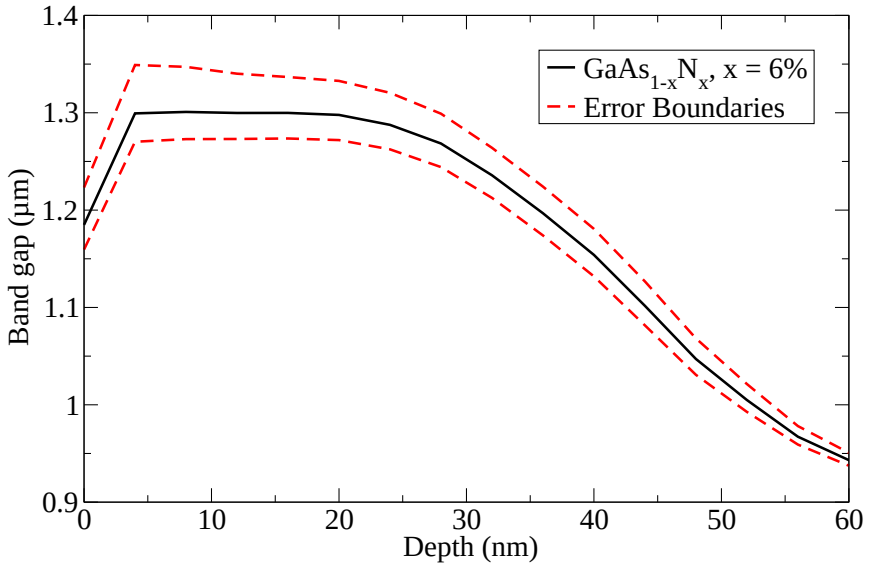

Figure 7.3. Predicted spatial variation of the band gap for the $GaAs_{1-x}N_x$ alloy with x = 6% shown above. The calculation of the band gap from the concentrations employed the method and constants reported by Tisch et al. [106]. The error boundaries in the plots shown are exclusively due to the estimated errors in the fluence. Note also that the band gap is given in units of micro meters to ease a comparison with the desired emission wavelength of 1.3 μm (0.95 eV).

7.4 Results and Discussion

Implantation in the Transformer Mode

The depth profile of ions implanted with a -10 kV voltage pulse in the 'Transformer Mode' is shown in Fig. 7.4 b). Part a) of the figure contains the energy distribution diagram of the applied voltage pulse which is displayed in the inset. The depth profile was simulated by the TRIM software and does not include effects due to sputtering. The lower energy components render it impossible to tailor depth profiles since they are present with any plateau voltage of the pulse. The depth profiles of the higher energy contributions are more similar to the distribution of the peak implantation energy. Their effect is thus to increase the concentration at the peak. The dominance of N_2 ions in the plasma decreases the attainable maximum layer width. The range of N^+ ions implanted in GaAs with the full potential of -10 kV is 22.5 nm whereas the range of the N_2^+ ions is only 12.5 nm. The problem of the low energy contributions can be solved by applying a more rectangular voltage pulse, but the gas composition cannot easily be altered to improve the implantation depth. The effects of lower and higher energy bands are neglected in the following paragraphs to show the other contributions to the depth profiles more clearly.

Formation of the GaAsN Alloy

Fig. 7.5 shows the result of implanting 2.5×10^{15} nitrogen ions per cm^2 into a GaAs sample with a single energy of 5 keV . Gallium atoms pile up near the surface, whereas the arsenic concentration decreases there. The decrease of the Ar concentration on the surface was also measured by Lin et al. [95] using Rutherford Backscattering Spectroscopy (RBS). The target is essentially unmodified for depths deeper than 40 nm. The concentrations of both Ga and As are slightly lower than the stochiometric value (Ga_1As_1) in the vicinity of the peak in the nitrogen depth profile.

Fig. 7.6 shows the same implantation, but the arsenic and nitrogen depth profiles are now plotted relative to the gallium content, in order to study the formation of the

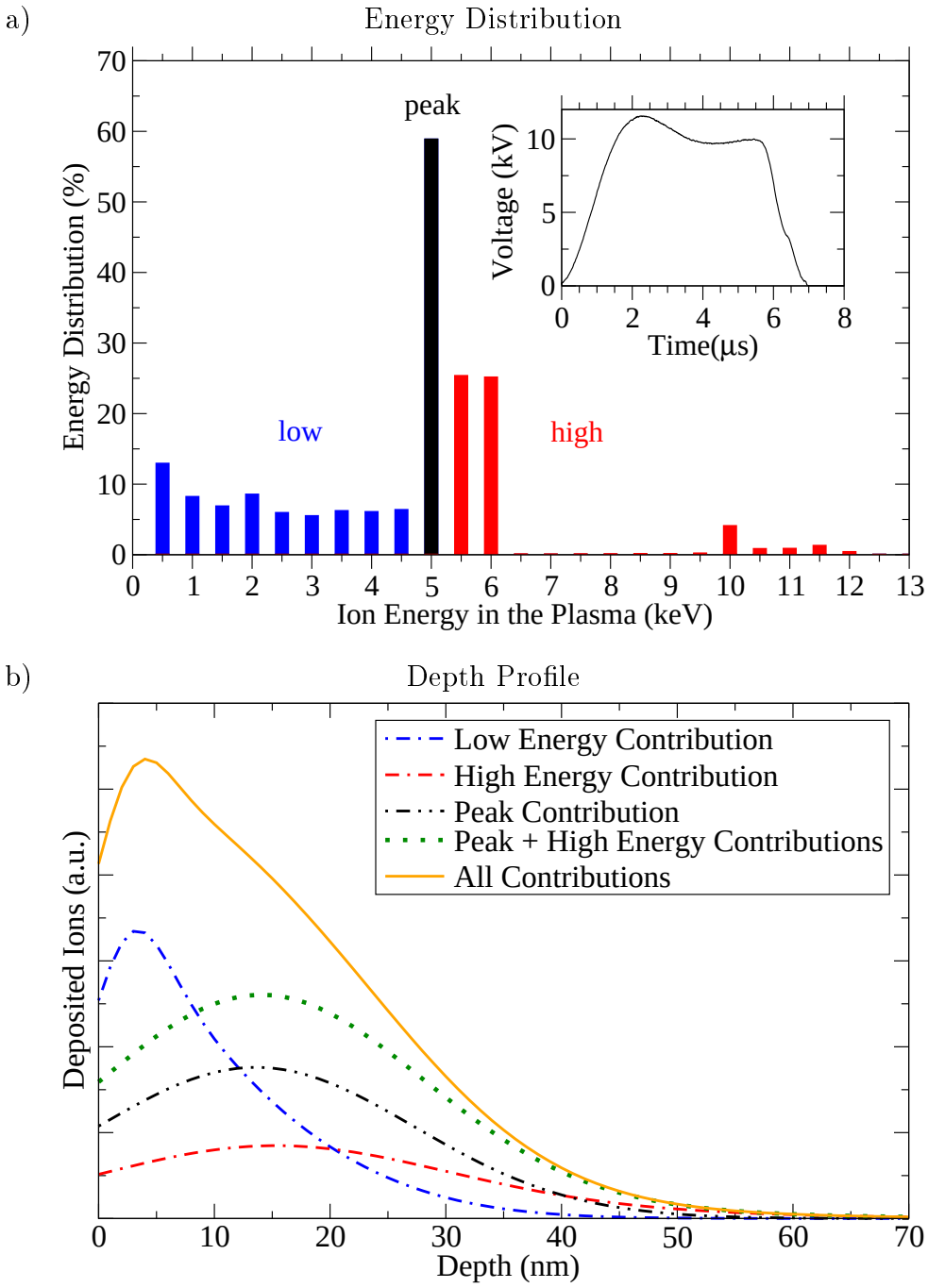

Figure 7.4. Energy distribution and resulting TRIM depth profiles of nitrogen ions implanted with the voltage shape shown in the inset of a). The conditions during implantation are gathered in Table 5.2. Ion energies below the peak in the energy diagram at 5 keV are labeled low and the energies higher are labeled high. The depth profiles produced by these contributions are shown in b).

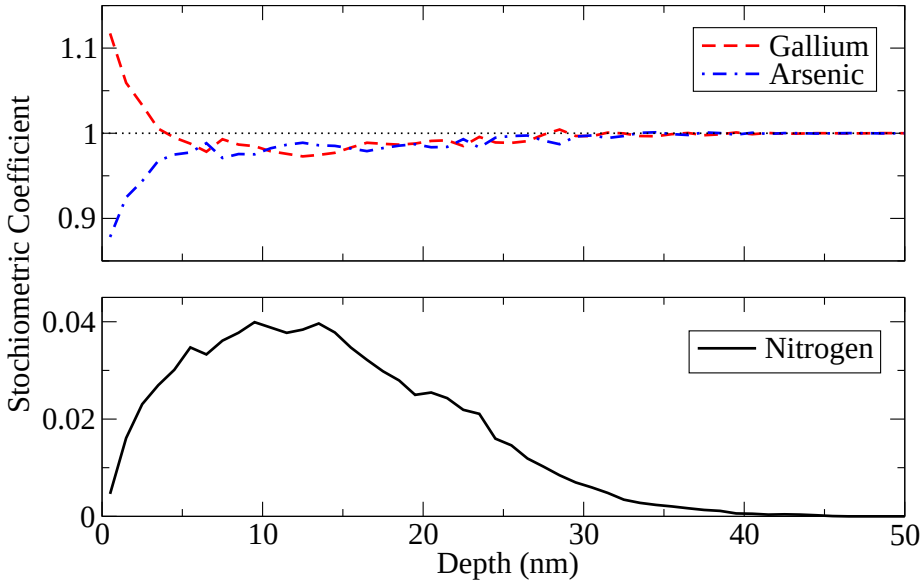

Figure 7.5. Depth profiles of gallium, arsenic and nitrogen after nitrogen ion implantation. The calcuation was done by the TRIDYN simulation using 10,000 pseudo particles, a fluence of 2.5×10^{15} ions/cm^2 and an ion energy of 5 keV.

$Ga_1As_{1-x}N_x$ alloy. The arsenic content from the TRIDYN simulation is represented by the blue dash-dot line and the green dash-dot-dot line shows the arsenic content expected from the alloy $GaAs_{1-x}N_x$ for the simulated nitrogen depth profile. This representation clearly shows that the desired alloy does not form after nitrogen ion implantation, even for the highly unlikely case that all nitrogen atoms would occupy lattice site, i.e. bond to the surrounding atoms. The profiles diverge at the surface due to sputtering of As atoms there. As and Ga atoms are displaced in equal numbers deeper in the target which prevents the proper ratio of the constituents to form the alloy. Further processing, such as annealing, is therefore necessary to synthesize the GaAsN alloy using plasma ion implantation.

TRIDYN Depth Profiles of Nitrogen Ions

The TRIDYN software can also be used to study the change of the depth profiles for increasing fluences. Those plots are shown in Fig. 7.7 a) to c). The depth profiles of the high-dose implantations are very noisy as the number of pseudo-particles was not sufficient. Nevertheless, the correct trend of a Gaussian distribution is clearly

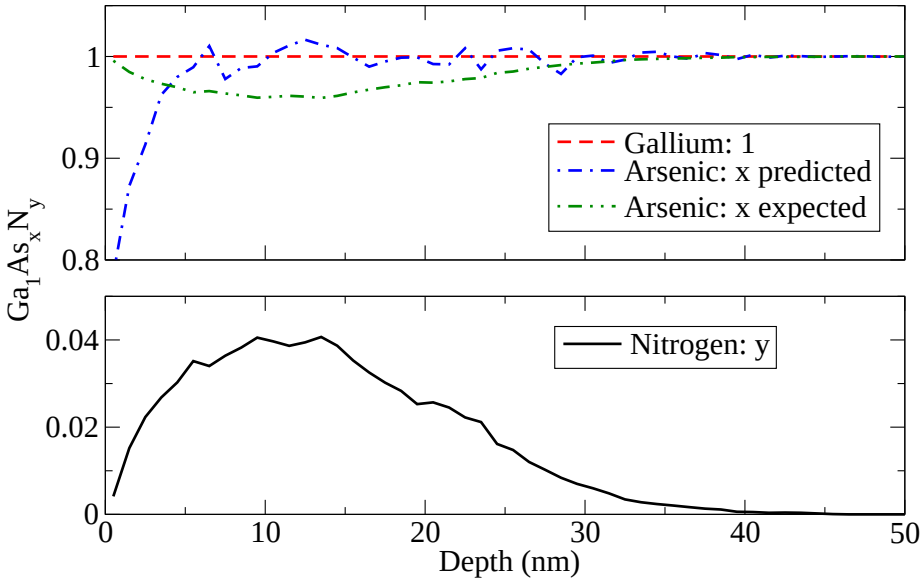

Figure 7.6. Depth profiles of arsenic and nitrogen relative to the gallium concentration. This plot shows that the GaAsN alloy does not form after plasma ion implantation because the predicted arsenic content (blue dash-dot line) deviates strongly from the arsenic content expected in the GaAsN alloy (green dash-dot-dot line). The calcuation was done by the TRIDYN simulation using 10,000 pseudo particles, a fluence of 2.5×10^{15} ions/cm^2 and an ion energy of 5 keV.

visible. A higher fluence applied to the target on the one hand increases the Ga concentration on the surface and on the other hand decreases the As concentration. Yet another phenomenon becomes apparent: the retained dose saturates, i.e. an increase of the fluence above the threshold does not change the depth profiles. The maximum concentration of nitrogen in GaAs is about 25 atomic percent. This is well below the 50 atomic percent needed to form GaN directly by ion implantation. It was furthermore found from the simulation that for the lowest fluence 2.5×10^{15} ions/cm^2, about 80% of the fluence is implanted whereas for the highest fluence 10^{18} ions/cm^2 only 2% of the initial ions stop and remain within the target. I estimated the maximal fluence retained in GaAs for 5 kV implantation of N ions as about 2.5×10^{16} ions which yields the peak at 25 atomic percent.

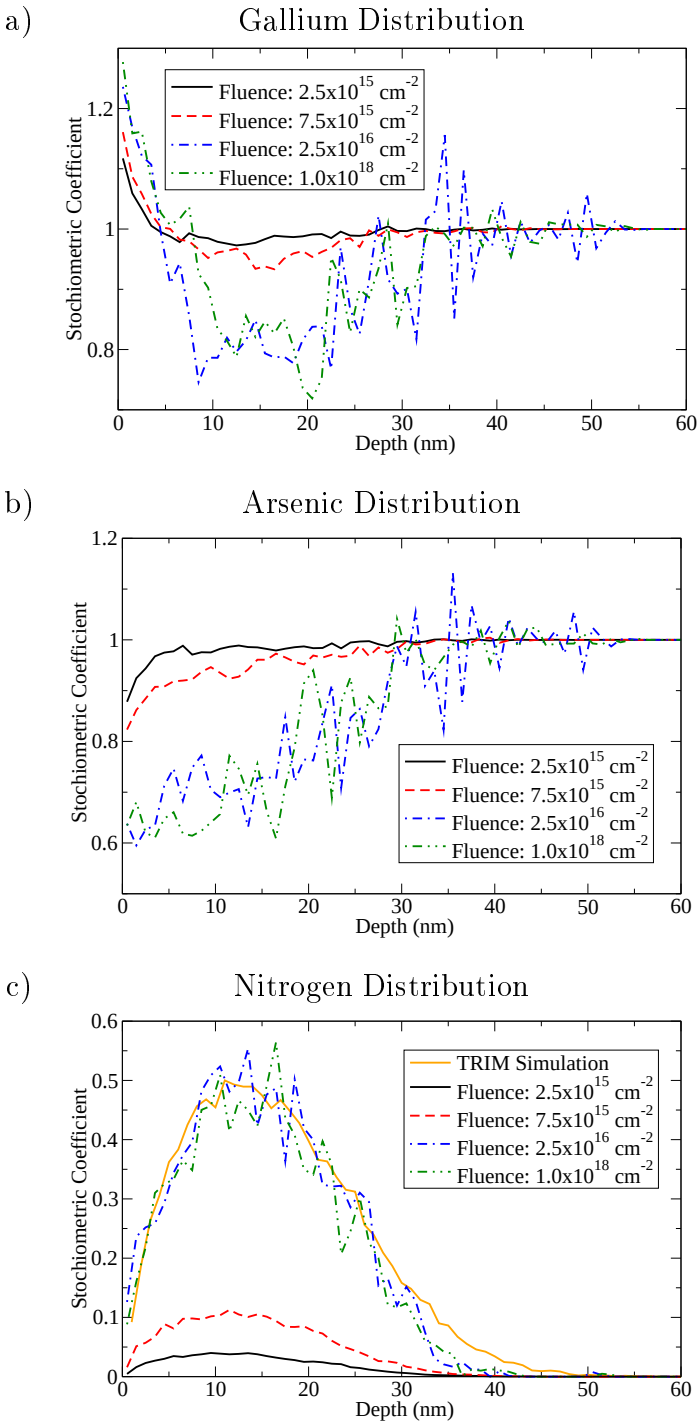

Figure 7.7. TRIDYN depth profiles of gallium, arsenic and nitrogen for various fluences of 5 keV nitrogen ion implantation. The plot of the nitrogen depth profile also shows the result of a TRIM simulation for comparison.

TRIDYN vs. TRIM

Fig. 7.7 c) also shows a reasonable agreement between the output of the TRIM simulation (orange solid line) and the TRIDYN simulation (other graphs). Erosion of the surface due to sputtering may thus be neglected and the faster TRIM software can be used to predict the depth profile under the condition that the retained dose is known. TRIDYN should therefore be employed to obtain an estimate of the retained dose with a reasonably low number of pseudo-particles. The actual depth profile can be obtained from TRIM or even using a Gaussian distribution if TRIDYN predicted higher order distribution moments close to zero. This situation is most likely for ion implantation perpendicular to the surface of the target.

Sputtering

The concentrations at the surface as well as the maximum retainable dose may be explained by the ejection of the surface atoms, which is called sputtering. Fig. 7.8 shows the sputtering yields for a wide range of incident fluences impinging at an ion energy of 5 keV. The yield equals the number of ejected surface atoms per incident nitrogen ion. The sputtering yield of gallium remains almost constant for the shown fluences and is about half of the yield for arsenic atoms for low fluences. This difference is the origin of the build-up of Ga atoms on the surface of the target after implantation. The sputtering yield of nitrogen atoms increases strongly with increasing fluence and the yield of As decreases with increasing fluence. For high fluences, previously implanted nitrogen is preferably sputtered which explains the maximum retainable dose of N in GaAs.

Retained Dose

The connection between sputtered nitrogen ions and the retained dose is plotted in Fig. 7.9. It is evident that sputtering limits the retained dose. The plot also contains the decrease of the retained dose due to reflected ions which is approximately constant for the shown fluences. Both the reflected ions and the sputtering yield depend on

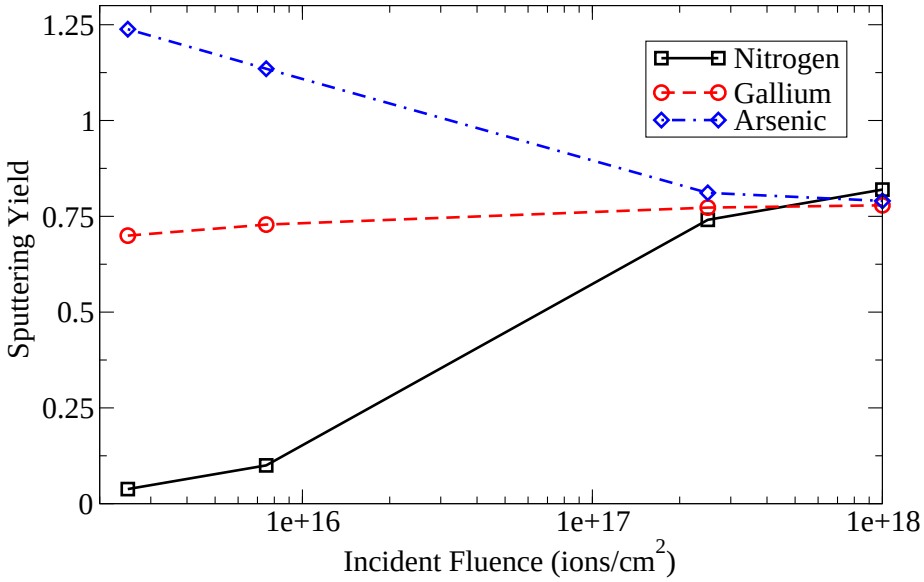

Figure 7.8. Sputtering yields for nitrogen ion implantation into gallium arsenide from the TRIDYN simulation. The ion energy is 5 keV.

the kinetic energy of the incident ions. The number of reflected ions as a function of the nitrogen ion energy is plotted in Fig. 7.10. More energetic ions are less likely to be reflected. Since more energetic ions penetrate deeper into the target, their concentration at the surface will be lower, which also influences the sputtering yield. Thus, the sputtering yield of nitrogen decreases with increasing ion energy. More ions reach the target and and remain there if both reflection and sputtering decrease with higher ion energy. Furthermore, the increase in the ion range results in a wider distribution of the ions within the target. Therefore, a higher ion kinetic energy results in an increased retained dose.

7.5 Annealing

Annealing is the heat treatment of a sample to change some of its properties. It is a necessary step after ion implantation to activate the implanted ions, i.e. to stimulate the formation of new bonds with the target's constituents. In fact, there is not a single report [77, 79, 85, 86, 87, 82, 83, 84, 81, 88, 80, 90, 91, 92] of ion implantation of N into GaAs for a composition change without the annealing step following the actual ion implantation. The annealing generally not only fosters the creation of

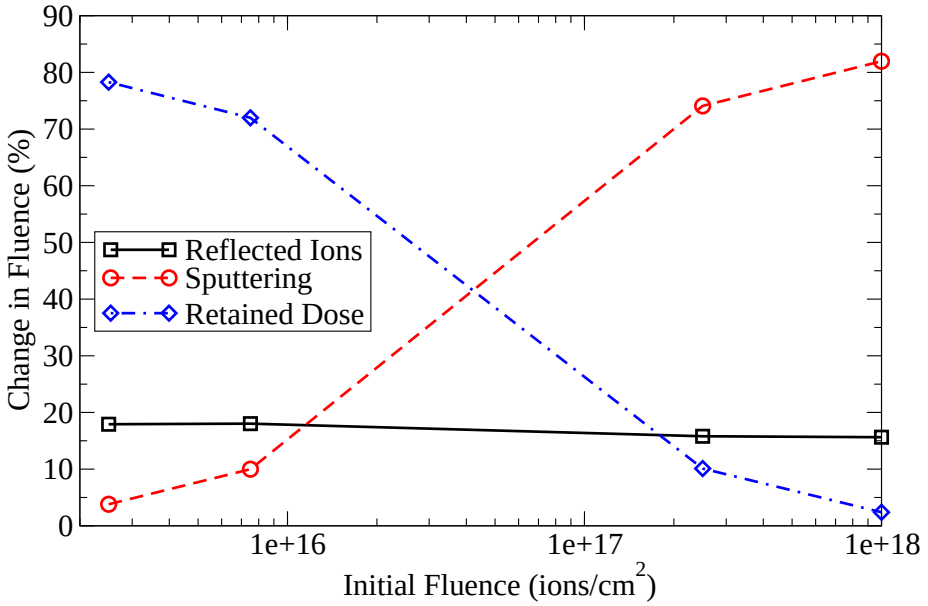

Figure 7.9. Correlation between the retained dose and sputtering of nitrogen atoms. Also shown is the nearly constant reduction of the retained dose due to reflected ions.

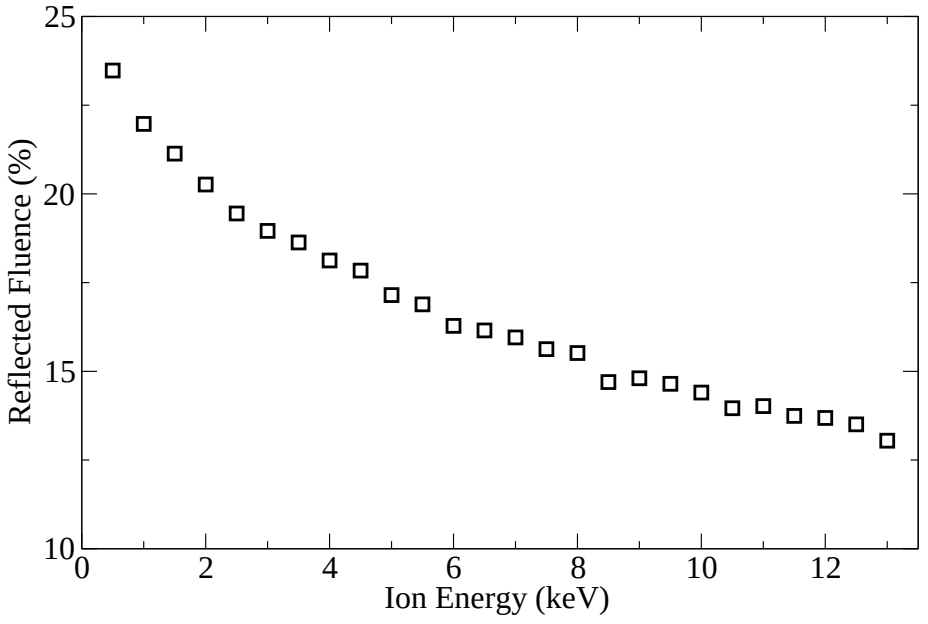

Figure 7.10. Fraction of the fluence that is reflected instead of implanted. The data was obtained from TRIM simulations.

new bonds, but also reduces disorder. Typical annealing times to forge Ga-N bonds by conventional furnace annealing are of the order of 10 minutes to 2 hours at a temperature of 850°C [95]. However, concentrations above the stochiometric limit for a given compound which are possible to obtain by ion implantation will be destroyed in the heating process.

Annealing drastically alters the depth profiles of the implanted ions and thus complicates tailoring of depth profiles and ultimately band gap engineering. However, the SUPREM simulation [117] comes to the rescue. The software simulates the diffusion of atoms during annealing for silicon and gallium arsenide semiconductors. It is available at no cost from the web page of the Integrated Circuits Laboratory at Stanford University. Diffusion during annealing will be included in my method for tailoring depth profiles due to the crucial role of annealing for the formation of new materials by ion implantation.

The U of S Plasma Laboratory owns a Branstead Thermodyne tube furnace model F21100 which can generate temperatures up to 1200°C. Tube and boat are made from alumina (Al_2O_3). The annealing setup is not rated to anneal materials which release toxic or flammable gases during heating. GaAs outgases toxic arsenic fumes during heat treatment, see MSDS data sheet in Appendix B.1. Therefore, the ion implanted samples cannot be annealed with the current apparatus.

Chapter 8

Raman Spectroscopy

The Raman effect is the inelastic scattering of light on the electrons forming the bond in a lattice or molecule. The majority of the incoming light is reflected, absorbed or elastically scattered and only a small fraction interacts inelastically. It is therefore not surprising that inelastic scattering was not discovered until 1928. As a twist of history, the effect was then reported almost simultaneously by Raman and Krishnan [118] in India as well as Landsberg and Mandelstam [119] in Russia.

The physics of Raman spectroscopy with semiconductors is discussed by Perkowitz [116], Weber and Merlin [120] and Turrell [121]. The reviews by Loudon [122] and Abstreiter [123] may also be recommended, despite their age. Herzberg [124] gives the full quantum theoretical treatment of the Raman effect which is beyond the scope of this report. I will furthermore restrict the discussion to the interaction of photons with phonons. Raman scattering of plasmons, electrons or spin waves is covered in the references, but not relevant for this study.

The spectra in Raman spectroscopy usually show the energy shift relative to a known light source which is an Ar^+ laser at the 514 nm line in this study. The (spectroscopic) wavenumber

$$\tilde{\nu} = \frac{1}{\lambda} = \frac{1}{2\pi}\frac{\Omega}{c} \tag{8.1}$$

is used to express this shift and has units of cm^{-1}. It is proportional to the angular frequency Ω[1] and often referred to as 'frequency', regardless of its unit.

In the following discussion, I will refer to crystal surfaces expressed in the Miller

[1]Reports from the 1960's often use the angular frequency or the frequency in units of cps (cycles per second = Hz).

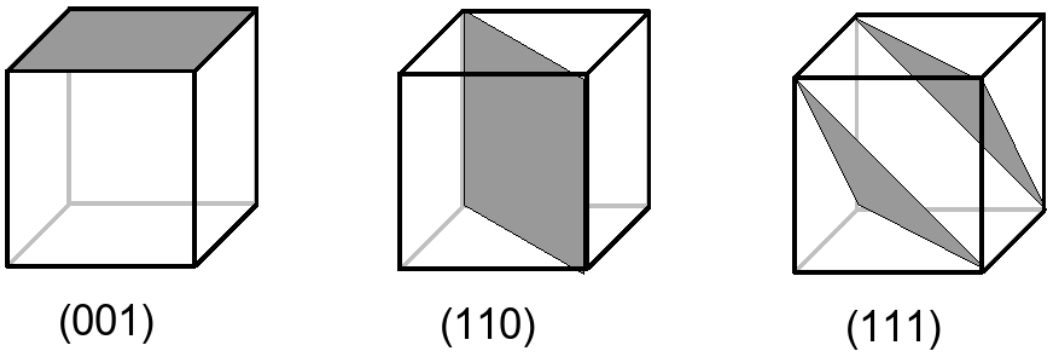

Figure 8.1. Miller notation for the planes used in the discussion. The planes are represented by the shaded areas.

notation for cubic unit cells. The three numbers in the brackets (x y z) represent the normal vector to the plane they refer to, e.g. (001) is the xy-plane. Kittel [3] or Kasap [98] provide a comprehensive discussion. Fig. 8.1 shows the planes I use in the following sections.

8.1 Lattice Vibrations

The atoms in a crystal can be thought of as an array of pearls on elastic strings, cf. Fig. 8.2 and Fig. 8.3. Born and von Karman used this (diatomic) linear chain model to explain a simple ionic crystal. The basic ideas are discussed very concisely by Turrell [121]. In the case of GaAs, there are two constituents with distinct masses coupled by a force constant given by the bond. If only the nearest neighbour interactions are considered, the problem reduces to the solution of two masses coupled by equal springs. There are two solutions per direction: the acoustic branch whose frequencies fall into the domain of sonic and ultra-sonic waves as well as the optical branch which has frequencies in the visible or near infra-red spectral region. Both can be observed in Raman spectroscopy with an appropriate choice of the apparatus and the semiconductor.

In a three dimensional crystal, atoms can move either longitudinal (L), i.e. parallel to the direction of their propagation $\vec{k}$, or transversal (T) which is perpendicular

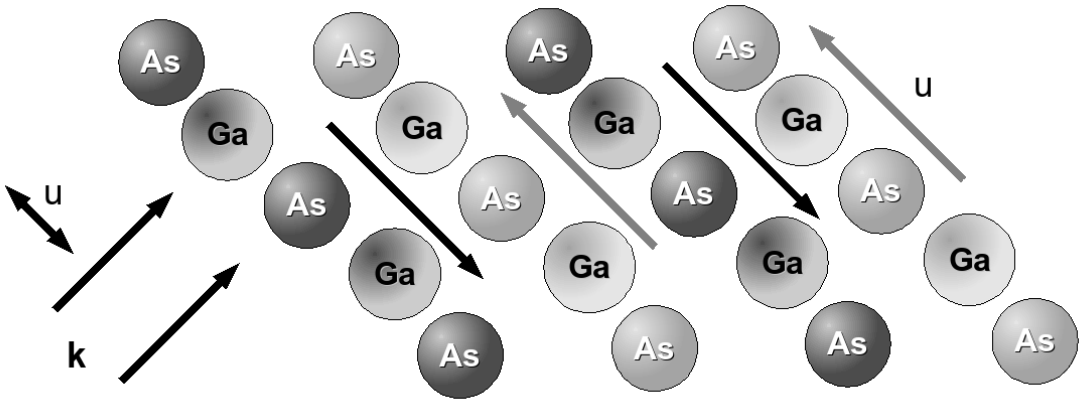

Figure 8.2. Schematic of transverse modes in GaAs.

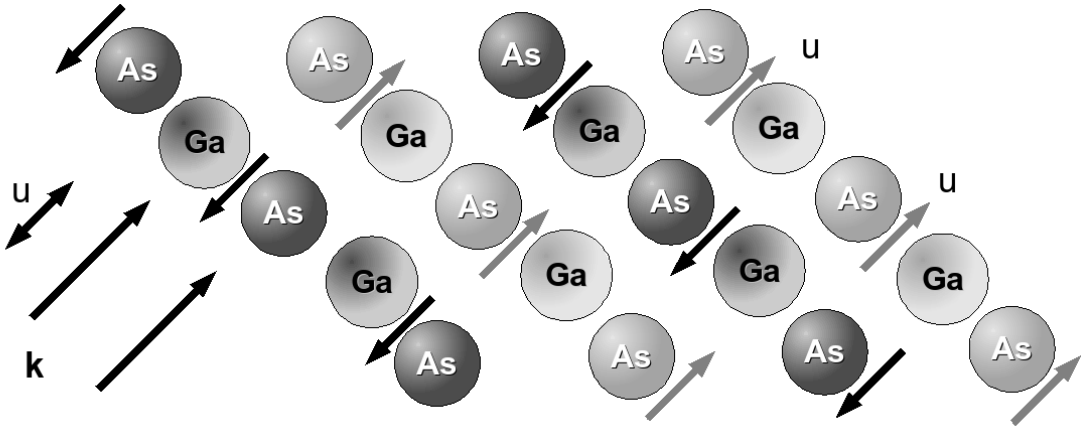

Figure 8.3. Schematic of longitudinal modes in GaAs.

to $\vec{k}$. The modes are illustrated in Fig 8.2 and Fig 8.3, respectively. Waugh and Dolling [125] discuss the phonon dispersion in GaAs. In the case of imperfect crystals, the transitions with (reduced) wavevector other than k = 0 become more likely. This is the origin of the peak broadening due to disorder.

8.2 Interaction of EM Waves and Matter

The light emitted by the Ar^+ laser used in the measurements may be approximated fairly well by a plane wave. The coordinate system will be chosen, so that this plane wave propagates in positive z-direction. The electric field of the light wave is then given by

$$\vec{E}(z) = \vec{E}_0 \cdot \exp(ikz - i\omega t), \tag{8.2}$$

where $\vec{E}_0$ is the amplitude of the radiation, k is the wavevector and ω is the angular frequency of the photons. The wave equation in semiconductors for plane waves is given by [116]

$$\varepsilon_L \varepsilon_0 \mu_0 \omega^2 \vec{E} + \sigma \mu_0 i\omega \vec{E} = \frac{\omega^2}{c^2} \varepsilon(\omega) \vec{E}, \tag{8.3}$$

where ε_0 is the permittivity of free space, μ_0 is the permeability of free space, c is the speed of light in free space and ε_L is the permittivity of the lattice which describes its polarization caused by the interaction of the electrons and atoms in the lattice. The wave equation also defines the (total) dielectric response function

$$\varepsilon(\omega) \equiv \varepsilon_L(\omega) + \frac{i\sigma(\omega)}{\varepsilon_0 \omega}, \tag{8.4}$$

which combines the polarization effects of the bound charge and the free carrier current in the semiconductor. In the linear response limit, this is the central equation describing the interaction between the semiconductor and electromagnetic waves.

Polarizability

A polarizability change, or amount of electron cloud deformation, with respect to the periodic displacement of lattice atoms u (see Fig. 8.2 or Fig. 8.3) is required to observe the Raman effect. The amount of the polarizability change will determine

the Raman scattering intensity, whereas the Raman shift is equal to the vibrational mode that is involved.

The dielectric response varies slightly across the lattice as a result of the electron cloud deformation. The homogeneous form of the dielectric response can thus be expanded into a Taylor series in u. This yields an approximation of the polarizability

$$\alpha(\omega, u) = \lim_{n\to\infty} \left\{ \varepsilon(\omega) + \left(\frac{d\varepsilon}{du}\right) u + \frac{1}{2}\left(\frac{d^2\varepsilon}{du^2}\right) u^2 + ... + \frac{1}{2}\left(\frac{d^n\varepsilon}{du^n}\right) u^n \right\}. \tag{8.5}$$

The dipole moment induced by the polarizability is

$$\vec{P} = \lim_{n\to\infty} \left\{ \varepsilon(\omega) + \left(\frac{d\varepsilon}{du}\right) u + \frac{1}{2}\left(\frac{d^2\varepsilon}{du^2}\right) u^2 + ... + \frac{1}{2}\left(\frac{d^n\varepsilon}{du^n}\right) u^n \right\} \vec{E} \tag{8.6}$$

at a fixed point in space, the phonon modes will obey

$$u = u_0 \cdot \cos(\Omega t), \tag{8.7}$$

where Ω is the angular frequency of the phonons as opposed to ω of the photons. The incident electric fields defined in eq. (8.2) may also be written in a similar form

$$E_{in} = E_0 \cdot \cos(\omega t). \tag{8.8}$$

The expression for the dipole moment in eq . (8.6) hence contains terms of form

$$\cos(\Omega t)^n \cdot \cos(\omega t) = \cos([\omega \pm n\Omega] \cdot t). \tag{8.9}$$

The amplitude of the outgoing wave which is radiated by the dipole is

$$\vec{E}_{out} \propto |\vec{P}| \propto \{\cos([\omega \pm \Omega] \cdot t) + \cos([\omega \pm 2\Omega] \cdot t) + ...\}. \tag{8.10}$$

Raman Scattering

The outgoing wave therefore contains photons with angular frequency $\omega_{out} = \omega \pm n\Omega$ where n is an integer (including zero). This means that the energy of those outgoing photons is shifted up or down in quanta of the phonon energy

$$\epsilon_{out} = \hbar\omega_{out} = \hbar\omega_{in} \pm n \cdot \hbar\Omega. \tag{8.11}$$

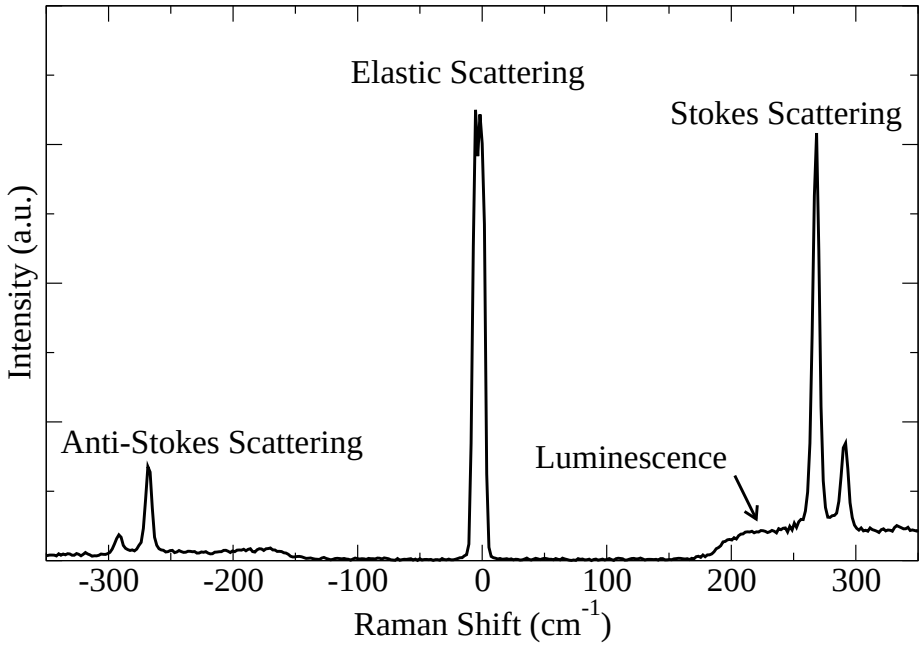

Figure 8.4. Raman spectrum of gallium arsenide (GaAs) showing inelastic Stokes and Anti-Stokes scattering as well as elastic scattering. Also shown is luminescence which cannot be avoided in measurements. The peak labeled 'Elasic Scattering' should be several orders of magnitude higher than the other peaks. The detector is not sensitive to low wavenumbers, thus decreasing the peak height.

In the process described above, light was therefore scattered inelastically by the lattice of a semiconductor. The first order energy shifts (n=1) are called Stokes-Raman scattering ($\omega - \Omega$) and Anti-Stokes-Raman scattering ($\omega + \Omega$). The inelastic scattering process becomes less likely with increasing order due to the u^n dependence in eq. (8.6). It is also possible that the energy of photons remains unchanged. The zeroth order energy shift (n=0) is simply the well known elastic scattering of light. Fig. 8.4 shows the measured shifts up to the first order for GaAs. The relative strength of the Stokes and Anti-Stokes lines depends on the ambient temperature and the angular frequency of the resonant phonons [116]. The Stokes line is always stronger at room temperature which was confirmed for my measurement in Fig. 8.4.

Intensity

The intensity of the first order Stokes and Anti-Stokes Scattering is very weak compared to elastic scattering [116]

$$I \propto \omega^4 \left(\frac{d\epsilon(\omega)}{du} \right)^2 \langle u^2 \rangle \propto \frac{1}{\lambda^4}, \tag{8.12}$$

where $\langle u^2 \rangle$ is the thermal average of the atomic displacement. The intensity scales with the inverse wavelength to the fourth power which is the reason why Raman spectroscopy is often carried out at the 514 nm laser line. Green light at this wavelength produces a Raman peak that is about 2.3 times more intense than that from the red light at the He-Ne line 633 nm. The intensity vanishes if the derivative vanishes. The photon frequency ω and the average displacement $\langle u^2 \rangle$ are finite. Thus, a phonon mode is Raman active only if

$$\frac{d\varepsilon}{du} \neq 0. \tag{8.13}$$

A full calculation of the Raman intensity and line shape is as arduous as complex for a specific semiconductor and can hardly be found in the literature. However, the observed intensity scales with the following bilinear form

$$I \propto \left| \hat{p}_i \cdot \mathbb{R} \cdot \hat{p}_s \right|^2, \tag{8.14}$$

where $\hat{p}_i$ is the normal vector of the incident ray's polarization, $\hat{p}_s$ is the polarization of the scattered electric field. $\mathbb{R}$ is the Raman tensor containing geometric information and thus the selection rules for the crystal symmetry. In the backscattering geometry employed in this study, both incident and scattered ray are along an arbitrary z-axis and opposite in sign. The incident electric field propagates in the z-direction and I define its polarization as

$$\hat{p}_{in} = \hat{x}. \tag{8.15}$$

The polarization of the longitudinal (LO) phonon mode is then

$$\hat{p}_{s,LO} = \hat{z} \tag{8.16}$$

and the polarization of the transverse (TO) phonon mode is

$$\hat{p}_{s,TO} = (\alpha\hat{x} + \beta\hat{y}) \qquad \alpha, \beta \epsilon \mathbb{R}. \tag{8.17}$$

A Zincblende structure, such as GaAs, has the following Raman tensor for backscattering on a (001) surface [122]

$$\mathbb{R} = \begin{pmatrix} 0 & 0 & 1 \\ 0 & 0 & 0 \\ 1 & 0 & 0 \end{pmatrix}. \tag{8.18}$$

The selection rules predicts that only LO phonons are Raman active in this geometry. Using the appropriate Raman tensor tabulated by Loudon [122], it is likewise found that only TO phonons contribute to the Raman effect on a (110) surface and both TO and LO phonons may be observed after scattering on a (111) surface which is shown in Fig. 8.1. These rules apply for ideal crystalline GaAs, but break down for disordered or polycrystalline structures. Raman scattering can thus be used to judge the crystalline quality if the orientation is known or measure the crystal orientation if the sample is sufficiently cystalline. Moreover, the breakdown of a selection rule due to disorder results in a broadening of the observed peaks. The line width of a Raman peak can therefore be used as a qualitatively measure of the lattice disorder.

8.3 Apparatus

The measurements were taken at the Saskatchewan Structural Sciences Centre (SSSC) at the U of S; their apparatus may be used for a fee after training. The main component is a Renishaw 2000 Raman microscope in backscattering geometry with a 1800 lines/mm grating. A 50× objective was used to illuminate a spot of less than 10 μm on the surface of the samples. The incident beam was supplied by a Melles Griot Argon-ion laser model 35-Lap-431-208 which was tuned to a wavelength of 514 nm for all measurements. The penetration depth of light at this wavelength is about 100 nm for GaAs [116]. The optical output power was set to 20 mW and not lessened by the software. Galactic Grams/32C version 4.14 Level 2 together

with Renishaw Wire were used to capture the spectra which have an accuracy of approximately 2 cm^{-1}. All spectra were recorded in the 'Cosmic Ray Removal' mode which analyzes multiple spectra to find sharp intense peaks from cosmic radiation and removes those. The final spectra were compiled by the software from 20 accumulations of 20 s exposure each. A reference spectra without a sample was taken to remove the background. Raman spectroscopy is susceptible to luminescence and the measurements were therefore carried out in the dark with the microscope lid closed.

8.4 Results and Discussion

The samples discussed in this section were implanted with nitrogen in the 'Transformer Mode' at 10 kV. A total fluence of 5×10^{16} ions/cm^2 hit the surface of the sample. Raman spectroscopy may yield insights to the following points which were discussed in Chapter 7:

- Ga-As bonds
- Ga-N bonds
- Molecular Nitrogen

The positions of all peaks due to phonons that can be detected are collected in Table 8.1. GaN-like bonds could be formed in either Zincblende or Wurtzite structure which is why phonon modes on both lattice structures were added. The Wurtzite structures allows more modes to propagate than the LO and TO phonons which is discussed in the references [116, 121, 120]. The results of my measurements are discussed in the subsequent paragraphs.

Ga-As Bonds

The region of interest for phonons due to the Ga-As bond is shown in Fig. 8.5. The GaAs reference sample clearly shows the the longitudinal optical (LO) and transverse optical (TO) mode of GaAs at 268 cm^{-1} and 291 cm^{-1}, respectively. The fact that

Table 8.1. Raman active modes which could be found in nitrogen-ion implanted gallium arsenide. The notation N means localized mode due to N_{As} substitution of an As lattice site. (z) indicates the Zincblende crystal structure and (w) the Wurtzite structure.

Mode	Wavenumber (cm^{-1})	Found	Ref
GaAs TO (z)	269	yes	[116]
GaAs LO (z)	291	yes	[116]
GaN TO (z)	552, 555	no	[4]
GaN LO (z)	739, 741	no	[4]
GaN TO A_1(w)	534	no	[4]
GaN TO E_1 (w)	556	no	[4]
GaN LO A_1(w)	735	no	[4]
GaN LO E_1(w)	743	no	[4]
N_{As}	473	no	[126]
N_2	2330	no*	[127]

*belonged to the background

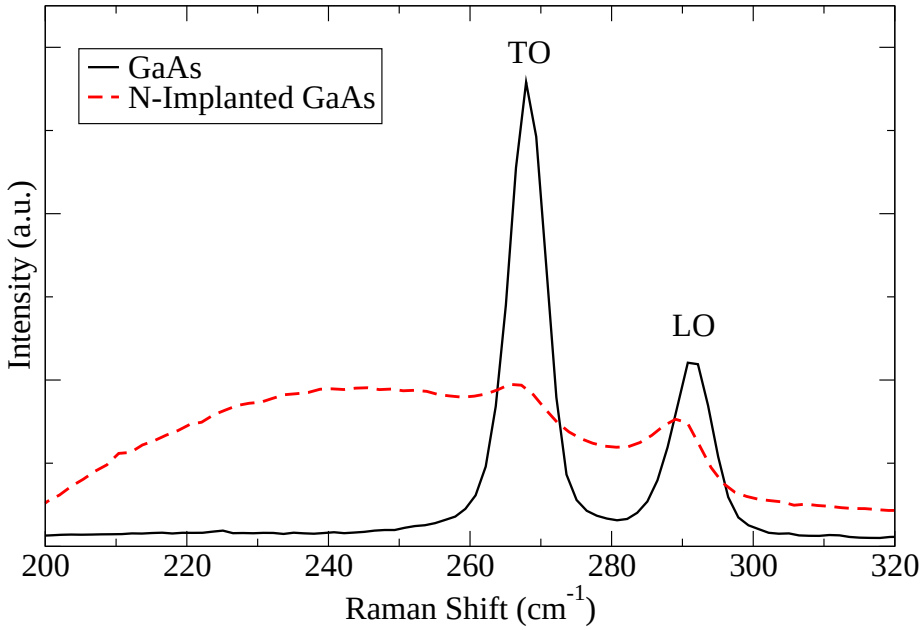

Figure 8.5. Raman Spectrum of nitrogen implanted gallium arsenide(GaAs) and unimplanted GaAs as a reference. All the peaks of the implanted spectrum are shifted to lower wavnumbers. Moreover, disorder induced broadening is visible below 260 cm^{-1}.

both are visible means that either the sample has a (111) surface or is polycrystalline. The latter is more likely since the manufacturer did not specify the orientation of the samples and a cut along (111) is an elaborate process. The peaks of the GaAs reference sample are also rather wide which seconds that structural disorder is already present in the reference sample. The peak labeled TO could also be due to plasmons of a dopant [128]. However, this is highly unlikely since the plasmon peak is only visible for high carrier concentrations which should not be expected from an undoped sample.

The phonon modes of N-implanted GaAs are shifted to lower wavenumbers of 266 cm^{-1} (TO) and 289 cm^{-1} (LO). The peak heights, especially of the TO mode, decreased significantly. A broad new feature appeared below 260 cm^{-1}. All those features are signs of the disorder caused by the implanted nitrogen ions. Strain of the lattice or a change in the bonding environment could cause the shift of the peaks.

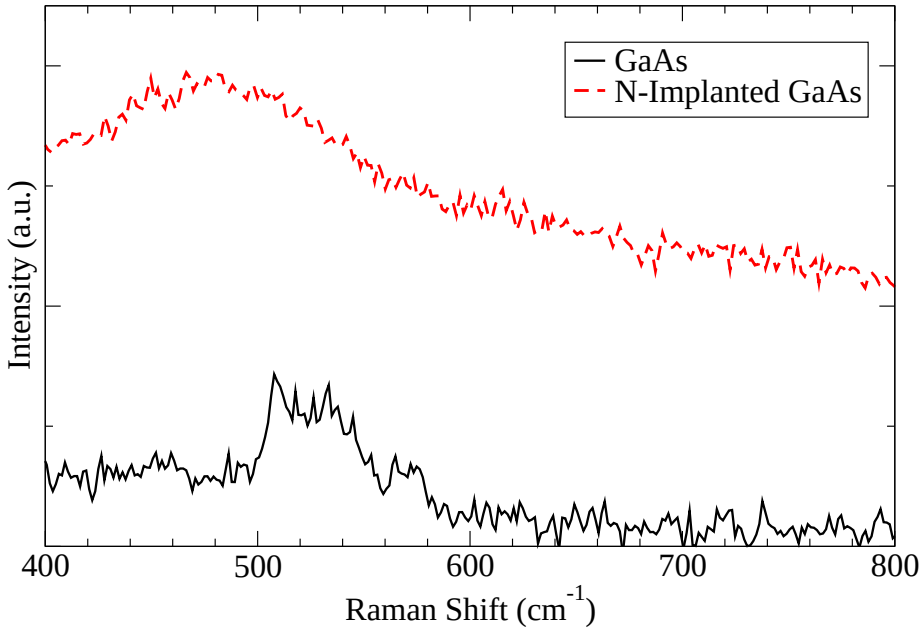

Figure 8.6. Raman Spectra of gallium arsenide (GaAs) and nitrogen-implanted GaAs. Shown is the region of wavnumbers for which Ga-N bonds would be expected. No evidence for those bonds was found. The peaks are due to second order Raman scattering of GaAs phonons.

Ga-N Bonds

The region of interest for phonons due to the Ga-N bond is shown in Fig. 8.6. The GaAs reference sample shows a broad second order GaAs TO peak at 523 cm^{-1} ($\approx 2 \times 268$ cm^{-1}) and an even fainter second order peak of the LO mode of GaAs at 571 cm^{-1} ($\approx 2 \times 291$ cm^{-1}).

The N-implanted sample shows a very broad feature centered at about 480 cm^{-1} which should be assigned to a second order GaAs phonon mode. Again, the broadening is caused by lattice disorder. No clear evidence was found for any of the phonons due to the Ga-N bonds in Table 8.1. The number of Ga-N bonds formed after nitrogen-ion implantation is thus negligible, i.e. below the detection limit of the apparatus. It is also questionable whether GaN-like phonons can travel across the highly disordered GaAs host matrix.

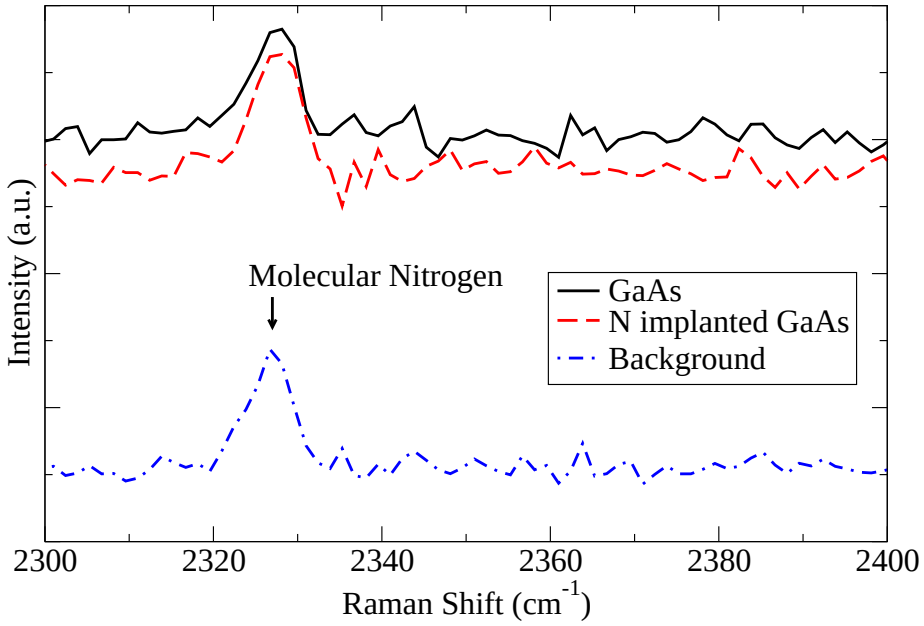

Figure 8.7. Raman spectra showing signals due to molecular nitrogen. The background was not removed from the shown spectra because it serves as the reference. The nitrogen signal is not stronger than in the background.

Molecular Nitrogen

The last question that arose in the last chapter is whether molecular nitrogen exists in voids within the implanted target. The vibration probed in these spectra are not due to waves on a lattice, but rather vibrations of the molecule. The principle idea that photons can loose or gain energy from scattering interaction with a construct of atoms is still valid. Herzberg [124] gives the proper derivations and a discussion of Raman spectroscopy of molecules.

The spectra are shown in Fig. 8.7. The peak due to molecular nitrogen was found at 2,326 cm^{-1} in all three spectra. Also, the peak height relative to the noise level is the same. The signal is therefore due to the nitrogen molecules in the air. No increase of the signal due to nitrogen molecules buried in within the implanted GaAs sample were detected.

Chapter 9

Conclusion

The motivation for the work presented in this document is discussed in Chapter 1. GaAsN is a candidate for future generations of on-chip lasers for telecommunication applications. The methods developed during my work could ultimately yield cost-effective synthesis and processing of GaAsN alloys from the cheap precursor gallium arsenide (GaAs).

An introduction to Plasma Ion Implantation (PII) was given in Chapter 2. The overview included the definition of PII, instrumentation, history and a discussion of the advantages and limitations of the technique. The second section of the chapter was concerned with the properties of different sheath types. The basic equations governing the sheaths dynamics were derived. Lastly, the interaction between secondary electrons and the plasma was explained.

Chapter 3 provides an overview on the components of the plasma processing setup at the Plasma Physics Laboratory (PPL) at the University of Saskatchewan (U of S). The focus was set on a thoroughly documentation of the various devices and practical information for maintenance. Two modes for the operation of the pulser were identified: the 'Transformer Mode' (TM) and the 'Marx Mode' (MM).

9.1 Measurements

The measurements needed by the methods developed in the course of my work are discussed in Chapter 4. The mass and dimensions of the GaAs samples was determined to calculate the atomic density of $n_{GaAs} = 1.96 \times 10^{22}$ cm^{-1} which is about 11% lower than the literature value of 2.2×10^{22} cm^{-1} [6]. Langmuir probe measure-

ments yielded an electron temperature of 4.34 eV and a plasma potential of 19.5 eV which both agree well with reports of other groups or previous work at the PPL. The four measurements of the plasma bulk density diverged a lot and the decision was made to use the value of $n_0 = 1.2 \times 10^{16}$ ions/m^3. The latter value agreed best with other reports in the literature and yielded the best agreement between measured and predicted ion currents.

9.2 PII Predictions

Chapter 5 deals with the prediction of the plasma ion current from the analytic Lieberman model. A review of the assumptions may be found in the Appendix C.1. The implementation of the model was discussed in great detail. The model contains various extensions to the original Lieberman model and error boundaries due to the experimental errors of the inputs were given for the first time. The sheath, current and fluence predictions were presented for 3 voltage pulses: -1 kV (MM), -1 kV (TM) and the -10 kV (TM) pulse which yields reasonable implantation depths. Both, -1 kV (MM) and -10 kV (TM) agree well to the measured variables within the error boundaries, but the -1 kV (TM) predictions are poor if the same set of input parameters is used for all pulses. It was found that the fluence scales with $n_0^p V_0^{1/2}$ where the exponent p depends on the plasma enhancement. Even with the enhancement turned off, the exponent calculated from my predictions are lower than previously derived by Tian and Chu [70]. The chapter was concluded by the results for the predicted energy distributions of the ions in the plasma and at the instant of impinging on the surface. None of the voltage pulses that can currently be produced at the PPL have satisfactory distributions.

9.3 Materials Aspects

The GaAsN alloy is the topic of Chapter 6. The research done previously by ion beam implantation is reviewed. The subsequent discussions of the alloy's structure and

electronic properties complement the overview. Models for the band gap as a function of the nitrogen (N) content in the GaAsN alloy are explained. The conductivity of the material can be estimated from the Band Anti-Crossing (BAC) model [108]. N incorporation was found to lower the conductivity of GaAsN. The concentration dependent band bowing model [106] showed convincing agreement with the first principles predictions of Bellaiche et al. [104] and were thus selected for my novel plots of the spatial variation of the band gap in N ion-implanted GaAs.

9.4 Depth Profiles

The depth profiles are discussed in Chapter 7. An introduction to the physics of ion stopping is provided and two Monte Carlo simulations for the output of depth profiles are commented on. A new method for the estimation of the change in the band gap upon ion implantation was presented for the assumption of mono-energetic ions in a nitrogen plasma with three ion species. It was pointed out that the total fluences of subsequent implants at various ion energies can be adjusted to tailor a trapezoidal depth profile. A region of nearly constant band gap is predicted for these depth profiles, hence making them suitable for device applications. The simplifications used in this model were discussed in the following. It was found that nitrogen ion implantation at the total fluences predicted for the spatially constant band gap causes gallium (Ga) atoms to pile up on the sample's surface whereas arsenic (As) and previously implanted N is preferably sputtered. Sputtering was also found to limit the maximal dose retained in the material for fluences an order of magnitude higher than necessary for the anticipated concentration. It was argued that the GaAsN alloy cannot form directly after ion implantation because the ratios of the elements Ga, As and N differ from the one expected for the alloy. All reports of the alloy's formation by ion (beam) implantation mention some form of annealing procedure to activate the implanted material. Annealing was discussed and the conclusion was drawn that it is a necessary step which cannot be carried out with the equipment at the PPL due to missing infrastructure for the handling of toxic gases released during

the annealing process.

9.5 Raman Characterization

The characterization of preliminary manufactured samples was discussed in Chapter 8. The apparatus as well as experimental settings were described. The Raman effect was explained and the observable shift due to inelastic scattering of light was derived. None of the anticipated signals indicating the formation of new bonds were found. Instead, the only effect of the implanted ions was an increase of the lattice disorder. In addition, no molecular nitrogen could be detected in the implanted samples.

9.6 Conferences and Publications

I presented the outline of my project at the 2007 CAP Congress in Saskatoon [129] and the method of the conversion of a depth profile into a spatial variation of the band gap at the 9th International Workshop on Plasma Based Ion Implantation and Deposition (PBIID) [93] also in 2007. My contribution to the proceedings have been published in pss c [94]. An overview of the preliminary optimal parameters for band gap engineering of GaAsN by means of PII will be presented in July 2008 at the 3rd International Conference on Optical, Optoelectronic and Photonic Materials and Applications (ICOOPMA) in Edmonton.

9.7 Future Work

9.7.1 Plasma Processing and Diagnosis

It was pointed out at various points that a Faraday cup is a versatile tool for PII diagnostics which can measure the ion current directly and also yield the in-situ fluence and ion energy distribution. The Faraday cup unit is designed and assembled. I expect testing to start in the near future. The data will help to improve the set of

input parameters to the p2i software as the direct measurement of the ion current supersedes the calculation of the true ion current from the measured total current which inherently contains the secondary electron emission. The operation of the Faraday cup will allow us to study the plasma enhancement effect which is the project of Phillip Desautels. His results could remove the necessity of fitting the predicted and measured currents with the enhancement factor.

The design of Marx stages is currently under review and plans exist to increase the number of installed modules. The circumvention of the transformer will yield much narrower distributed ion energies, thus offering the opportunity to tailor the desired trapezoidal profiles. Moreover, a pulse-counting controller system has been developed by Kurt Kreuger during his summer research position in the summer of 2007. Once installed, it will allow for very precise selection of the dose applied to the target.

9.7.2 Annealing

The crucial role of annealing for the formation of the GaAsN alloy by ion implantation was emphasized multiple times in this document. I will investigate whether it is possible to upgrade the existing annealing setup to treat potentially toxic volatile substrates, such as GaAs. The Chemistry Department at the U of S might also offer some help in modifying the setup at the PPL. It is also possible, that someone on campus has a suitable setup and is willing to collaborate by annealing the implanted samples. The annealing could also be done externally as a last resort. The other options are preferable since a larger number of samples must be processed to find the optimal annealing temperature and duration. Meanwhile, it will be very beneficial to become familiar with simulations of the diffusion during annealing to maintain the possibility of designing a depth profile and also to decrease the number of test samples in the task of finding the optimal conditions for alloying N and GaAs.

9.7.3 Further Measurements

The predicted N depth profiles must be measured to verify the method. The relative depth profile can be obtained from Secondary Ion Mass Spectroscopy (SIMS) in which ions mill the surface and the released ions are analyzed by mass spectroscopy. The technique is not yet available at the U of S, but we received an offer to measure some of our samples at the Forschungszentrum Rossendorf-Dresden. This should be done right after the challenge of annealing is solved.

9.7.4 Continuing Research

The experience gained with the work on the GaAsN alloy could be used to investigate the similar alloy of GaInAsN. The introduction of indium (In) gives the freedom to adjust the band gap and the lattice parameter within limits. A thin film of In could be added on the surface of a GaAsN sample and with a technique called ion mixing, some of the In atoms in the film would be pushed into the GaAsN. The result after removal of the surface and further annealing would be GaInAsN synthesized from GaAs by ion implantation in general and PII in specific, which has not yet been demonstrated. Preliminary calculations of the feasibility will be part of my legacy to the next generation of students in PII at the PPL.

References

[1] B. Brecht, R. Grimm, and C. Vedia, *Berthold Brecht: Poetry and Prose*. Continuum International Publishing Group, 2003.

[2] R.R. Schaller, "Moore's law: past, present and future," *IEEE Spectrum*, vol. 34, no. 6, p. 52, 1997.

[3] Ch. Kittel, *Introduction to Solid State Physics*. 7th ed., 1996.

[4] S. Nakamura and S.F. Chichibu, eds., *Introduction to Nitride Semiconductor Blue Lasers and Light Emitting Diodes*. Taylor and Francis, 2000.

[5] Landolt-Börnstein, Springer.

[6] Sadao Adachi, *GaAs and Related Materials*. World Scientific, 1994.

[7] I.Vurgaftman, J.R. Meyer, and L.R. Ram-Mohan, "Band parameters for III-IV semiconductors and their alloys," *J. Appl. Phys.*, vol. 89, no. 11, p. 5815, 2001.

[8] M. Risch, "Silicon Carbide Synthesized by Plasma Immersion Ion Implantation for Electroluminescent Device Applications." B.Sc. Thesis, Technische Universität Darmstadt, June 2006.

[9] F.F. Chen, *Introduction to Plasma Physics and Fusion*. Plenum Press, 2nd ed., 1984.

[10] A. Anders, ed., *Handbook of Plasma Immersion Ion Implantation*. Wiley and Sons, 1st ed., 2000.

[11] M. Risch and M. Bradley, "Electroluminescence of Carbon-Implanted Silicon," *49th Annual Meeting of the Division of Plasma Physics*, Nov. 2007.

[12] I. Alexeff, W.D. Jones, K. Lonngren, and D. Montgomery, "Transient Plasma Sheath - Discovered by Ion-Acoustic Waves," *Phys. Fluids*, vol. 12, p. 345, 1969.

[13] M. Widner, I. Alexeff, W.D. Jones, and K.E. Lonngren, "Ion Acoustic wave excitation and ion sheath evolution," *Phys. Fluids*, vol. 13, no. 10, p. 2532, 1970.

[14] R.J. Adler and S.T. Picraux, "Repetitively pulsed metal ion beams for ion implantation," *Nucl. Instrum. Methods B*, vol. 6, p. 123, 1985.

[15] J.R. Conrad and C. Forest, "Plasma source ion implantation," *IEEE International Conference on Plasma Science, Sasaktoon, Canada*, 1986.

[16] J.R. Conrad and T. Castagna, "Plasma source ion implantation for surface modification," *Bull. Am. Phys. Soc.*, vol. 31, p. 1479, 1986.

[17] B. Mizuno, I. Nakayama, N. Aoi, M. Kubota, and T. Komeda, "New doping method for subhalf micron trench sidewalls by using an electron cyclotron resonance plasma," *Appl. Phys. Lett.*, vol. 53, p. 2059, 1988.

[18] S. Qin, Y.Z. Zhou, C. Chan, and P.K. Chu, "Fabrication of low dielectric constant materials for ULSI multilevel interconnection by plasma immersion ion implantation," *IEEE Electron. Device Lett.*, vol. 19, p. 420, 1998.

[19] J.N.A. Matthews, "Semiconductor industry switches to haffnium-based transistors," *Physics Today*, vol. 61, no. 2, p. 25, 2008.

[20] E. Goldstein, "Über eine noch nicht untersuchte Strahlungsform an der Kathode inducierter Entladungen," *Sitzungsberichte der Königlichen Akademie der Wissenschaften zu Berlin*, vol. 39, p. 691, 1886.

[21] A. Anders, "From plasma immersion ion implantation to deposition: a historical perspective on principles and trends," *Surface and Coatings Technology*, vol. 156, p. 3, 2003.

[22] J. Pelletier and A. Anders, "Plasma-Based Ion Implantation and Deposition: A Review of Physics, Technology, and Applications," *IEEE Transact. on Plasma Sci.*, vol. 33, no. 6, p. 1944, 2005.

[23] P.K. Chu, "Semiconductor applications of plasma immersion ion implantation," *Plasma Phys. Control Fusion*, vol. 45, p. 555, 2003.

[24] W. Ensinger, "Semiconductor Processing by Plasma Immersion Ion Implantation," *Mat. Sci. En.*, vol. 253, p. 258, 1998.

[25] W. Möller and S. Nukherjee, "Plasma-based ion implantation," *Current Science*, vol. 83, no. 3, p. 237, 2002.

[26] M.A. Lieberman and A.J. Lichtenberg, *Principles of Plasma Discharges and Materials Processing.* Wiley and Sons, 2nd ed., 2005.

[27] D. Bohm, *The Characteristics of Electrical Discharges in Magnetic Fields.* MacGraw-Hill, 1949.

[28] K.U. Riemann, "The Bohm Criterion and sheath formation," *J. Phys. D: Appl. Phys.*, vol. 24, p. 493, 1991.

[29] K.U. Riemann, "The validity of Bohm's sheath criterion in RF discharges," *Phys. Fluid. B*, vol. 4, no. 9, p. 2693, 1992.

[30] C.D. Child, "Discharge from hot Cao," *Phys. Rev. (Series I)*, vol. 32, p. 492, 1911.

[31] J.T. Steenkamp, "High Power Solid State Modulator for Plasma Ion Implantation," Master's thesis, University of Saskatchewan, Oct. 2006.

[32] W. En and N.W. Cheung, "A new method for determining the secondary electron yield dependence on ion energy for plasma exposed surfaces," *Transact. on Plasma Sci.*, vol. 24, no. 3, p. 1184, 1996.

[33] B. Szapiro, J.J. Rocca, and T. Prabhuram, "Electron yeild of glow discharge cathode materials under helium ion bombardment," vol. 53, p. 358, 1988.

[34] M.M. Shamin, J.T. Scheuer, R.P. Fetherston, and J.R. Conrad, "Measurement of electron emission due to energetic ion baombardment in plasma source ion implantation," *J. Appl. Phys.*, vol. 70, p. 4756, 1991.

[35] B.P. Cluggish and C.P. Munson, "Secondary electron enhanced discharges in plasma source ion implantation," *J. Appl. Phys.*, vol. 84, p. 5945, 1998.

[36] P.L. Kellerman, J.D. Bernstein, and M.P. Bradley, "Ion Energy Distributions in Plasma Immersion Ion Implantation- Theory and Experiment," *Proceedings of the International Conference on Ion Implantation Technology 2000*, p. 484, 2000.

[37] S. Qin, M.P. Bradley, and P.L. Kellerman, "Measurements of secondary electron emission and plasma density enhancement for plasma exposed surfaces using an optically isolated Faraday cup," *Review of Scientific Instruments*, vol. 73, no. 3, p. 1153, 2002.

[38] M. Bradley, "Fundamental Plasma Phenomena and Delivered Ion Dose in PBII," *Invited Talk at the 9th International Workshop of Plasma-Based Ion Implantation and Deposition*, no. I-2-1, p. 46, 2008.

[39] C. J. T. Steenkamp and M. P. Bradley, "Active Charge/Discharge IGBT Modulator for Marx Generator and Plasma Applications," *IEEE Transactions on Plasma Science*, vol. 35, no. 2, p. 473, 2007.

[40] C.J.T. Steenkamp, *Bradley Group -20 kV Pulse Generator User and Maintenance Manual*. Plasma Physics Laboratory, University of Saskatchewan, Saskatoon, 1st ed., 2006.

[41] Hong Li, "Measurements of electron energy distribution function and neutral gas temperature in an inductively coupled plasma," Master's thesis, University of Saskatchewan, 2006.

[42] M. Tuszwwski and J.A. Tobin, "The accuracy of Langmuir probe ion density measurements in low-frequency RF discharges," *Plasma Sources Sci. Technol.*, vol. 5, p. 640, 1996.

[43] G.H. Kim, G.H. Rim, and S.A. Nikiforov, "Monitoring of ion mass composition in plasma immersion ion implantation," *Surf. Coat. Tech.*, vol. 136, p. 255, 2001.

[44] G.A. Emmert, "Model for expanding sheaths and surface charging at dielectric surfaces during plasma source ion implantation," *J. Vac. Sci. Technol. B*, vol. 12, p. 880, 1994.

[45] B.P. Linder and N.W. Cheung, "Plasma Immersion Ion Implantation with dielectric substrates," *IEEE Trans. Plasma Sci.*, vol. 24, p. 1383, 1996.

[46] Z.L. Dai and Y.N. Wang, "Dynamic sheath model at pulsed-biased insulating substrates," *J. Appl. Phys.*, vol. 92, no. 11, p. 6428, 2002.

[47] X. Tian and P.K. Chu, "Direct temperature monitoring for semiconductors in plasma immersion ion implantation," *Rev. Sci. Instr.*, vol. 71, no. 7, p. 2839, 2000.

[48] J.P. Blanchard, "Temperature Prediction for Plasma Source Ion Implantation," *J. Vac. Sci. B*, vol. 12, no. 2, p. 910, 1994.

[49] S.M. Sze, *Semiconductor Sensors*. Wiley and Sons, 1994.

[50] I.H. Hutchinson, *Principles of Plasma Diagnostics*. Cambridge University Press, 2nd ed., 2002.

[51] F.F. Chen, "Numerical Computations for ion probe characteristics in a collisionless plasma," *J. Nucl. Energy, Part C Plasma Phys.*, vol. 7, p. 47, 1965.

[52] F.F. Chen, "Langmuir Probe analysis for high density plasmas," *Phys. Plasmas*, vol. 8, no. 6, p. 3029, 2001.

[53] H.M. Mott-Smith and I. Langmuir, "The theory of collectors in gaseous discharges," *Phys. Rev.*, vol. 28, p. 727, 1926.

[54] L.S. Pilling and D.A. Carnegie, "Validating experimental and theoretical Langmuir probe analyses," *Plasma Sources Sci. Technol.*, vol. 16, p. 570, 2007.

[55] N. Hershkowitz, M.H. Cho, C.H. Nam, and T. Intrator, "Langmuir Probe Characteristics in RF Glow Discharges," vol. 8, no. 1, p. 35, 1988.

[56] V.A. Godyak and R.B. Piejak, "Abnormally low electron energy and heating-mode transition in a low-pressure argon rf discharge at 13.56 MHz," *Phys. Rev. Lett.*, vol. 65, p. 996, 1990.

[57] J.E. Allen, "Probe Theory - The Orbital Motion Approach," *Phys. Scr.*, vol. 45, pp. 497–503, 1992.

[58] J.E. Allen, R.L.F. Boyd, and P. Reynolds, "The Collection of Positive Ions by a Probe Immersed in a Plasma," *Proc. Phys. Soc. B*, vol. 70, pp. 297–304.

[59] T.I. Cox, V.G.I. Deshmukh, D.A.). Hope, A.J. Hydes, N. St.J. Braithwaite, and N.M.P Benjamin, "The use of Langmuir probes and optical emission spectroscpy to measure electron energy distribution functions in RF generated argon plasmas," *J. Phys D*, vol. 20, pp. 820–831, 1987.

[60] M.A. Lieberman, "Model of plasma immersion ion implantation," *J. Appl. Phys.*, vol. 66, no. 7, p. 2926, 1989.

[61] R.A. Stewart and M.A. Lieberman, "Model of plasma immersion ion implantation for voltage pulses with finite rise and fall times," *J. Appl. Phys.*, vol. 70, no. 7, p. 3481, 1991.

[62] W.G. En, M.A. Lieberman, and N.W. Cheung, "Comparision of experimental target currents with analytical model results for plasma immerison ion implantation," *IEEE Transact. Plasma Sci.*, vol. 23, no. 3, p. 415, 1995.

[63] G.A. Emmert and M.A. Henry, "Numerical simulation of plasma sheath expansion, with applications to plasma-source ion implantation," *J. Appl. Phys.*, vol. 71, no. 1, p. 113, 1992.

[64] B. Briehl and H.M. Urbassek, "Simulation of Plasma Sheath and Presheath Dynamics in PIII," *Sur. Coat. Technol.*, vol. 156, no. 1-3, p. 131, 2002.

[65] D.T. Kwok, X. Liu, and P.K. Chu, "Introduction to multiple-grid-pic method and its application to plasma immersion ion implantation of NiTi Rod," *Invited Talk at the 9th International Workshop of Plasma-Based Ion Implantation and Deposition*, no. I-5-1, p. 64, 2007.

[66] S. Qin, Z. Jin, and Ch. Chan, "Dynamic sheath model of collisionless multispecies plasma immerison ion implantation," *J. Appl. Phys.*, vol. 78, no. 1, p. 55, 1995.

[67] Barry P. Linder, William G. En, and Nathan W. Cheung, "Multiple Species implants with pulsed and DC plasma immersion ion implantation," *Ion Implantation Technology Proceedings, 1998 International Conference on*, vol. 2, pp. 1179–1182, 1999.

[68] P.L. Kellerman, S. Qin, and M.P. Bradley, "Ion depletion effects in sheath dynamics during plasma immersion ion implantation - models and data," *Review of scientific instruments*, vol. 73, no. 2, p. 837, 2002.

[69] J.J. Barrosso, J.O. Rossi, and M. Ueda, "Modeling Plasma Immersion Ion Implantation under Trapezoidal Voltage Pulses," *IEEE Transact. Plasma Sci.*, vol. 31, no. 1, p. 104, 2003.

[70] X. Tian and P.K. Chu, "Modeling of the relationship between implantation parameters and implantation dose during plasma immersion ion implantation," *Physics Letters A*, vol. 277, pp. 42–46, 2000.

[71] S. Qin, M.P. Bradley, and P.L. Kellerman, "Farady Dosimetry Characteristics of PII Doping Processes," *IEEE Transact. Plasma Sci.*, vol. 31, p. 369, 2003.

[72] X.B. Tian, D.T.K. Kwok, and P.K. Chu, "Modeling of incident particle energy distribution in plasma immersion ion implantation," *J. Appl. Phys.*, vol. 88, no. 9, p. 4961, 200.

[73] S. Mändel, J. Brutscher, R. Günzel, and W. Möller, "Ion Energy Distribution in Plasma Immersion Ion Implantation," *Surf. Coat. Technol.*, vol. 93, p. 234, 1997.

[74] I. Vurgaftman and J.R. Meyer, "Band parameters for nitrogen-containing semiconductors," *J. Appl. Phys*, vol. 94, no. 6, p. 3675, 2003.

[75] J. Toivonen, *Growth and properties of GaAsN structures.* PhD thesis, Helsinki University of Technology, 16 May 2003.

[76] V.M. Goldschmidt, "Crystal structure and chemical constitution," *Trans Faraday Soc.*, vol. 25, p. 253, 1929.

[77] A.H. Kachare, W.G. Spitzer, K. Kahan, F.K. Euler, and T.A. Whatley, "Ion-implanted nitrogen in gallium arsenide," *J. Appl. Phys.*, vol. 44, no. 10, p. 4393, 1973.

[78] M. Weyers, M. Sato, and H. Ando, "Red Shift of photoluminescence and absorption in dilute GaAsN alloy layers," *Jpn. J. Appl. Phys.*, vol. 31, p. L853, 1992.

[79] T. Shima, S. Kimura, T. Iida, A. Obera, Y. Makita, K. Kudo, and K. Tanaka, "High concentration nitrogen ion doping into GaAs for the fabrication of GaAsN," *Nucl. Instr. Meth. Phys. Res. B*, vol. 118, p. 743, 1996.

[80] W. Shan, W. Walukiewicz, K.M. Yu, J.W. Ager, E.E. Haller, J.F. Geisz, D.J. Friedman, J.M. Olson, and S.R. Kurtz, "Effect of nitrogen on the electronic band structure of group III-N-V alloys," *Phys. Rev. B*, vol. 62, no. 7, p. 4211, 2000.

[81] K.M. Yu, W. Walukiewicz, W. Shan, J. Wu, J. Beeman, J.W. Ager, E.E. Haller, and M.C. Ridgeway, "Mutual Passivation in Dilute GaNAs alloys," *Mater. Res. Soc. Symp. Proc.*, vol. 647, 2001.

[82] K.M. Yu, W. Walukiewicz, J. Wu, J.W. Beeman, J.W. Ager, E.E. Haller, W. Shan, H.P. Xin, and C.W. Tu, "Formation of diluted III-V nitride thin films by N ion implantation," *J. Appl. Phys.*, vol. 90, no. 5, p. 2227, 2001.

[83] K.M. Yu, W. Walukiewicz, and J.W. Beeman, "Enhanced nitrogen incorporation by pulsed laser annealing of GaAsN formed by N ion implantation," *Appl. Phys. Lett.*, vol. 80, no. 21, p. 3958, 2002.

[84] K.M. Yu, W. Walukiewicz, M.A. Scarpulla, O.D. Dubon, J. Wu, J. Jasinski, Z. Liliental-Weber, J.W. Beeman, M.R. Pillai, and M.J. Aziz, "Synthesis of GaAsN thin films by pulsed laser melting and rapid thermal annealing of N implanted GaAs," *J. Appl. Phys.*, vol. 94, no. 2, p. 1043, 2003.

[85] H.Ch. Alt, A.Y. Egorov, H. Richert, B. Wiedemann, J.D. Meyer, R.W. Michelmann, and K. Bethge, "Infrared absorption study of nitrogen in N-implanted GaAs and epitaxially grown GaAsN layers," *J. Appl. Phys.*, vol. 77, p. 3331, 2000.

[86] H.Ch. Alt, Y.V. Gomeniuk, G. Lenk, and B. Wiedemann, "GaAsN formation by implantation of nitrogen into GaAs studied by infrared spectroscopy," *Physica B*, vol. 340-342, p. 394, 2003.

[87] J. Miao and H.L. Hartnagel, "High-energy ion implantation: an alternative technology for micromatching three-dimensional GaAs structures," *Sensors and Actuators A*, vol. 114, p. 505, 2004.

[88] S. Sinning, T. Dekorsy, and M. Helm, "Ultrafast carrier dynamics in nitrogen-implanted GaAs," *IEE Proc. Optoelectron.*, vol. 151, no. 5, p. 361, 2004.

[89] M. Mikulics, M. Marso, S. Mantl, H. Lüth, and P. Kordos, "GaAs photodetectors prepared by high-energy and high-dose nitrogen implantation," *Appl. Phys. Lett.*, vol. 89, p. 091103, 2006.

[90] X. Weng, S.J. Clarke, W. Ye, S. Kumar, R.S. Goldman, A. Daniel, R. Clarke, J. Holt, J. Sipowska, A. Francis, and V. Rotberg, "Evolution of structural and optical properties of ion-beam synthesized GaAsN nanostructures," *J. Appl. Phys.*, vol. 92, no. 7, p. 4012, 2002.

[91] X. Weng, R.S. Goldman, V. Rotberg, N. Bataiev, and L.J. Brillson, "Origins of luminescence from nitrogen-ion-implanted epitaxial GaAs," *Appl. Phys. Lett.*, vol. 85, no. 14, p. 2774, 2004.

[92] X. Weng, W. Ye, R.S. Goldman, and J.C. Mabon, "Formation and blistering of GaAsN nanostructure layers," *J. Vac. Sci. Technol. B*, vol. 22, no. 3, p. 989, 2004.

[93] M. Risch and M. Bradley, "Nitrogen Ion Implantation into Gallium Arsenide for Band Gap Enginerring," *9th International Workshop of Plasma-Based Ion Implantation and Deposition*, no. O-4-1, p. 56, 2007.

[94] M. Risch and M. Bradley, "Predicted Depth Profiles for Nitrogen-Ion Implantation into Gallium Arsenide," *phys. stat. sol. (c)*, vol. 5, no. 4, p. 939, 2008.

[95] X.W. Lin, M. Behar, R. Maltez, W. Swinder, Z. Liliental-Weber, and J. Washburn, "Synthesis of GaN by N ion implantation in GaAs (001)," *Appl. Phys. Lett.*, vol. 67, no. 18, p. 2699, 1995.

[96] A.H.P. Ho, D.T.K. Kwok, X.C. Zeng, Ch. Chan, and P.K. Chu, "Preparation of gallium nitride (GaN) and related compounds by plasma immersion ion implantation and rapid thermal annealing," *Surf. Coat. Technol.*, vol. 136, p. 142, 2001.

[97] K.C. Lo, H.P. Ho, K.Y. Fu, and P.K. Chu, "Preparation of GaN thin film and GaO nanoribons by plasma immersion ion implantation of N into GaAs," *J. Appl. Phys.*, vol. 95, no. 12, p. 8178, 2004.

[98] S.O. Kasap, *Priciples of Electronic Materials and Devices.* 2nd ed., 2002.

[99] S. B. Zhang and Su-Huai Wei, "Nitrogen solubility and induced defect complexes in epitaxial GaAs:N," *Phys. Rev. Lett.*, vol. 86, p. 1789, 2001.

[100] C.F. Foxon, T.S. Cheng, S.V. Novikov, D.E. Lacklison, L.C. Jenkins, D. Johnston, J.W. Orton, S.E. Hooper, N. Aba-Ali, T.L. Tansley, and V.V. Tret'yakov, "The growth and properties of group III nitrides," *J. Cryst. Growth*, vol. 150, p. 892, 1995.

[101] Z.Z. Bandic, R.J. Hauenstein, M.L. O'Steen, and T.C. McGill, "Kinetic modelling of microscopic processes during electron cyclotron resonance microwave plasma-assisted molecular beam epitaxial growth of GaN/GaAs-based heterostructures," *Appl. Phys. Lett.*, vol. 68, no. 11, p. 1510, 1996.

[102] R.J. Hauenstein, D.A. Collins, X.P. Cai, M.L. O'Steen, Z.Z. Bandic, and T.C. McGill, "Anion Exchange Reactions and Initial GaN Epitaxial Layer Formation under Nitrogen Plasma Exposure of a GaAs Surface," *Mater. Res. Soc. Proc.*, vol. 388, p. 259, 1995.

[103] W.G. Bi and C.W. Tu, "Bowing parameter of the band-gap energy of GaNas," *Appl. Phys. Lett.*, vol. 70, no. 12, p. 1608, 1997.

[104] L. Bellaiche, S.-H. Wei, and A. Zunger, "Localization and percolation in semiconductor alloys: GaAsN vs GaAsP," *Phys. Rev. B*, vol. 54, p. 17568, 1996.

[105] S. A. Ding, S. R. Barman, and K. Horn, "Valence band discontinuity at a cubic GaN/GaAs heterojunction measured by synchrotron-radiation photoemission spectroscopy," *Appl. Phys. Lett.*, vol. 70, p. 2407, 1997.

[106] U. Tisch, E. Finkman, and J. Salzman, "The anomalous bandgap bowing in GaAsN," *Appl. Phys. Lett.*, vol. 81, p. 463, 2002.

[107] U. Tisch, E. Finkman, and J. Salzman, "Fine structure of the E1 Delta1 critical point in GaAsN," *Phys. Rev. B*, vol. 65, no. 15, p. 153204, 2002.

[108] W. Shan, W. Walukiewicz, and J. W. Ager III, "Band Anticrossing in GaInNAs Alloys," *Phys. Rev. Lett.*, vol. 82, p. 1221, 1999.

[109] T.S. Moss, T.D.F. Hawkins, and G.J. Burrell, "Use of plasma edge reflection measurements in the study of semiconductors," *J. Phys. C (Proc. Phys. Soc.)*, vol. 1, no. 2, p. 1435, 1968.

[110] N.A. van Dantzig and P.C.M Planken, "Time-resolved far-infrared reflectance of n-type GaAs," *Phys. Rev. B*, vol. 59, no. 3, p. 1586, 1999.

[111] P. Perlin, E. Litwin-Staaszewska, B. Suchanek, W. Knap, J. Camassel, E. Kaminska, and J.C. Chervin, "Determination of the effective mass of GaN from infrared reflectivity and Hall effect," *Appl. Phys. Lett.*, vol. 68, no. 8, p. 1114, 1996.

[112] J.F. Ziegler, "SRIM-2003," *Nucl. Instr. Meth. B*, vol. 219-220, p. 1027, 2004.

[113] M. W and W. Eckstein, "Tridyn - A TRIM simulation code including dynamic composition changes," *Nucl. Instr. and Meth. in Phys. Res. B*, vol. 2, p. 814, 1984.

[114] W. Möller, W. Eckstein, and J.P. Biersack, "Tridyn-binary collision simulation of atomic collisions and dynamic composition changes in solids," vol. 51, no. 3, pp. 355–368, 1988.

[115] W. Möller and M. Posselt, "TRIDYN_FZR User Manual," tech. rep., Forschungszentrum Dresden-Rossendorf, 2002.

[116] S. Perkowitz, *Optical Characterization of Semiconductors: Infrared, Raman, and Photoluminescence Spectroscopy*. Academic Press, 1993.

[117] C.P. Ho, J.D. Plummer, S.E. Hansen, and R.W. Dutton, "VLSI Process modeling - SUPREM III," *IEEE Transact. Elec. Devices*, vol. 30, no. 11, p. 1438, 1983.

[118] K.S. Krishnan and C.V. Raman, "A new type of secondary radiation," *Nature*, vol. 121, p. 501, 1928.

[119] L. Mandelstam and G. Landsberg, "Eine neue Erscheinung bei der Lichtzerstreuung in Krystallen," *Naturwissenschaften*, vol. 16, p. 557, 1928.

[120] Willes H. Weber and Roberto Merlin, eds., *Raman Scattering in Materials Science*, vol. 42 of *Springer Series in Material Science*. Springer, 2000.

[121] George Turrell, *Infrared and Raman Spectra of Crystals*. Academic Press, 1972.

[122] Loudon, "The Raman effect in crystals," *Advances in Physics*, vol. 13, p. 423, 1964.

[123] G. Abstreiter, E. Bauser, A. Fischer, and K. Ploog, "Raman Spectroscopy - A Versatile Tool for Characterization of Thin Films and Heterostructures of GaAs and AlGaAs," *Appl. Phys.*, vol. 16, p. 345, 1978.

[124] G. Herzberg, *Infrared and Raman Spectra.* D. Van Nostrad Company, Inc, 1945.

[125] J.L.T. Waugh and G. Dolling, "Crystal Dynamics of Gallium arsenide," *Phys. Rev.*, vol. 132, no. 6, p. 2410, 1963.

[126] A.M. Mintairov, P.A. Blagnov, and V.G. Melehin, "Ordering effects in Raman spectra of coherently strained GaAs(1-x)N(x)," *Phys. Rev. B*, vol. 56, p. 15836, 1997.

[127] A. Lofthus and P.H. Krupenie, "The spectrum of molecular nitrogen," *Journal of Physical and Chemical Reference Data*, vol. 6, no. 1, p. 113, 1977.

[128] H. Shen, F.H. Pollak, and R.N. Sacks, "Raman scattering determination of free-carrier concentration and surface space-charge layer in (100) n-GaAs," *Appl. Phys Lett.*, vol. 47, p. 891, 1985.

[129] M. Risch and M. Bradley, "Plasma Implantation for Band Gap Engineering of dilute GaAsN Alloys (TU-P4-1)," *Physics in Canada (Proceedings of the 2007 CAP Congress)*, vol. 63, no. 2, p. 104, 2007.

[130] K.U. Riemann and Th. Daube, "Analytical model of the relaxation of a collisionless ion matrix sheath," *J. Appl. Phys.*, vol. 86, no. 3, p. 1202, 1999.

[131] D. Israel, K.U. Riemann, and L. Tsendin, "Relaxation of a collisionless ion matrix sheath," *J. Appl. Phys.*, vol. 95, no. 9, p. 4565, 2004.

[132] B.P. Wood, "Displacement current and multiple pulse effects in plasma source ion implantation," *J. Appl. Phys.*, vol. 73, no. 10, p. 4770, 1993.

[133] S. Mändel, J. Brutscher, R. Günzel, and W. Möller, "Design Considerations for Plasma Immersion Ion Implantation Systems," *Nucl. Instr. Meth. Phys. Res. B*, vol. 112, p. 252, 1996.

[134] V. Vahedi, M. Lieberman, M.V. Alves, J.P. Verboncoeur, and C.K. Birdsall, "A one-dimernsional collosional model for plasma-immersion ion implantation," *J. Appl. Phys.*, vol. 69, no. 4, p. 2008, 1991.

[135] S. Qin and Ch. Chan, "Plasma immersion ion implantation model including multiple charge state," *J. Appl. Phys.*, vol. 79, no. 7, p. 3432, 1996.

[136] D.T.K. Kwok, T.W.H. Oates, D.R. McKenzie, and M.M.M Bilek, "Determination of the Equilibrium Ion Sheath in the Drifting Plasma by Numerical Simulation," *IEEE Transact. Plasma Sci.*, vol. 31, no. 5, p. 1044, 2003.

Appendix A

Instrumentation

A.1 Control Box

A.2 Sample Holder

Table A.1. Specifications of the astable 555 timer.

Capacitance:	0.02 μF
R_on:	384 kΩ $\pm$ 5 %
R_off:	1560 - 660 kΩ $\pm$ 5 %

Calculated	Pulse Width:	5.32 μs
	Repetition Rate:	46 - 109 Hz
Measured	Pulse Width:	6.2 μs
	Repetition Rate:	48-114 Hz

Table A.2. Specifications of the monostable 555 timer.

Capacitance:	3300μF

R (kΩ)	Time	Setting #
1.35 $\pm$5%	4.88 s	1
2.67 $\pm$5%	9.69 s	2
5.6 $\pm$5%	20.33 s	3
8.27 $\pm$5%	30.02 s	4
16.26 $\pm$10%	59.02 s	5
81.3 $\pm$5%	4.92 min	7
162.3 $\pm$5%	9.82 min	8
453 $\pm$15%	27.41 min	9
1519 $\pm$5%	91.9 min	10

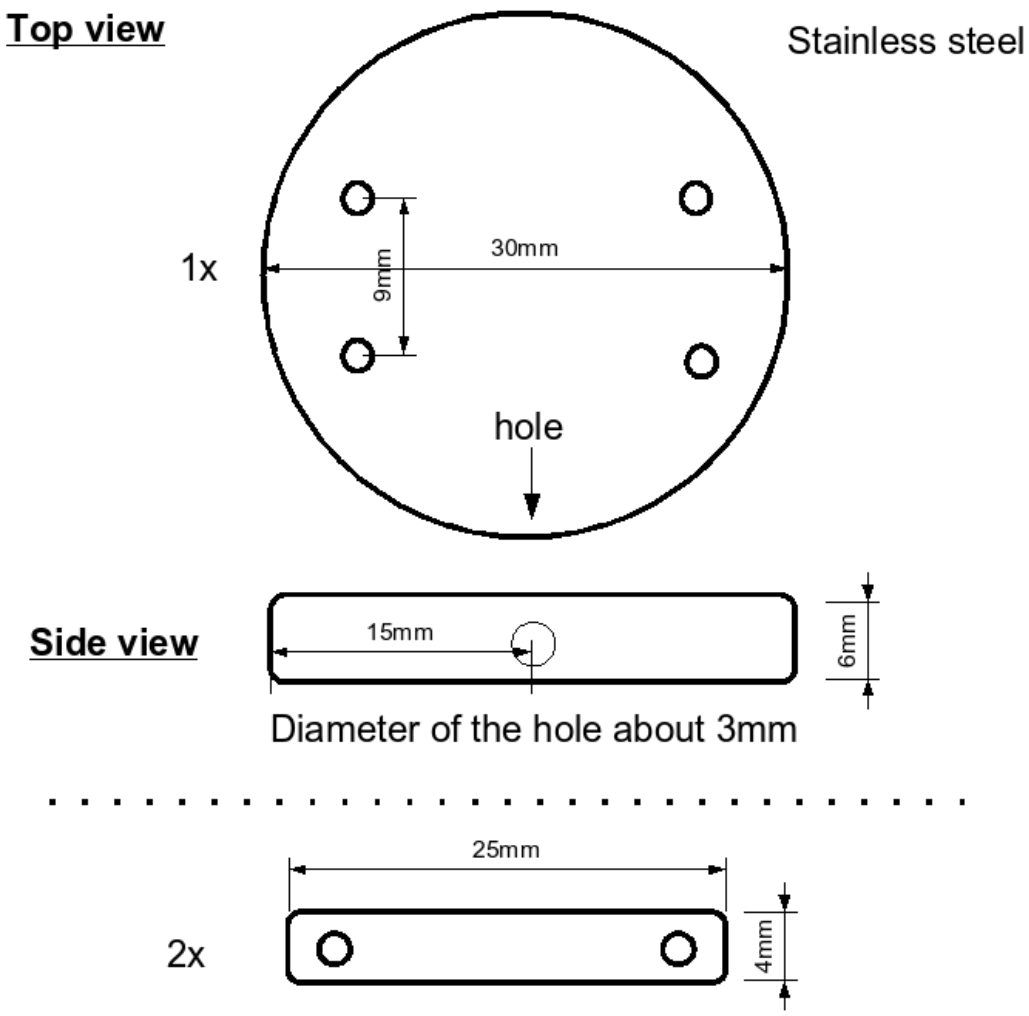

Figure A.1. The sample holder for GaAs implants.

Appendix B

Documentation

B.1 MSDS sheet for GaAs

B.2 Specimen Data Sheets

ELECTRONIC SPACE PRODUCTS INTERNATIONAL

1050 Benson Way, Ashland, OR 97520
Toll Free (800) 638-2581 * Fax (541) 488-8313
E-Mail: sales@espimetals.com

MATERIAL SAFETY DATA SHEET

I PRODUCT IDENTIFICATION

Trade Name: Gallium Arsenide
Formula: GaAs
Synonym: Gallium Monoarsenide
CAS #: 1303-00-0

II HAZARDOUS INGREDIENTS

Hazardous Components	%	OSHA/PEL	ACGIH/TLV
Gallium Arsenide	0-100	0.5 (As) mg/m^3	0.01 (As) mg/m^3

III PHYSICAL DATA

Boiling Point: N/E
Vapor Density: N/E
Molecular Weight: 144.64
Appearance and Odor: Dark gray cubic crystals
Melting Point: 1238 ^oC
Specific Gravity: 5.31 g/cc
Solubility in H_2O: Insoluble
% Volatiles: N/E or N/A

IV FIRE AND EXPLOSION HAZARDS DATA

Flash Point: N/A
Autoignition Temp: N/E or N/A
Flammable Limits: **Lower**: N/E or N/A **Upper**: N/E or N/A

Extinguishing Media: Use dry chemical, CO_2 or graphite. DO NOT USE WATER OR WATER SPRAY.
Fire Fighting Procedures: Wear NIOSH/MSHA approved self-contained breathing apparatus, flame and chemical resistant clothing, hats, boots, and gloves.
Unusual Fire and Explosion Hazards: Can React with Steam, Heat, Acid and Acid Fumes to Evolve Deadly Poisonous Arsine.

V HEALTH HAZARD INFORMATION

Effects of Exposure:

To the best of our knowledge the chemical, physical and toxicological properties of gallium arsenide have not been thoroughly investigated and reported.

Acute arsenic poisoning from ingestion results in marked irritation of the stomach and intestines with nausea, vomiting and diarrhea. In severe cases, the vomitus and stools are bloody and the patient goes into collapse and shock with weak, rapid pulse, cold sweats, coma and death. Chronic arsenic poisoning may cause disturbances of the digestive system such as loss of appetite, cramps, nausea, constipation or diarrhea.

Gallium and gallium compounds may cause metallic taste, dermatitis and depression of the bone marrow function. Large doses may cause hemorrhagic nephritis.

Acute Effects: May be irritating to skin, eyes and mucous membranes.
Carcinogenicity: **NTP**: Yes **IARC**: Yes **ACGIH**: Yes **OSHA**: Yes

EMERGENCY AND FIRST AID PROCEDURES:

Figure B.1. MSDS sheet for GaAs. Page 1/2.

INHALATION: Remove to fresh air; give oxygen if breathing is difficult. Seek medical attention.
INGESTION: Give 2 cups of milk or water and induce vomiting. Seek medical attention.
SKIN: Brush off skin, wash area with soap and water. Seek medical attention.
EYES: Immediately flush eyes, including under eyelids with large amounts of water. Call a physician.

VI REACTIVITY DATA

Stability: Stable
Conditions to Avoid: Water/moisture
Incompatibility (Material to Avoid): Steam, heat, acids, acid fumes.
Hazardous Decomposition Products: Highly toxic fumes of arsenic. Contact with acids releases toxic gases.
Hazardous Polymerization: Will not occur

VII SPILL OR LEAK PROCEDURES

Steps to Be Taken in Case Material Is Released or Spilled: Wear full protective equipment, cover spill with dry sand or vermiculite. Mix well and carefully transfer to a container.

Waste Disposal Method: Dispose of in accordance with Local, State and Federal Waste Disposal Regulations.

VIII SPECIAL PROTECTION INFORMATION

Respiratory Protection (Specify Type): Wear a NIOSH-approved dust-mist-fume cartridge respirator.
Ventilation: Handle under dry protective gas. Handle in a controlled environment. Use local exhaust to maintain below TLV level for Arsenic.

Eye Protection: ANSI approved safety goggles, or glasses.
Protective Gloves: Neoprene, Rubber
Other Protective Equipment: Wear protective clothing to prevent contamination of skin and clothes.

IX SPECIAL PRECAUTIONS

Precautions to Be Taken in Handling and Storage: Handle under dry protective gas. Protect from humidity and water. Store in tightly closed containers in a cool, dry place. Wash hands and face thoroughly after handling and before meals.

Work Practices: Implement engineering and work practice controls to reduce and maintain concentration of exposure. Handle in a controlled, inert atmosphere. Minimize exposure by using local exhaust and an enclosing process if/when possible. Use good housekeeping and sanitation practices. Do not blow dust off clothing or skin with compressed air. Maintain eyewash capable of sustained flushing, safety drench shower and facilities for washing.

The above information is believed to be correct, but does not purport to be all inclusive and shall be used only as a guide. ESPI shall not be held liable for any damage resulting from handling or from contact with the above product.

Issued by: S. Dierks
Date: October 2002

Figure B.2. MSDS sheet for GaAs. Page 2/2.

Name of Sample: _____ Code: _____

Name of Set: _____# in Set: ___/___

Purpose: _____

Storage Room #: _____ Box ID: _____

Cleaning of Chamber:

Work Done By: _____ Date (Day/Month/Year): __ / __ / 20__

Type: Mechanical / Chemical / Plasma Chemical/Tool used: _____

Specify Procedure:

_____

_____

Plasma Cleaning of Specimen:

Work Done By: _____ Date (Day/Month/Year): __ / __ / 20__

Power (W): _____ PPS (Hz) or DC: _____

Base pressure (Torr): _____ Working Pressure (mTorr): _____

Gas (H/N/CH4/Ar) _____ Duration (hrs:min:sec): ___:____:___

Voltage (V): _____ Cool Down (hrs:min:sec): ___:____:___

Other Cleaning of Specimen:

Work Done By: _____ Date (Day/Month/Year): __ / __ / 20__

Type: Mechanical / Chemical Chemical/Tool used: _____

Specify Procedure:

_____

_____

Cleaving of Specimen:

Work Done By: _____ Date (Day/Month/Year): __ / __ / 20__

Tool used: _____ Orientation marked by: _____

Specify Procedure:

_____

_____

Figure B.3. Specimen data sheet to document implants and their characterizations. Page 1/4.

Plasma Ion Implantation:

Work Done By:	_____	Date (Day/Month/Year):	__ / __ / 20__
# samples processed:	_____	Code:	_____
Base pressure (Torr):	_____	Working Pressure (mTorr):	_____
Flow Rate (ccm):	_____	POS:	_____
Power (W):	_____	Shunt / Series Matching	____ / _____
PPS (Hz):	XXXXXXX		
1. Voltage (kV):	_____	Gas: _____ PPS (Hz):	_____
# Pulses:	_____	Duration (hrs:min:sec):	___:____:___
Start:	_____	Stop:	_____
Pulse File Name:	_____	Cool Down (hrs:min:sec):	___:____:___
2. Voltage (kV):	_____	Gas: _____ PPS (Hz):	_____
# Pulses:	_____	Duration (hrs:min:sec):	___:____:___
Start:	_____	Stop:	_____
Pulse File Name:	_____	Cool Down (hrs:min:sec):	___:____:___
3. Voltage (kV):	_____	Gas: _____ PPS (Hz):	_____
# Pulses:	_____	Duration (hrs:min:sec):	___:____:___
Start:	_____	Stop:	_____
Pulse File Name:	_____	Cool Down (hrs:min:sec):	___:____:___
4. Voltage (kV):	_____	Gas: _____ PPS (Hz):	_____
# Pulses:	_____	Duration (hrs:min:sec):	___:____:___
Start:	_____	Stop:	_____
Pulse File Name:	_____	Cool Down (hrs:min:sec):	___:____:___

Comments/Irregularities:

_____

_____

_____

Figure B.4. Specimen data sheet to document implants and their characterizations. Page 2/4.

Annealing:

Work Done By:	_____	Date (Day/Month/Year):	__ / __ / 20__
# samples processed:	_____	Code:	_____
Environment (Air, N):	_____	Pressure (mTorr) start/end:	____ / _____
Duration (hrs:min:sec):	___:____:___	Temperature (°C):	_____
Ramp Mode:	_____	Cool Down (hrs:min:sec):	___:____:___

Comments:

Langmuir Probe:

Work Done By:	_____	Date (Day/Month/Year):	__ / __ / 20__
Sweep Freq (Hz):	_____	Voltage Range (V):	____ to ____
File Name (s):	_____	While Implanting	Yes / No
Electron Temp (eV):	_____	Electron Dens. (m^{-3}):	_____
Plasma Potential (V):	_____		

Comments:

Characterization:

Raman	Yes / No	File Name (s):	_____
Work Done By:	_____	Date (Day/Month/Year):	__ / __ / 20__
FTIR	Yes / No	File Name (s):	_____
Work Done By:	_____	Date (Day/Month/Year):	__ / __ / 20__

Comments:

Figure B.5. Specimen data sheet to document implants and their characterizations. Page 3/4.

Coating:

samples processed: _____ Code: _____

Notes:

_____

_____

_____

_____

_____

_____

_____

_____

_____

_____

_____

_____

_____

Figure B.6. Specimen data sheet to document implants and their characterizations. Page 4/4.

Appendix C

Complementary Material

C.1 Validity of the Assumptions in the Lieberman Model

The Lieberman model works within the framework of the two-fluid model given by the continuity equation

$$\frac{\partial n_i}{\partial t} + \frac{\partial}{\partial x}\left(n_i u_i\right) = 0, \tag{C.1}$$

the equation of motion

$$m_i \frac{\partial v_i}{\partial t} + m_i u_i \frac{\partial u_i}{\partial t} = -e\frac{\partial \Phi}{\partial x} \tag{C.2}$$

and Poisson's equation

$$\frac{\partial^2 \Phi}{\partial x^2} = -\frac{\Phi}{\lambda_D} \tag{C.3}$$

for Maxwell-distributed electrons

$$n_e = n_0 \cdot exp\left(-\frac{\Phi}{T_e}\right) \tag{C.4}$$

and cold ions ($n_0 = n_i$). Lieberman [60] derives two equations for the implantation current of an ideal pulse, i.e. zero rise and fall time. The first solution accounts for the Matrix sheath implantation and a second one for Child-law implantation. The solution over the duration of the pulse has a discontinuity at $\omega_p t = 2.7$ where the point of instantaneous transition is assumed. The first and second assumption are justified post-hoc by agreement with numerical solutions of eqs. (C.1 - C.4) over a wide range of parameters.

Riemann [130] reported another analytical model based on special solutions to the fluid equation for ideal pulses which supersede the first and second assumption in the following discussion. His solutions agree even better with numerical simulations than the Lieberman model, only surpassed by a recent paper of the same group [131] which also includes subtle features in the ion extraction phase. There is no report of the prediction of ion current caused by real pulses using the Riemann model, despite its potential to include Matrix sheath contributions in the predictions in a continuous way.

The physical insight and simplicity of an analytical description for a complex system such as the plasma sheath must be paid for by assumptions which specify the boundaries of the description's validity. The analytical Lieberman model for the ion current toward the target is subject to the following conditions:

1. Electric fields are frozen to their initial value during a calculation step. Thus, ion motion and the sheath positions are treated quasi-statically.

2. A fully expanded quasi-static ion matrix sheath forms instantaneously and the current can be described by a (quasi-static) Child-Langmuir law [30] during the entire implantation.

3. Pre-sheath and the plasma bulk supply the Bohm current and the plasma ion density at all times which are treated as boundary conditions. Furthermore, the ion reservoir is infinite and refilling happens instantaneously.

4. Electrons respond instantaneously to the applied fields. Lieberman [60] refers to those electrons as 'inertialess'.

5. Ions arrive at the target instantaneously.

6. Uniform plasma density in the region of implantation.

7. Collsionless ion flow.

8. The sheath edge is abrupt which applies if the Debye length is much smaller than the initial sheath width.

9. Ions are mono-atomic and singly charged. Moreover, multiple ion species in the plasma produce a common sheath edge, i.e. they can be treated by an effective mass.

10. The geometry is planar and one dimensional.

11. Ion density and initial sheath width at the beginning each applied voltage pulse are the same.

12. The measured potential is the potential at the sample surface.

These assumptions will be examined in the following paragraphs.

Frozen Electric Fields

The effective electric fields are set by electrons which react much faster to changes in the applied electric potential than the ions. The ratio of ion to electron response time is smallest for hydrogen

$$\frac{\tau_i}{\tau_e} = \frac{\omega_i^{-1}}{\omega_e^{-1}} = \sqrt{\frac{m_i}{m_e}} = \sqrt{1836} = \approx 42.8 \gg 1. \tag{C.5}$$

The ratio in a nitrogen plasma with effective ion mass $m_i = 26$ u is $\tau_i : \tau_e = 218 : 1$. Hence, the characteristic time scale in plasma ion implantation exceeds the electron response time by far. In addition, the ion transit time for small sheaths and dense plasmas is negligible as I will show in one of the following paragraphs. The change in the electric field in the sheath region due to ions is thus also marginal. Therefore, the field may be assumed frozen during a calculation step.

Quasi-Static Child Langmuir Description

The Child-Langmuir law is only an approximation to the full description given by eqs. (C.1) through (C.4). It is a poor description of the dynamical processes that transform the Matrix sheath into a steady-state sheath governed by the space-charge. However, the approximation holds quite well after a few microseconds for most plasma conditions. The Child-Langmuir law can be derived from Poisson's equation only if the electron temperature is small compared to the applied potential. This is generally the case in high-voltage implantation. The difference to measured currents and numerical simulations arises mostly from the fact that the quasi-static assumption does not hold at the beginning of the voltage pulse when the target potential and thus the sheath width increases rapidly. The contributions from the initial dynamic sheath expansion phase may be neglected completely if the pulse duration is ten-fold or more longer than the expansion phase.

Infinite Ion Reservoir

It is a fair assumption that the ion reservoir is infinite if the chamber is sufficiently large, the flow rate of the precursor gas is appropriate and the ionization rate of new gas molecules is quick. This can be controlled by a smart choice of the plasma and gas parameters as well as by the instrumentation. The plasma bulk and pre-sheath regions are therefore persistent and can be treated as boundary conditions.

Instant Ion Arrival

The characteristic time scale of plasma ion implantation is set by the time it takes ions to travel through the initial Matrix sheath $\omega_i^{-1} = 35$ ns which is of the order of the sampling time of the oscilloscope $t_s = 40$ ns. Hence, even the farthest ions arrive at the target within the sampling time. Wood [132] found that ion transit times become a significant for low plasma densities of 10^{14} to 10^{15} m^{-3}. Also, an ion is not accelerated by the full potential if the sheath expands significantly during the transit time and the displacement current becomes important in this situation. Barroso et al. [69] found that the measured plasma ion current for the low density regime is given by the convection current rather than the Child-Langmuir law.

Uniform Plasma Density

The (bulk) ion density profiles for the ICP configuration used in this study can be assumed uniform in the region of interest, i.e. toward the middle of the chamber. However, the plasma ion density in real ICP plasma discharges is always somewhat distributed which adds to the error budget for this model.

Collisionless Ion Flow

Whether the ion flow is collisionless depends on the plasma parameters pressure, Debye length, electron temperature and the potential at the electrode. The condition

of a collisionless sheath is that the mean free path of ions MFP is greater than the sheath width

$$s_{\max,\mathrm{CL}} \approx \lambda_D \cdot \left(\frac{|V_0|}{T_e}\right)^{3/4}, \tag{C.6}$$

where λ_D is the Debye length, V_0 is the voltage at the plateau of the pulse and T_e is the electron temperature. The mean free path of ions in a plasma is given by [133]

$$\mathrm{MFP} = \frac{a}{p}, \tag{C.7}$$

where a is a tabulated constant (4.58 mTorr·cm for nitrogen) [133] and p is the working pressure of the discharge. The value of the mean free path is 1.53 cm for a working pressure of 3 mTorr. Fig. C.1 shows the sheath width calculated by the p2i software for a -10 kV voltage pulse and the mean free path (MFP). The sheath is collisional during the first microsecond of the 6.5 μs pulse, i.e. during the first 15% of the pulse. This could be neglected for longer pulses, but adds an error to a non-collisional calculation. Vahedi et al. [134] published an extension to the Lieberman model to account for the ion flow in highly collisional plasmas, but the situation during the first few microseconds of the implantation is most likely low collisional and can still be treated by the collisionless description. Fig. C.2 is a graphical representation of the condition for a collisionless sheath $s <$ MFP. The inequality is true if the conditions of electron temperature, ion density and peak voltage of the pulse are above the dashed (black) horizontal line of the pressure during the implantation. The plot is valid for ideal long pulses. It is likely that the steady state condition is not reached if the voltage pulse is short ($\sim$ 5 μs) and/or the density is low. The maximal sheath width during the implantation is then up 15% lower than the ideal sheath width for the pulse shapes produced by our setup and the plasma parameters can use.

Abrupt Sheath Edge

For the sheath edge to be abrupt, the Debye length must be much smaller than the sheath width which is the case when the applied voltage V is much greater than the electron temperature. This can easily seen by rearranging eq. (C.6).

Mono-Atomic Ions

The ions in ICP discharges have rarely a higher charge state than singly charged and assumption 9 is thus valid in this study. Qin [66, 135] and Linder [67] extended the Lieberman model to include multiple ion species with arbitrary charge states. Multiple ion species are included in my model and arbitrary charge states could easily be added if necessary.

The ion masses and Bohm velocities of individual species are replaced by an effective mass [135]

$$\sqrt{m_{i,\mathrm{eff}}} = \sum r_k \cdot \sqrt{Z_k m_k} \tag{C.8}$$

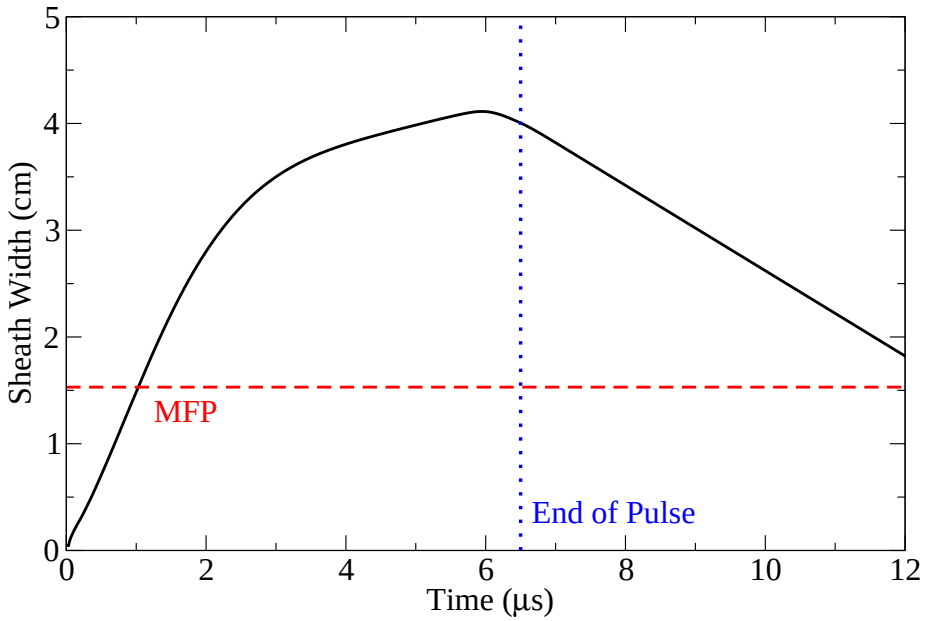

Figure C.1. Calculated sheath width of a -10 kV pulse compared with the mean free path. The calculations were done using the p2i software which is discussed in Chapter 5. The plasma conditions are: 3 mTorr pressure, 1.2×10^{16} m^{-3} density and 4.34 eV electron temperature.

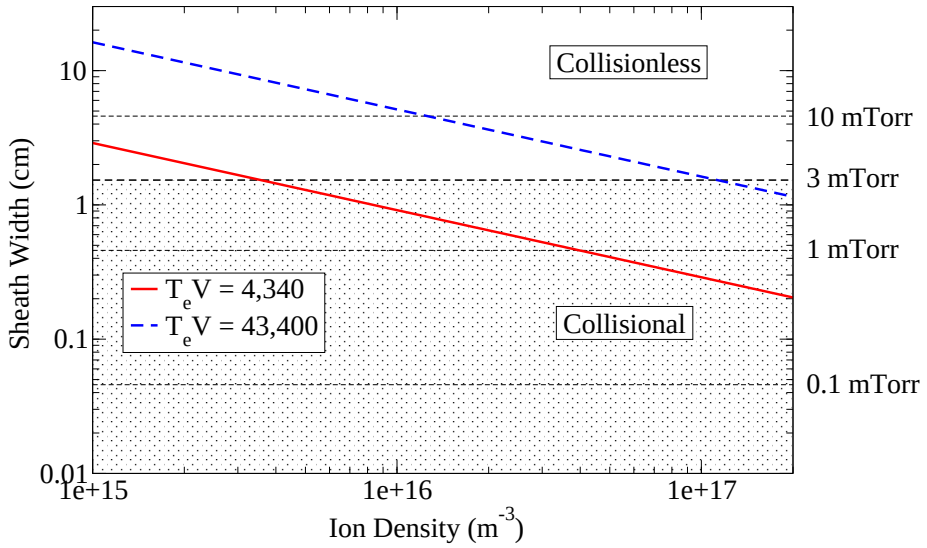

Figure C.2. Graphical representation of the condition for a collisonless sheath. The coloured lines represent the steady-state sheath width of ideal pulses for various electron temperatures T_e and peak voltages V. The dashed (black) horizontal lines are the lowest sheath width for which the sheath may be assumed collisionless for various working pressures. The area of the plot which is collisionless for the pressure used in this study is dotted. The solid red and dashed blue line represent an ideal -1 kV and -10 kV pulse, respectively.

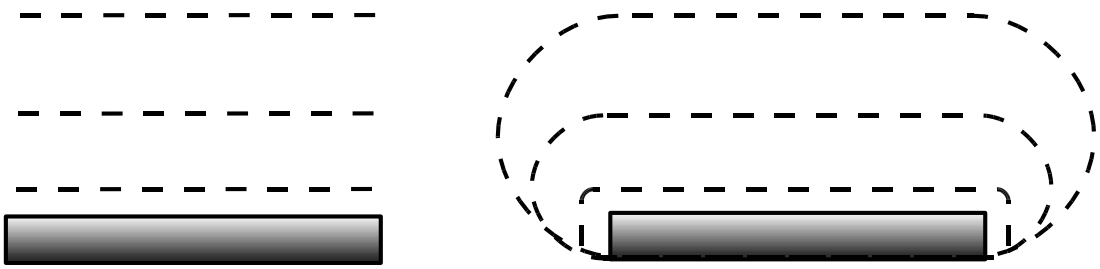

Figure C.3. Schematic movement of the sheath edge (dashed line) away from an extended sample in a one-dimensional model (left) and a two-dimensional model (right).

and Bohm velocity [67]

$$u_{B,\mathrm{eff}} = \frac{1}{\sqrt{m_{i,\mathrm{eff}}}} \sum_k r_k u_{B,k} \sqrt{m_k}, \tag{C.9}$$

where r_k is the population of species k in the plasma and Z_k is the charge state. This simplification is only valid during the inflating sheaths and steady-state sheaths. The individual ion transit times become important during the sheath collapse because the lightest ion species will set the pace of sheath decrease if all species are in the same charge state. Kwok et al. [136] studied the situation by means of a particle-in-a-cell simulation.

Planar Geometry

Fig. C.3 shows schematically a comparison between a one-dimension planar treatment of an extended sample and a more realistic two-dimensional model which includes edge effects. Larger sheath widths in real implantation situation of a box will evolve towards a spherical sheath if the applied voltage is high and the sheath has been given enough time to reach steady-state. The predictions of both models are still in good agreement in the middle of the sample. The assumption of a planar one-dimensional sheath is therefore valid for low voltages, short pulses and sufficiently flat samples. Moreover, the dimensions of the chamber must be large enough, so that the shape of the sheath is not distorted. Our setup fulfills the requirements for a planar model. Barrosso et al. [69] give an example of a situation in which the sheath at later times must have been spherical to agree with the measured plasma ion current.

Initial Conditions

For the 11th assumption to be valid, the sheath must refill entirely, i.e. the sheath collapses completely between pulses and the time between subsequent pulses is large enough to allow ions to diffuse into the former sheath region until the density there is at the bulk level again.

The ion transit time across the sheath is the time it takes for the sheath to collapse in the case of a short fall time of the applied voltage waveform. It is then given by

$$\Delta t_{\text{collapse}} = \frac{s_{\max}}{u_B}, \tag{C.10}$$

where $s_{\max}$ is the maximal sheath width and u_B is the Bohm velocity. The sheath vanishes in a nitrogen plasma after about 10 μs for a density of 1.2×10^{16} m^{-3} and an electron temperature of 4.34 eV. In addition, the voltage wave form lasts for approximately 6.5 μs (FWHM). The sheath exists therefore for about 16.5 μs under the given conditions. Hence the sheath does not close if the pulse repetition rate is faster than 60 kHz.

This is not the final answer since the closed sheath must still be refilled with ions. Wood [132] found that the depleted sheath fills in according to:

$$\frac{n_s(t)}{n_0} = 1 - \left(1 - \frac{n_{s,0}}{n_0}\right) \cdot \exp(-\vartheta t), \tag{C.11}$$

where $n_s(t)$ is the ion density in the former sheath region at time t, n_0 is the plasma bulk density, $n_{s,0}$ is the initial density in the depleted region. The fill-in rate ϑ is given by

$$\vartheta = \frac{T_e}{T_i} \cdot \frac{1}{s_m} \cdot \sqrt{\frac{kT_i}{2\pi m_i}}, \tag{C.12}$$

where s_m is the maximal sheath width, m_i is the (effective) ion mass, T_e and T_i are the electron and ion temperatures, respectively. Wood also calculated the time to fill-in the ion density to 95% of the bulk density

$$t_{95\%} = \frac{3}{\vartheta}. \tag{C.13}$$

This time is plotted in Fig. C.4 as a function of the maximal sheath width for various ion temperatures. These temperatures vary between 0.1 and 0.5 eV in ICP discharges and the refill-time to 95% of the bulk density is thus between the red dashed and the solid black line. In the worst case, an additional 55 μs must be added to the time for the sheath collapse for a 4 cm sheath. The maximum frequency is then 14 kHz which is still far beyond the capabilities of our pulser.

Potential at the Surface

This is discussed in Section 3.3.3. The result for nitrogen ion implantation into gallium arsenide is that charging of the surface is not likely and the potential at the electrode may thus be taken as the potential at the surface.

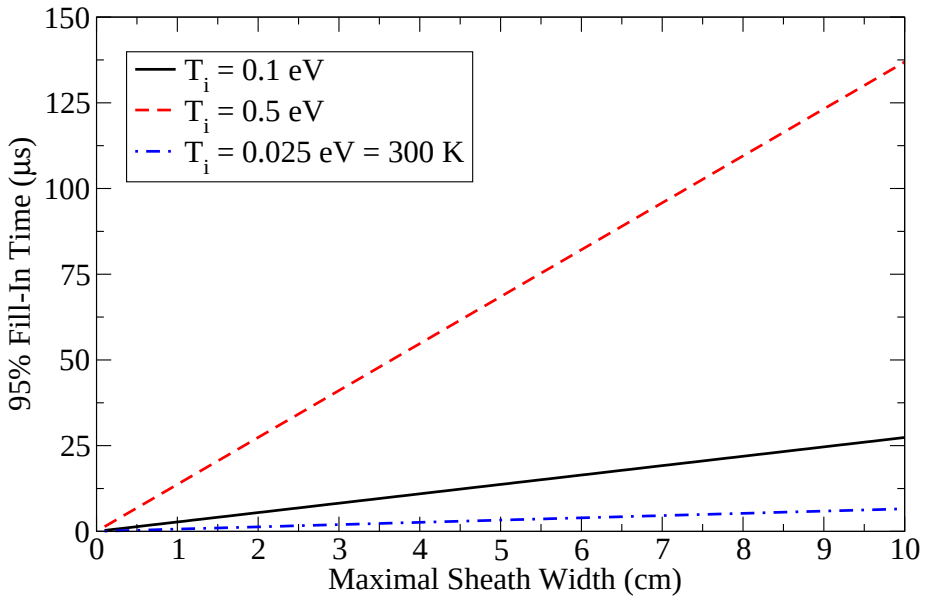

Figure C.4. Refill time to 95% of the bulk density as a function of the maximal sheath width for various ion temperatures including room temperature.